November 2018

Impact of Chemical Doping on the Thermoelectric Charge Transport of Organic Semiconductors

Connor J. Boyle

IMPACT OF CHEMICAL DOPING ON THE THERMOELECTRIC CHARGE TRANSPORT OF ORGANIC SEMICONDUCTORS

A Dissertation Presented

by

CONNOR J. BOYLE

Submitted to the Graduate School of the
University of Massachusetts Amherst in partial fulfillment
of the requirements for the degree of

DOCTOR OF PHILOSOPHY

September 2018

Department of Chemistry

IMPACT OF CHEMICAL DOPING ON THE THERMOELECTRIC CHARGE TRANSPORT OF ORGANIC SEMICONDUCTORS

A Dissertation Presented

by

CONNOR J. BOYLE

Approved as to style and content by:

_____
D. Venkataraman, Chair

_____
Michael D. Barnes, Member

_____
E. Bryan Coughlin, Member

_____
Anthony D. Dinsmore, Member

_____
Richard Vachet, Department Head
Department of Chemistry

DEDICATION

To my brother, Desmond, my father, Brian, and my mother, Colleen, for your support, love, and guidance.

To my best friend and wife, Ashley, for your love, care, patience, and motivation during every step of this journey.

ACKNOWLEDGMENTS

I have many people to thank for where I am today, and it would not be possible to list them all here. I will try, however, to thank some of them.

I will start by thanking Allison Chase, whose attitude toward teaching and supporting students helped me in High School to find the appreciation for science and chemistry that I still have to this day, and Ivan Gitsov, whose passion for organic and polymer chemistry at SUNY-ESF motivated me to seek the fulfilling research I found at SUNY-ESF and at UMass.

I thank every member of the DV group that I have had the opportunity to work with: Eric Schott, Joseph Daignault, Haote Li, Donnie Rollings, Julia Lenef. Dr. Monojit Bag, Dr. Sravan Surampudi, Dr. Dana Algaier, Dr. Timothy Gehan, Dr. Lawrence Renna, Seung Pyo Jeong, Christie L. C. Ellis, Emily Smith, Hamza Javaid, and Dr. Sashi Debnath. Being surrounded by such a supportive, creative, curious, and fun group has been an incredible and unforgettable experience, and I thank you all for shaping the way I think about science and problem solving and helping me have such a great time in the process.

I am grateful for the many helpful collaborations at UMass and elsewhere that have supported and shaped my graduate research. I thank Dr. Sashi Debnath for the synthesis and characterization of electron transporting polymers including PDNDIV and PFNDIV, Dr. Dongming Zhou and Prof. Kevin Kittilstved for their EPR studies on radical anion polymers, and Prof. Bryan Wong for calculating the molecular orbital levels and energy levels of electron accepting monomers and oligomers. I thank Prof. Paul Lahti and Dr. Murat Tonga for providing and demonstrating the use of the thermoelectric

measurement apparatus that has become the central and indispensable instrument for my graduate research. I thank Dr. Timothy Gehan for synthesizing and providing PBTDV2 and Dr. Feng Liu and Prof. Thomas P. Russell for synthesizing and providing PDPP4T. I thank Dr. Ljiljana Korugic-Karasz for helpful discussions on charge transport through semicrystalline polymers. I thank Stephen Dongming Kang and Dr. G. Jeffrey Snyder for providing their transport model fitting MatLAB code and Dr. Lawrence Renna for his insights and modifications to the code. I thank Dr. Peijian Wang and Prof. Mike Barnes for characterizing the KPFM and PL microscopy. I thank Meenakshi Upadhyaya and Zlatan Aksamija for teaching me their model of thermoelectric charge transport, fitting experimental thermoelectric data to their model, and countless meetings discussing the peculiar nature of charge transport in disordered organic semiconductors that led to our understanding of its underlying causes.

I thank Prof. Hans Mentzen and all the Chemistry Instructors at UMass, for their guidance and for fostering my development as a teacher.

I thank my past committee member, Prof. Paul Lahti, and my current committee members Prof. Anthony Dinsmore, Prof. Bryan Coughlin, and Prof. Mike Barnes. Prof. Paul Lahti provided thoughtful insights to my research as a former member of my committee and has since continued to reach out to me with thoughtful advice, materials, and instrumentation for my research. Prof. Mike Barnes' teaching has helped me appreciate both spectroscopy theory and the efficacy of computer software for calculating, modeling, and visualizing the physical organic chemistry problems that would otherwise evade my imagination. Prof. Anthony Dinsmore, Prof. Bryan Coughlin,

and Prof. Mike Barnes have all offered thoughtful insight and suggestions to my research projects and my career development at UMass, for which I am graciously appreciative.

Lastly, I cannot thank DV enough for his guidance as my teacher, Ph.D. advisor, and mentor. DV is never afraid to imagine and think outside of the research status quo, which has made all of the research projects in his lab unique, challenging, rewarding, and exciting. He also brings the same attitude to the classroom, encouraging his students to challenge the conventional wisdom and improve their understanding by scientifically constructing their own interpretation of the chemistry. DV prioritized learning about my short-term and long-term research and career aspirations so that he could offer the advice and opportunities that helped me develop the skills and training I valued most. He routinely joins the group for coffee and lunch in and out of the lab, making himself approachable and making it clear that we can always talk to him about our research concerns, questions about grad school, and life. DV's enthusiasm for science, teaching, mentoring, and making sure his lab is a supportive environment for all of his group members to learn, develop professionally, and be happy have made DV better than the best advisor I could have imagined.

ABSTRACT

IMPACT OF CHEMICAL DOPING ON THE THERMOELECTRIC CHARGE TRANSPORT OF ORGANIC SEMICONDUCTORS

SEPTEMBER 2018

CONNOR J. BOYLE, B.S., STATE UNIVERSITY OF NEW YORK – COLLEGE OF ENVIRONMENTAL SCIENCE AND FORESTRY

Ph.D., UNIVERSITY OF MASSACHUSETTS AMHERST

Directed by: Professor D. Venkataraman

The thermoelectric properties of organic semiconductors allow them to directly convert heat into electricity without the use of moving parts and to directly convert electricity into heat without the use of working fluids. These properties offer opportunities for the generation of electricity from non-conventional or renewable sources of heat and for refrigeration without the risk of leaking harmful working fluids at any length scale down to the nanoscale. Since organic materials are lightweight, flexible, and made from abundant resources, these opportunities could one day become affordable for widespread use and could be expanded to include specialized and otherwise difficult to reach applications, such as wearable refrigeration and electricity generation from anthropogenic heat. Since these properties are a result of how charge carriers in organic materials transfer energy upon conduction, measuring these properties also allows us to better understand the factors that influence how charge carriers carry energy during charge transport.

One of the remaining challenges in developing organic thermoelectric materials for practical use is the preparation of n-type thermoelectric materials, which transport electrons as their charge carrier, since most n-type organic semiconductors are unstable in

air due to electron transfer to oxygen gas. We synthesized three organic conjugated polymers based on electron deficient rylene diimides and a vinylene spacer – PDNDIV, PFNDIV, and PDIV – to study how these could be doped into n-type semiconductors and how long these persist in air. Each polymer was capable of electron transport, and PFNDIV was capable of remaining n-doped with electronic charges for at least one week in air.

Blending conducting fillers into organic thermoelectric materials can alter their thermoelectric properties by altering the mechanism of charge transport. We blended the conductive filler SWNT into the organic conjugated polymer PBTDV2 and measured the thermoelectric properties. Although PBTDV2 was originally developed for use as an electron transporting polymer, all blends of SWNT with PBTDV2 had p-type, hole transporting, thermoelectric properties similar to those of oxygen-doped SWNT.

We measured the thermoelectric properties of two p-type organic polymers – P3HT and PDPP4T – that were doped to achieve a high concentration of charge carriers as they spontaneously de-doped and decreased their charge carrier concentration. Modeling these thermoelectric properties revealed that the spatial distribution of dopants in the polymers impacted the how much energy was carried per charge carrier due to Coulombic interactions of the dopants with the charge carriers, and that more heterogeneous spatial distributions of dopants can limit the thermoelectric performance by limiting how much energy is carried per charge carrier. These findings aid in the future development of organic thermoelectric materials by highlighting the importance of doping organic thermoelectric materials in ways that achieve homogeneous spatial distributions of dopants.

TABLE OF CONTENTS

Page

LIST OF TABLES

Table Page

LIST OF FIGURES

CHAPTER 1

INTRODUCTION

1.1 Brief Overview of the Thermoelectric Effect

The conversion of heat into electricity has enabled the electrical grid that has revolutionized the world around us allowing us to light our homes, share information across the globe at light speed, stay connected with those we care about the most, and much more. This electrical grid is made possible by power plants around the world, most of which use heat engines to convert heat into motion and then use generators to convert that motion into electricity. Despite our current global reliance on a combination of heat engines and generators with moving parts for converting heat into electricity, this is not the only way heat can be transferred into electrical power.

Conductors and semiconductors can convert heat directly into electricity, as described by the Seebeck effect.[1] Whenever heat is applied to these types of materials, the electrons and other types of charge carriers have more energy on the hotter side than on the colder side. This leads to the formation of a voltage across the material according to the relation $\alpha = \frac{\Delta V}{\Delta T}$, where α is a material property known as the Seebeck coefficient, ΔT is the temperature gradient applied to the material, and ΔV is the voltage response, also known as the thermovoltage. When two materials with dissimilar α are connected in series by conductive interconnects positioned on the hot and cold side of the materials, electrical power can be generated as like charges move codirectionally through the series while unlike charges move contradirectionally, as depicted in Figure 1. Ideally, one of the materials should have a positive value of α, making it a p-type thermoelectric material

which moves holes from hot side to cold, and the other material should have a negative α, making it an n-type thermoelectric material which moves electrons from hot side to cold. When no heat is applied to this device, but a current is applied, charge carriers carry heat with them as they move through the series, resulting in the heating of one side and the cooling of another, a process known as the Peltier effect. Thermoelectric devices can therefore function either as an electrical power generator using heat sources or as a refrigerator using electrical power sources.

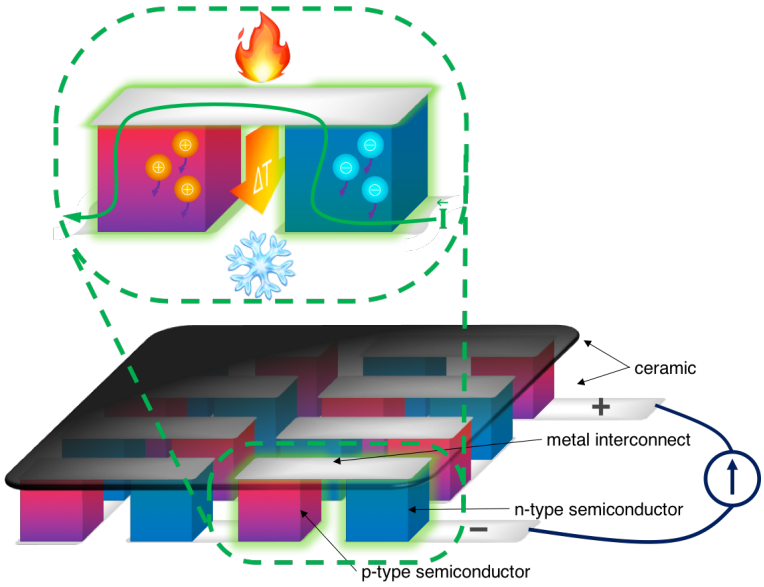

Figure 1: p-type and n-type semiconductor blocks connected by metal interconnects in a configuration that enables power generation from a temperature gradient through the device.

The magnitude of power that can be generated across a material at a particular temperature gradient is given by its thermoelectric power factor, $\sigma\alpha^2$, where σ is the conductivity of the material. A material's thermoelectric power conversion efficiency depends on its power factor and on how much its heat transfer is dominated by the transfer of charge carriers from hot side to cold, so that the amount of heat wasted by

transfers through other processes is minimal. These properties are combined into the dimensionless thermoelectric figure of merit, *ZT*, which indicates how well the material can perform in terms of its power conversion efficiency and is given by the relation: $ZT = \frac{\sigma\alpha^2}{\kappa}T$, where κ is the thermal conductivity of the material.

The direct conversion of heat into electricity by thermoelectric materials without the use of moving parts makes them advantageous for harvesting energy from heat sources that cannot practically power heat engines, such as anthropogenic heat, solar thermal heat, and waste heat from industrial processes and vehicles. Thermoelectric materials therefore make it possible to generate more of our electrical power without burning fossil fuels and to generate electrical power in remote areas that do not have access to the grid, including the generation of electricity for space probes using radioisotope heating. The most commonly used thermoelectric materials in the current market are bismuth telluride and lead telluride, which have a *ZT* of ~1.

Organic thermoelectric materials have many advantages over inorganic ones such as bismuth telluride. Organic materials are lightweight and flexible, making them amenable to applications where weight, hardness, and brittleness are undesirable, such as wearable thermoelectric materials for clothing and accessories. Organic materials are also prepared from abundant materials, making them more widely available and affordable then materials based on rare metals such as tellurium. Organic thermoelectric materials are not yet competitive, however, in terms of their *ZT*.

1.2 The Current Status of Organic Thermoelectric Materials

Organic semiconductors typically have a low thermal conductivity, placing the focus of improving their *ZT* on increasing their thermoelectric power factor $\sigma\alpha^2$. To understand $\sigma\alpha^2$can be improved, it is convenient to begin by examining Fritzsche's general equations for σ and α.[2] Fritzche described the conductivity as the integral over all single electron states: $\sigma = \int \sigma(E)\, dE = q \int g(E)\mu(E)f(E)[1 - f(E)]\, dE$ and the α as the energy carried per unit charge, relative to the E_F, in proportion to that charge carriers relative contribution to the overall conduction: $\alpha = \left(\frac{k_B}{q}\right) \int \left(\frac{E-E_F}{kT}\right) \frac{\sigma(E)}{\sigma} dE$. Here, q is the charge of the carrier, $g(E)$ is the density of states (DOS), $\mu(E)$ is the charge carrier mobility, $f(E)$ is the Fermi-Dirac distribution, $f(E) = \frac{1}{1+e^{\frac{E-E_F}{kT}}}$, E_F is the electron chemical potential, and k is the Boltzmann constant. It can be seen that adjusting the E_F to a position closer to the DOS will increase the overlap between the Fermi window $f(E)[1\text{-}f(E)]$ and the DOS, and thus increase the σ. It can also be seen that moving the E_F to a position closer to the DOS will decrease the energy of each single electron state relative to the E_F and will thus decrease the α. This results in a tradeoff between σ and α when between moving the E_F closer to the DOS, and an optimal E_F where the thermoelectric power factor $\sigma\alpha^2$ is optimized. This tradeoff can also be understood in terms of the carrier concentration, n, given by: $n = \int g(E)f(E)dE$. Moving the E_F closer to the DOS increases n, so an increasing n is predicted to increase the σ while decreasing α, at some point reaching an optimal n for maximizing the value of $\sigma\alpha^2$. Optimization of n for a given organic thermoelectric material is therefore a common strategy for improving $\sigma\alpha^2$.

The reported *ZT* for p-type organic thermoelectric materials has recently approached values competitive with inorganic. A *ZT* of 0.24 was reported for PEDOT:PSS, and was attained by optimizing *n* by chemical reduction of doped PEDOT:PSS.[3] A *ZT* of 0.42 is reported for DMSO-mixed PEDOT:PSS, having a power factor of 469 μW m^{-1} K^{-2}.[4] A power factor of 1,270 μW m^{-1} K^{-2} has been achieved for PEDOT:Tos by electrochemically controlling the carrier concentration, but the thermal conductivity and therefore the *ZT* is not known.[5] The strategy of optimizing *n* has led to significant improvements in the thermoelectric power factor and *ZT* of p-type organic thermoelectric materials. Further improvements will require a better understanding of what factors determine the optimum value for *n*, and how these factors can be tuned to shift the entire trend of σ and α on *n* to achieve even greater values for $\sigma\alpha^2$.

Devices made from both organic p-type and n-type thermoelectric materials are necessary to attain the full benefits of organic thermoelectric materials' light weight, flexibility, and availability from abundant resources, but the performance of n-type organic thermoelectric materials is lagging significantly behind in performance. A power factor of 33.3 μW m^{-1} K^{-2} has recently been reported for the n-type thermoelectric small molecule 2DQTT-*o*-OD doped with $(2\text{-Cyc-DMBI-Me})_2$, with a *ZT* of 0.02.[6] The n-type small molecule A-DCV-DPPTT doped with N-DMBI has recently been reported to reach its maximum power factor of 236 μW m^{-1} K^{-2} at °C, resulting in a *ZT* of 0.23.[7] The authors attribute this remarkably high power factor, in part, to ability to control the doping of solid state aggregates of A-DCV-DPPTT using the N-DMBI$^{\bullet}$ radical. A power factor of 28 μW m^{-1} K^{-2} has recently been reported for the n-type polymer FBDPPV doped with N-DMBI.[8] These results have all been attributed to the high electron mobility

of the n-type semiconductor and to the careful energy level alignment between the LUMO of the n-type semiconductor and the HOMO or SOMO level of the dopant. A power factor of 1,050 $\mu W\ m^{-1}\ K^{-2}$ and ZT of 0.5 has also been reported for PEDOT composites with carbon nanotubes doped with TDAE.[9] Although some of these power factors and *ZT*s are remarkably high for n-type organic thermoelectric materials, these n-type materials can only be tested in the absence of air, presumably due to their instability in air caused by the oxidation of the n-doped semiconductor by oxygen. An added and unique challenge for improving n-type organic thermoelectric materials is, therefore, to prepare semiconductors with such low-LUMO levels that oxygen will not accept an electron from the n-doped semiconductor.

In this dissertation, I describe my Ph.D. research results that address the current needs in the field of organic thermoelectric materials of understanding α vs. σ trends and of synthesizing and doping n-type organic semiconductors that are persistent in their radical anion, doped state in the presence of air. In Chapter 2, I describe the synthesis of n-type organic copolymers designed using rylenediimide units with a vinylene spacer and how tuning the LUMO levels of these copolymers enables their chemical doping into radical anion copolymers that persist under ambient conditions. The polymers I describe in Chapter 2 – PDNDIV, PFNDIV, and PDIV – could be chemically doped under ambient conditions, became electrically conductive under ambient conditions after doping, and persisted as chemically doped radical anions on a timescale of days to one week. In Chapter 3, I describe the charge transport in blends of the n-type organic polymer PBTDV2 with carbon nanotubes. The charge transport in these blends was p-type, based on the sign of α, which is consistent with the carrier type in oxygen-doped

carbon nanotubes and inconsistent with the previously reported n-type carrier in PBTDV2. The dependence on carbon nanotube concentration in these blends is consistent with that of P3HT blends with carbon nanotubes. In Chapter 4, I describe methodology to obtain α vs. σ trends for the organic polymers P3HT and PDPP4T by making in situ measurements of the iodine doped samples as they spontaneously dedope over time. Modeling these trends to deduce the dopant-induced density of states (DOS) and mapping the Surface Potential Contrast (SPC) using Kelvin Probe Force Microscopy (KPFM) to measure the spatial distribution of dopants throughout the samples' surface provided us with insight into how the spatial distribution of dopants influenced the α vs. σ trends. In the final chapter of this dissertation, Chapter 5, I describe the synthesis of p-type, electrically conductive films of PEDOT:Tos and the modulation of their thermoelectric properties by electrochemical oxidation and reduction. This chapter serves as documentation of the methods we used to synthesize and electrochemically oxidize and reduce PEDOT:Tos, however, the range of α and σ we obtained was too narrow for useful modelling.

CHAPTER 2

DESIGN AND SYNTHESIS OF N-TYPE CONDUCTING POLYMERS WITH PERSISTENT RADICAL ANIONS

2.1 Overview

In this chapter, I describe the design and synthesis of electron transporting polymers in the DV Group based on electron deficient rylenediimide units bridged by vinylene spacers. This research was a continuation of the DV Group's previous research into electron transporting polymers,[10-11] with a new focus on tailoring the LUMO levels of the polymers to enable chemical doping and persistence of the chemically doped radical anion polymers under ambient conditions. This was motivated by the current lack of n-type polymers with a high thermoelectric power factor. Although the polymers prepared in this research could be chemically doped under ambient conditions, their electrical conductivities were too low to enable measurements of their Seebeck coefficients (α).

The following section* describes the synthesis and properties of polymers based on naphthalenediimide with a vinylene spacer we have already reported elsewhere.[12] The final section of this chapter describes a regiorandom perylenediimide vinylene copolymer. I gratefully acknowledge Dr. Sashi Debnath, who synthesized the naphthalenediimide vinylene copolymers and carried out a significant amount of their characterization, Dr. Dongming Zhou and Prof. Kevin Kittilstved, who characterized the electron paramagnetic resonance spectroscopy, Dr. Bryan M. Wong, who performed the

* Section 2.2 was adapted from Ref. 12: Debnath, S.; Boyle, C. J.; Zhou, D.; Wong, Bryan M.; Kittilstved, K. R.; Venkataraman, D., Persistent radical anion polymers based on naphthalenediimide and a vinylene spacer. *RSC Adv.* **2018,** *8* (27), 14760-14764.

DFT calculations, and Dr. Lawrence Renna, who suggested and fabricated the home-built two-terminal Au electrodes used in these studies.

2.2 Persistent Radical Anion Polymers Based on Naphthalenediimide and a Vinylene Spacer

Doped conjugated polymers with excess electronic charge carriers are essential for many organic electronic applications such as organic thermoelectrics that require enhanced electrical conductivity. Applications for organic electronics require either p-doped (doping with positive charge carriers, holes) or n-doped (doping with negative charge carriers, electrons) polymers or both. Many conjugated polymers can be p-doped with ease using chemical or electrochemical methods. Several of these polymers retain their p-doping at ambient conditions making it easier to incorporate them into devices. On the other hand, obtaining stable n-doping in conjugated polymers is a challenge because many conjugated polymers have a low electron affinity. Thus, chemical n-doping requires very reactive dopants, and the doped polymers can easily de-dope by transferring the electrons to other molecules such as oxygen. Therefore, examples of extrinsically n-doped polymers[8, 13-16] are sparse and often require doping under dry nitrogen or argon. Recently, Katz and co-workers[17] reported an n-doped polymer that they claimed to be the first demonstrated example of an air-stable n-doped polymer. This section focuses on a different class of naphthalenediimide-based polymers that can be n-doped under ambient conditions. The important role of side chains in tuning and enhancing the air-stability of the doped polymers is also demonstrated.

The DV Group has previously reported a straightforward route to electron-transporting polymers from readily available electron accepting monomers and vinylene

spacers.[10] Using this route, and monomers containing naphthalene diimide (NDI) units, we designed two new naphthalene diimide-vinylene (NDIV) copolymers. We chose to incorporate vinylene spacers instead of electron-rich donor units since vinylene groups impose planarity of the conjugated polymer while maintaining a high electron affinity. We chose to utilize two NDI monomers, one with alkyl hydrocarbon side chains on both imide nitrogens [*N*,*N*′-bis(*n*-dodecyl)-2,6-dibromo-1,4,5,8-naphthenedicarboximide (DNDI)] and the other with an alkyl fluorocarbon on one imide nitrogen and an alkyl hydrocarbon chain on the other imide nitrogen [*N*-(2,2,3,3,4,4,4-heptafluorobutyl)-*N*′-octadecyl-2,6-dibromo-1,4,5,8-naphthenedicarboximide (FNDI)]. We chose naphthalene diimide because it has been shown to form stable radical anions.[18-20] Based on the work by Katz and co-workers,[21] we hypothesized that the fluorocarbon sidechain will lower the lowest unoccupied molecular orbitals (LUMO), increase the electron affinity, and thus chemical stability of the n-doped polymer. To shed additional insight into the electronic properties of these systems, we carried out first-principles density functional theory (DFT) calculations on a series of oligomers ranging from 1 to 6 monomer units for both the FNDI and DNDI systems. Both the electron affinity and the spin density (see Figure 2) were computed at the ωB97XD/6-31g(d,p) level of theory,[22] which has been previously benchmarked for a variety of charged, conjugated organic systems.[23-24] Based on our DFT calculations, we found that oligomers with FNDI had an electron affinity that was 0.2 eV higher than oligomers with DNDI.

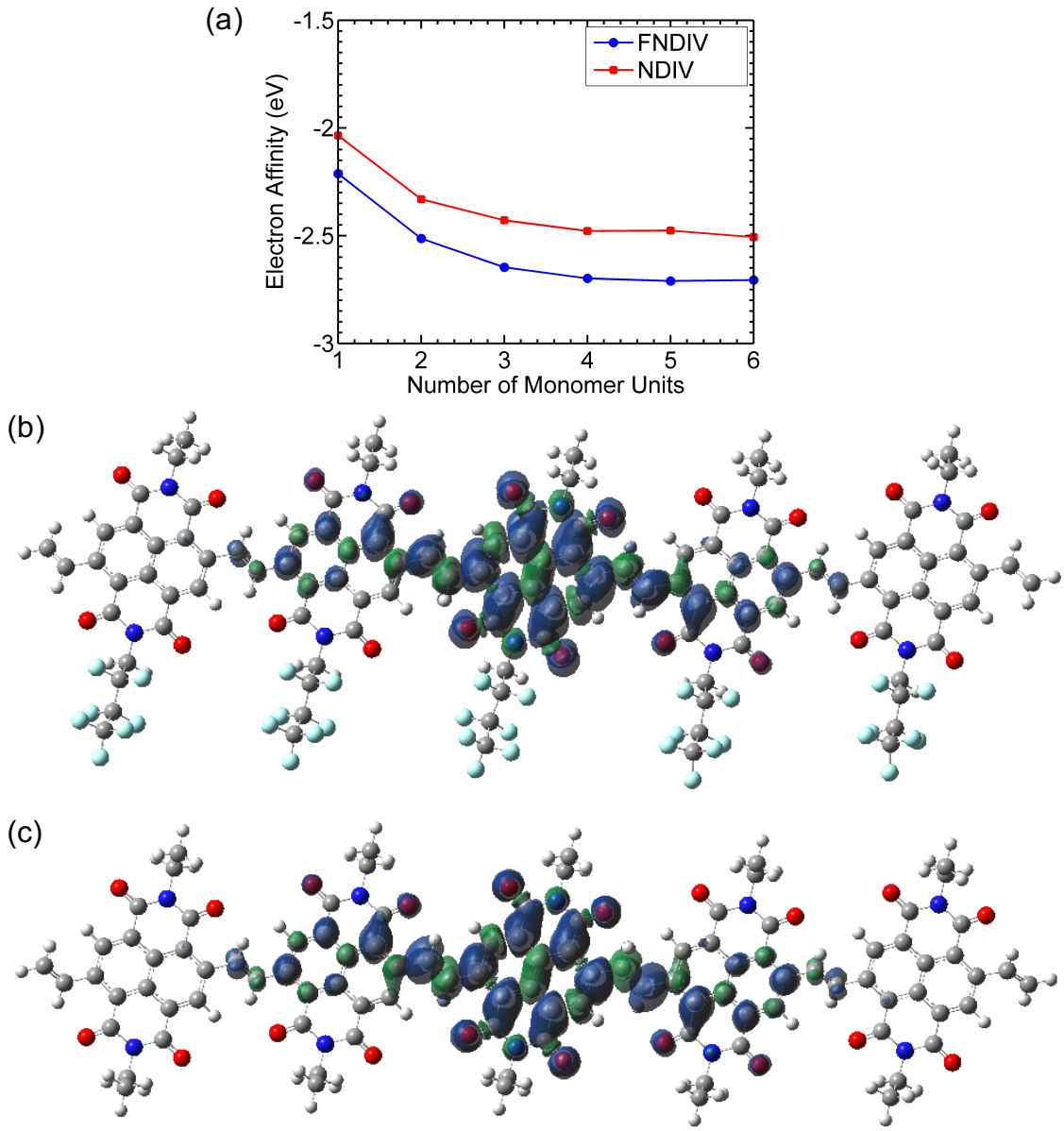

Figure 2: (a) DFT calculated electron affinity of DNDIV and FNDIV oligomers modelled with increasing naphthalene diimide units. (b) Optimized geometry and molecular orbital spin density difference plots including positive spin density (green orbital) and negative spin density (blue orbital) for the 5-mer of $[FNDIV]^{\bullet-}$ and (c) $[DNDIV]^{\bullet-}$.

The polymers, poly[*N*,*N*′-bis(*n*-dodecyl)-1,4,5,8-naphthalenedicarboximide-2,6-diylvinylene] (PDNDIV) and poly[*N*-(2,2,3,3,4,4,4-heptafluorobutyl)-*N*′-octadecyl-1,4,5,8-naphthalenedicarboximide-2,6-diylvinylene] (PFNDIV) were synthesized using

previously reported methods (see Figure 3).[10, 25] The polymers were doped by chemical reduction using either tetrabutylammonium cyanide (TBACN)[26-28] or tetrakis(dimethylamino)ethylene (TDAE).[16, 29] Consistent with our hypothesis, we found that the incorporation of a fluorinated side chain in PFNDIV increased the electron affinity, as indicated by its decreased LUMO energy level (−4.27 eV), estimated from electrochemical measurements. Each polymer showed well-defined spectroscopic changes after gradual addition of either dopant due to the formation of radical anions, which were confirmed by EPR. Both of the doped polymers exhibit signatures of the radical anion for several days in THF under ambient conditions.

2.2.1 Synthesis and Characterization of Naphthalenediimide Vinylene Copolymers

The synthetic scheme for DNDI, FNDI, PDNDIV, and PFNDIV are shown in Figure 3 and the experimental procedures are described in Appendix A, the Experimental Section. The molecular weights of the polymers were measured by high temperature gel permeation chromatography (GPC) using 135 °C 1,2,4-trichlorobenzene as the mobile phase and summarized in Table 1.

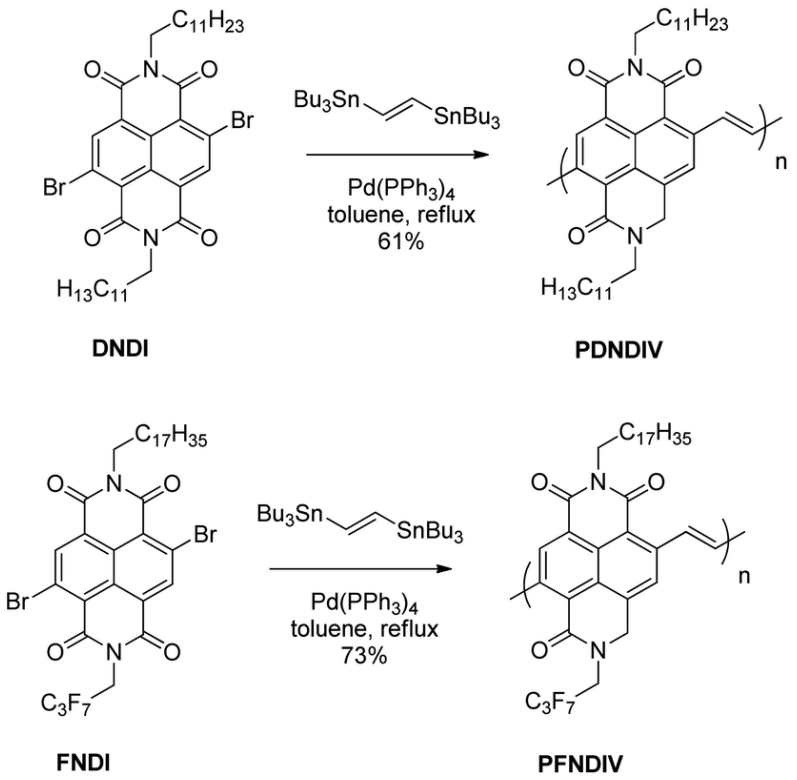

Figure 3: Scheme of the synthesis of PDNDIV and PFNDIV by Stille reaction.

Table 1: Molecular mass distribution of the polymers

Polymer	M_n **(g/mol)**	M_w **(g/mol)**	$Đ$
PDNDIV	10,622	18,836	1.77
PFNDIV	8,304	15,927	1.91

The thermal stability of PDNDIV and PFNDIV was determined by using thermogravimetric analysis (TGA) with a heating rate of 10 °C min^{-1} under nitrogen atmosphere (see Figure 4a). TGA curves showed that the decomposition temperatures (T_d, at which 5% weight loss occurred) for PDNDIV and PFNDIV were found to be 239 and 279 °C, suggesting sufficient thermal stability of the polymers. Differential scanning calorimetry (DSC, see Figure 4b and 4c) and powder X-ray diffraction patterns (see

Figure 5) of the polymers did not show any distinguishing peaks, which indicates that the solid-state structure of the polymers are amorphous.

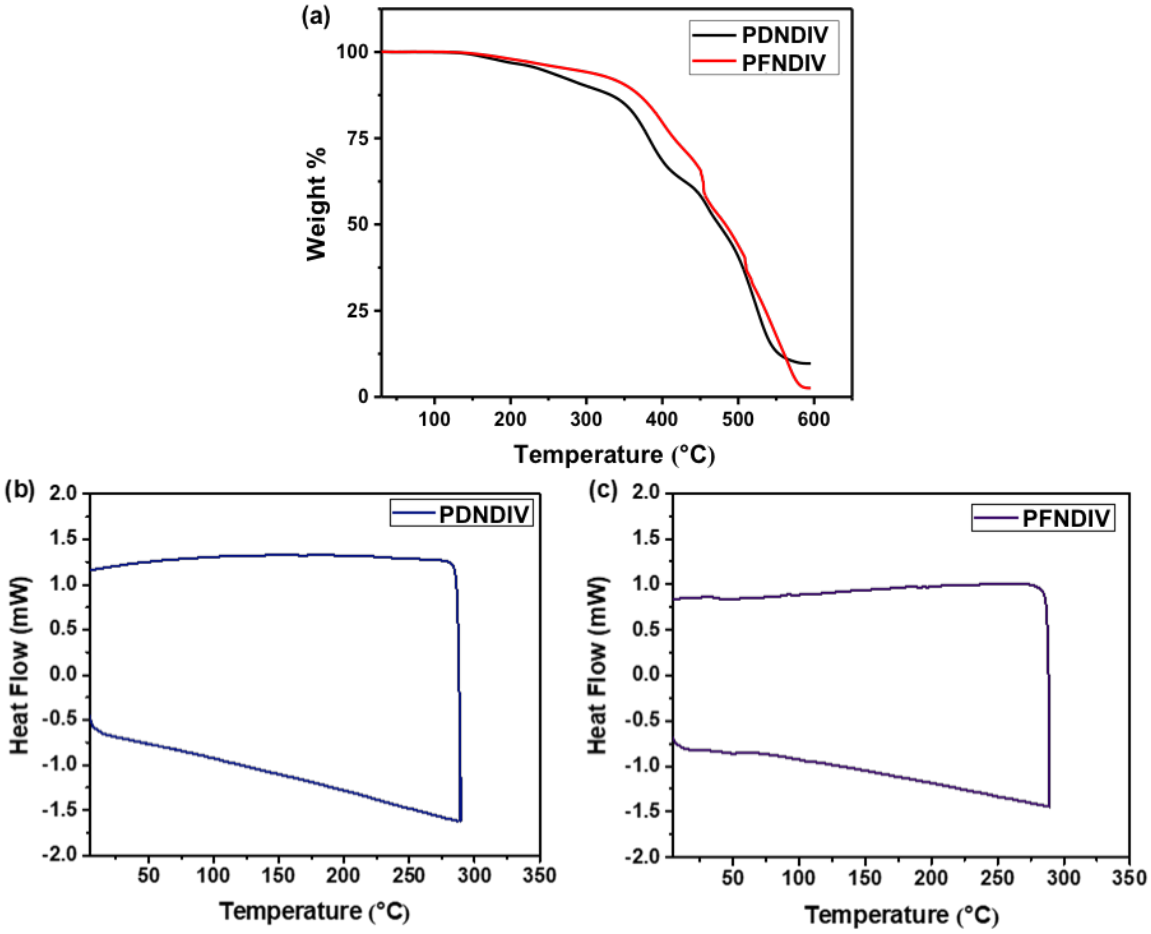

Figure 4: (a) TGA thermograms of PDNDIV and PFNDIV (b) DSC plots of PDNDIV, (c) DSC plots of PFNDIV at heating rate of 10 °C min^{-1} under a N_2 atmosphere.

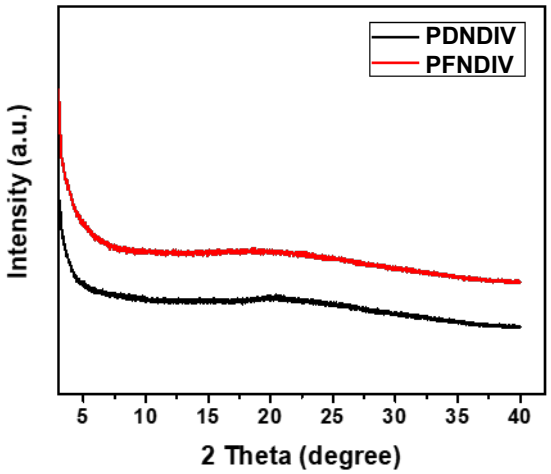

Figure 5: XRD patterns of PDNDIV and PFNDIV at ambient temperature.

2.2.2 Optoelectronic Properties of Naphthalenediimide Vinylene Copolymers

The UV-Vis absorption spectra of each polymer in dilute chloroform solution (10^{-5} M on the basis of repeating units) and of thin films on glass substrates coated with indium tin oxide (ITO) is shown in Figure 6a. Both polymers showed two distinctive absorption bands, one in the blue region from 300–400 nm and the other in the red region 450–650 nm. We attribute these absorption to π–π* transitions of the NDI chromophore and electronic transitions between new delocalized bands in the polymer backbone,[30] respectively (Table 2). A distinct broadening and red shift of the low energy transitions by 10–20 nm is observed in the polymer films, which indicates chromophore aggregation caused by interactions between the chains in the solid-state.[31] The optical band gaps (E_g) obtained from the Tauc plot (see Figure 6a inset) are 2.11 eV for PDNDIV and 2.04 eV for PFNDIV. The reduced E_g value of PFNDIV compared to that of PDNDIV was attributed to the presence of the electron-withdrawing fluorinated side chain, which can lower the LUMO energy level through inductive effects.[21]

Table 2: Optical and electrochemical properties of the polymers

Polymer	λ_{max} Solution (nm)	λ_{max} Film (nm)	$E_{reduction}$ (eV)	[a]E_{HOMO} (eV)	[b]E_{LUMO} (eV)	[c]E_g (eV)
PDNDIV	322, 500	330, 509	−0.392	−6.07	−4.09	1.98
PFNDIV	325, 506	338, 524	−0.208	−6.16	−4.27	1.89

$$E_{LUMO} = -4.8\ eV - (E_{reduction} - 0.32\ eV) \quad (1)$$

$$E_{HOMO} = E_{LUMO} - E_g \quad (2)$$

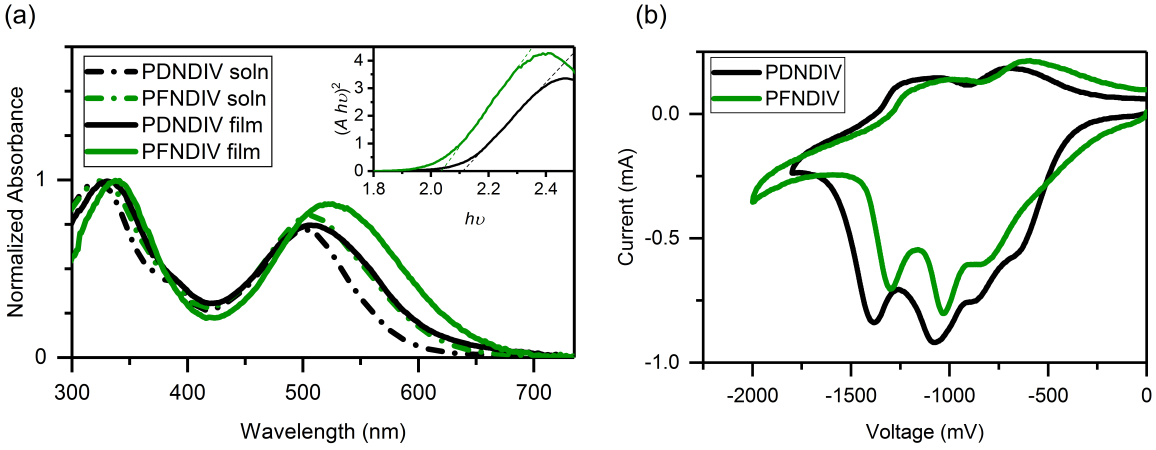

Figure 6: (a) UV-Vis spectra of the polymers in 10^{-5} M chloroform solution and as thin films on ITO coated glass. The Tauc plot of the film spectra, assuming $r = 1/2$ for a direct allowed transition, including the dashed trace used to determine the bandgap is inset. (b) Cyclic voltammograms of the polymer film dropcast onto a Pt disk (1.6 mm diameter) electrode as the working electrode, using Pt wire as the counter electrode, Ag/AgCl as the reference electrode, and 0.1 M tetrabutylammonium perchlorate as the supporting electrolyte at a scan rate of 50 mV s^{-1}, reduction only scans.

Cyclic voltammograms (CV) of the polymer films are shown in Figure 6b. There were multiple reduction onsets in the CV, indicating that polymers can be consecutively reduced by up to 4 electrons in acetonitrile. LUMO energies of both the polymers were calculated from their first onset reduction potentials (see Equation 1) as −4.09 eV

for PDNDIV and −4.27 eV for PFNDIV. The HOMO energy levels were estimated by subtracting the E_g from the above CV-determined LUMO energy levels and were found to be −6.20 eV for PDNDIV and −6.31 eV for PFNDIV (see Equation 2). CV data showed that both polymers are positioned at low-lying LUMO levels and the electron withdrawing *N*-substituents impart a significant impact on PFNDIV's superior π-acidity, which is evident from additional diminution in reduction potential.

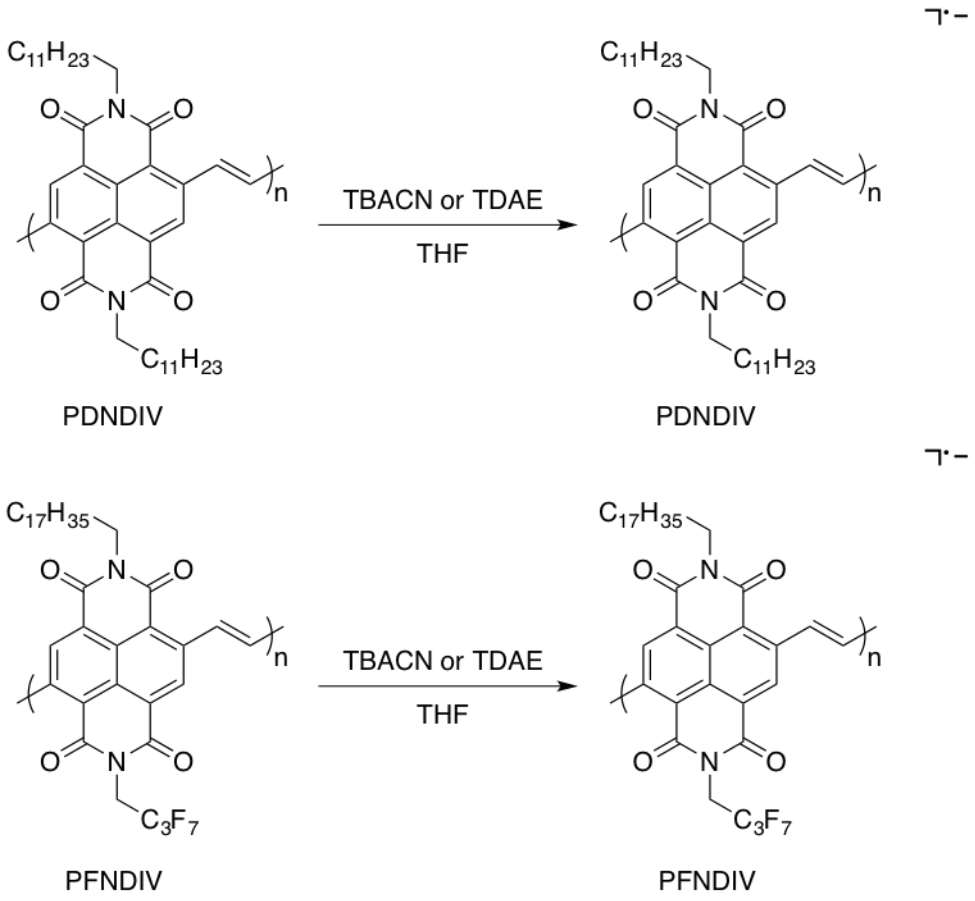

Figure 7: Synthesis of [PDNDIV]$^{\bullet-}$ and [PFNDIV]$^{\bullet-}$ under ambient condition in THF using TBACN or TDAE.

2.2.3 Characterization and Stability Study of Radical Anion Naphthalenediimide Vinylene Copolymers

The polymers were doped using TDAE, a neutral electron donor, or TBACN, an anionic electron donor, under ambient conditions (see Figure 7). TDAE[26-28] and TBACN[16, 29] have been used as electron donors for rylenediimides, and their proposed mechanism of doping is a single electron transfer. In the UV-Vis-NIR spectra, we found that the continuous addition of 0–1.4 equivalents (with respect to the polymer's repeating units) of TBACN with PFNDIV, progressively bleached the neutral polymer absorption band (450–650 nm) and simultaneously produced a new absorption band at 750 nm, with an isosbestic point near 600 nm (see Figure 8). A similar behavior was observed for PDNDIV, but with larger numbers of equivalents (0–10) of TBACN (see Figure 8) required to produce similar spectral changes.

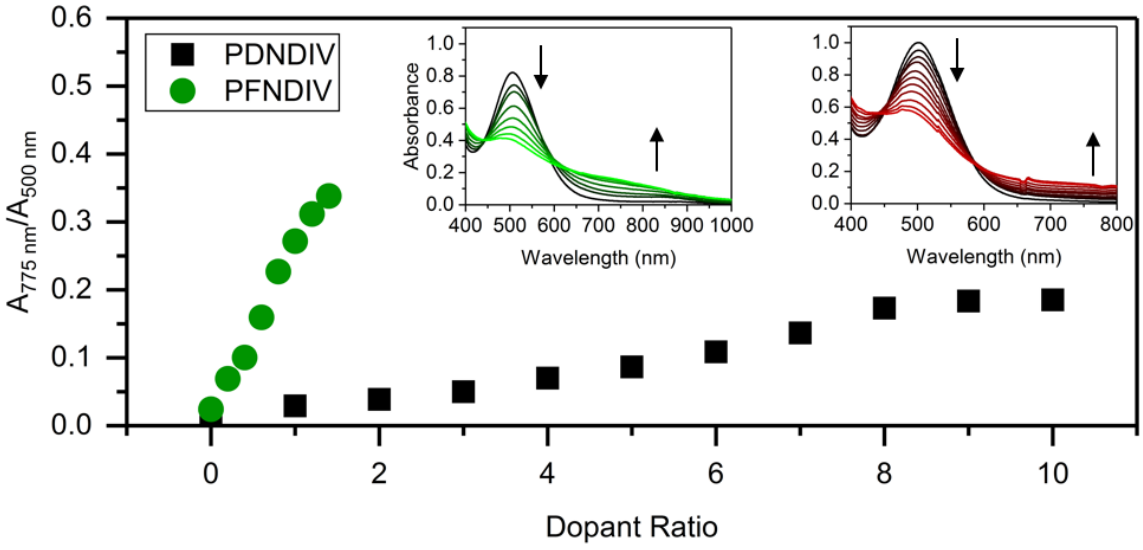

Figure 8: Ratio of doped to undoped repeating units, estimated by UV-Vis-NIR spectroscopic changes, for PDNDIV and PFNDIV in THF with increasing molar equivalents of TBACN; insets are the UV-Vis-NIR spectra for PFNDIV (left) and PDNDIV (right).

The formation of a weaker absorption band at ~750 nm suggests the formation of the radical anion polymers $[PDNDIV]^{\bullet-}$ and $[PFNDIV]^{\bullet-}$ (Figure 8), which was also confirmed by EPR spectroscopy (vide infra). The addition of TDAE also resulted in an instantaneous color change of the polymer solution (see inset Figure 9), which is consistent with an n-doped polymer. TDAE-doped radical anion polymers were also characterized by UV-Vis-NIR absorption (Figure 9) and EPR spectroscopy (Figure 10).

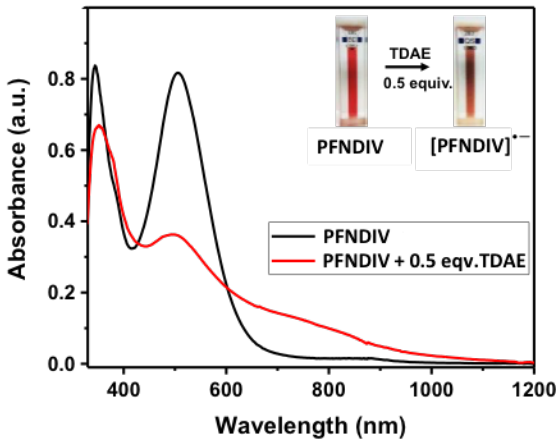

Figure 9: UV–Vis–NIR spectroscopic changes of PFNDIV in THF with TDAE dopant, inset TDAE induced colorimetry.

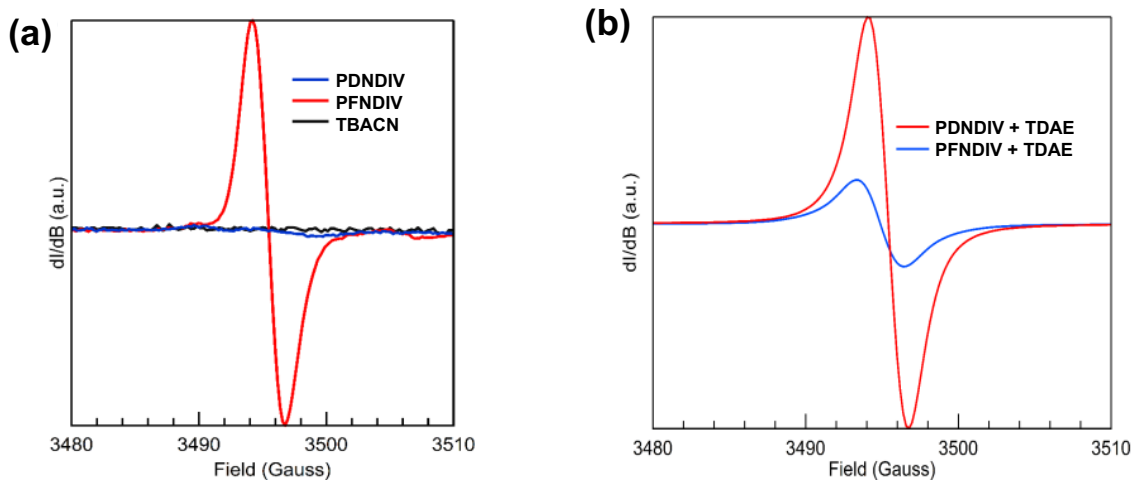

Figure 10: (a) Control EPR spectra of PDNDIV, PFNDIV and TBACN, in THF. (b) EPR spectrum of $[PDNDIV]^{\bullet-}$ and $[PFNDIV]^{\bullet-}$ in THF (TDAE induced).

EPR spectroscopy was used to probe the formation of a radical anion and monitor the relative stability of the radical under ambient conditions over time. The EPR spectra of the polymers after addition of TBACN are shown in Figure 11. Both PDNDIV and PFNDIV display a single, narrow resonance at $g = 2.0035$ upon mixing with TBACN, which indicates the formation of $[PDNDIV]^{\bullet-}$ and $[PFNDIV]^{\bullet-}$ radical anions. The absence of any hyperfine splitting indicates that the spin density of the radical anion is localized on the carbon of the aromatic ring. DFT calculations performed with the ωB97XD/6-31g(d,p) basis verify the nature of the SOMO as shown in the difference plots of the molecular orbital spin density (Figure 2). Both polymer radical anions are persistent as THF solutions stored in air, but the radical signal of $[PFNDIV]^{\bullet-}$ is more stable with an apparent half-life on the order of one week (Figure 11b), comparable to the stability of the recently reported n-type polymer, ClBDPPV.[17] The decay of the radical EPR signal is tentatively assigned to quenching by triplet oxygen. The difference in radical stabilities could possibly originate from variation in the reduction potentials of the LUMOs of $[PDNDIV]^{\bullet-}$ and $[PFNDIV]^{\bullet-}$, with the more negative LUMO on PFNDIV.

Interestingly, the EPR spectrum of the as-prepared PFNDIV displays the same radical signal and suggests PFNDIV can be partially doped under ambient conditions while PDNDIV displays no signal (Figure 10a).

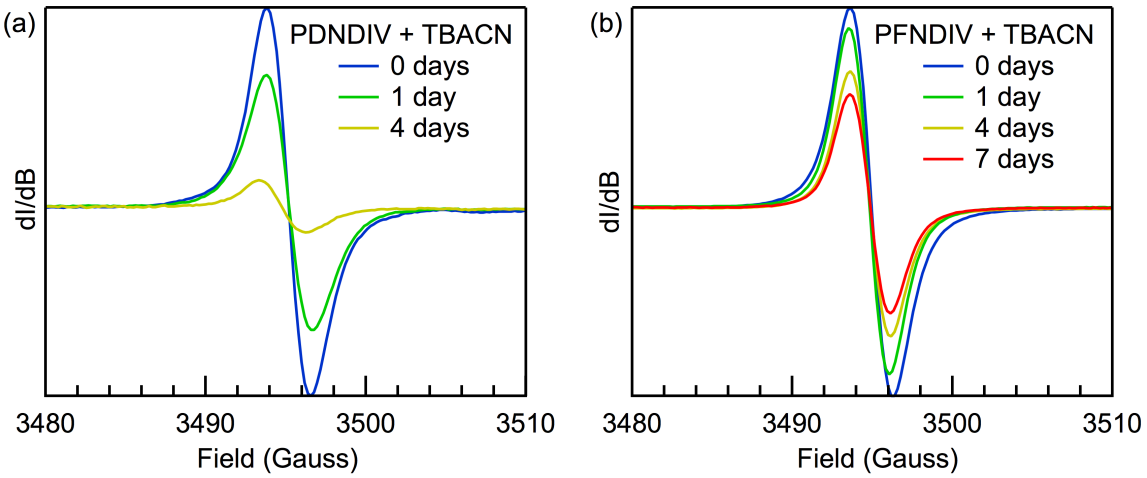

Figure 11: Room-temperature X-band EPR spectra of (a) 2 mM (repeating units) PDNDIV with 10 mM TBACN and (b) 2 mM PFNDIV with 2 mM TBACN in THF yielding $[PDNDIV]^{\bullet-}$ and $[PFNDIV]^{\bullet-}$, respectively. The 7 day point for $PDNDIV]^{\bullet-}$ is omitted and unreliable due to polymer precipitation.

We then studied the impact of the concentration of TBACN on the intensity of the EPR signal (see Figure 12). For PDNDIV we found that 1 equivalent of TBACN with respect to polymer repeating units was insufficient to dope the polymer. At higher concentrations, we observed an EPR signal, which indicated the formation of the radical anion. The intensity of the signal increased steadily with increasing concentration of the dopant. This observation is consistent with the presence of an equilibrium, with a slight preference for the reactants. This is consistent with the expected LUMO energy levels of PDNDIV and the cyanide anion of TBACN. In the case of PFNDIV, we found a steady increase in the EPR signal up to 1 equivalent of the TBACN. Further increase of the cyanide concentration led to a decrease in the EPR signal. From CV studies, we know that the polymer can accept up to four electrons. Therefore, we tentatively attribute this

decrease in $[PFNDIV]^{\bullet-}$ EPR signal with increasing TBACN concentration to the formation of an EPR-silent singlet or triplet $[PFNDIV]^{2-}$ species.

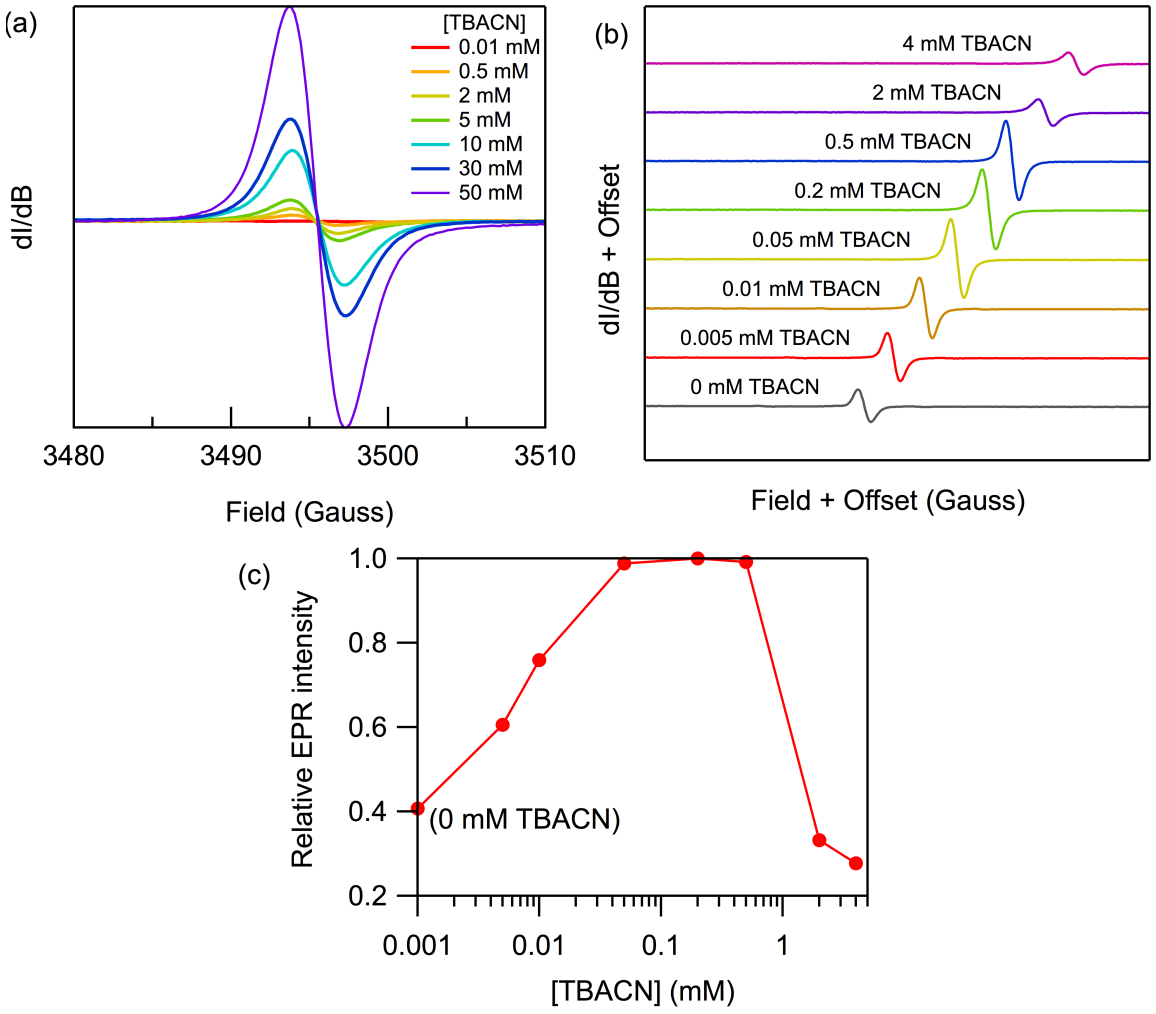

Figure 12: Room-temperature X-band EPR spectra of (a) PDNDIV (2 mM) and (b) PFNDIV (0.5 mM) after mixing with increasing concentration of TBACN in THF. (c) Normalized EPR intensity of PFNDIV (0.5 mM) with increasing concentration of TBACN in THF.

2.2.4 Conductivity of Radical Anion Naphthalenediimide Vinylene Copolymers

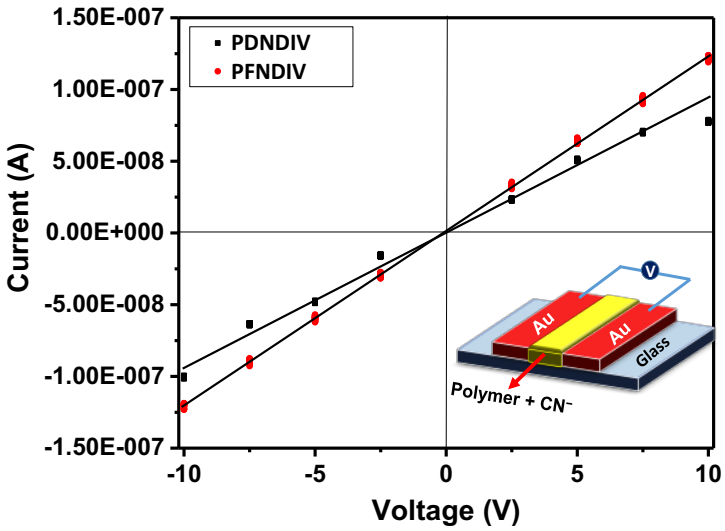

Figure 13: *I-V* curves of $[PDNDIV]^{\bullet-}$ and $[PFNDIV]^{\bullet-}$ doped using TBACN.

To investigate the solid-state conductivity of these radical anion polymers under ambient conditions, we fabricated two-terminal devices using vacuum depositing Au electrodes (see Figure 13 inset) using neutral or doped PDNDIV or PFNDIV acting as the active layer. Either the neutral (see Figure 14) or doped (see Figure 13) polymers were drop-cast from THF on the fabricated channels, and current (*I*)–voltage (*V*) measurements were carried out under ambient conditions. To ensure that only the electronic contribution, and no ionic contribution, to the conductivity was considered, the sample was poled at a constant voltage to ensure the decay of any ionic current (see Figure 15 and Figure 16) and only the final 2.5 seconds of current measured was used for the *I-V* plot.

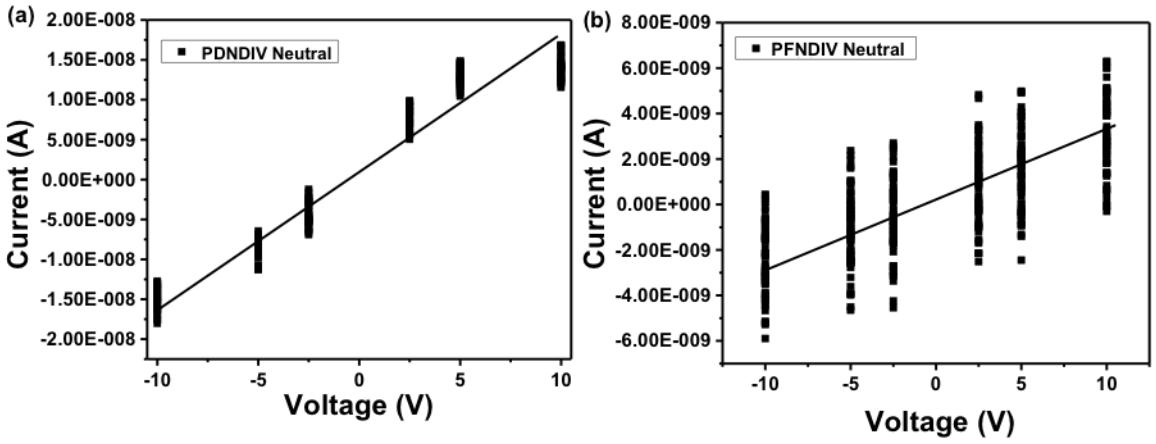

Figure 14: *I-V* curves of PDNDIV (a) and PFNDIV (b) in absence of any dopant.

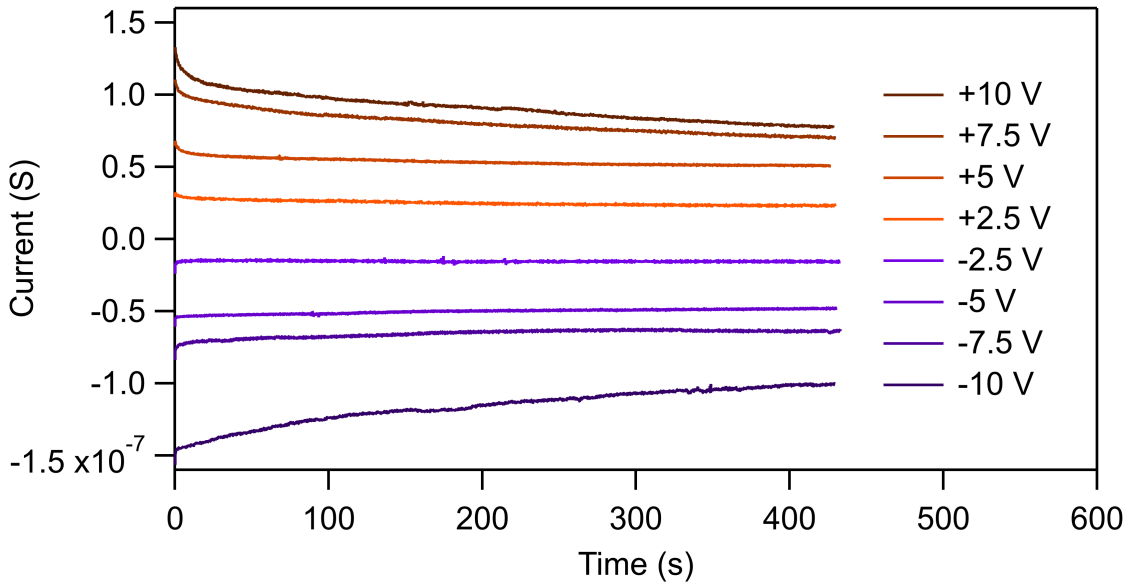

Figure 15: Current response of $[PDNDIV]^{\bullet-}$ to a constant applied voltage over time.

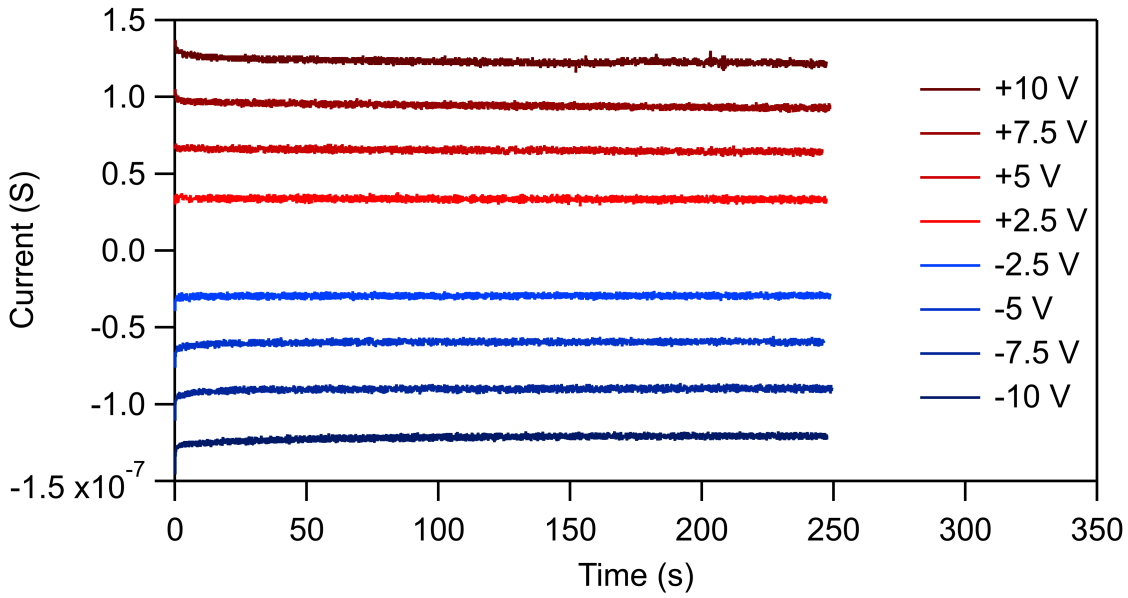

Figure 16: Current response of $[PFNDIV]^{\bullet-}$ to a constant applied voltage over time.

The conductivity of each doped polymer (see Table 3) was at least an order of magnitude greater than the conductivity of the neutral polymers. While these conductivities are lower than those of other reported n-doped conjugated polymers and are too low for practical applications, the drastic increase in conductivity upon doping and the air stability of the doped polymers suggests that these and similar NDI-vinylene polymers may find potential use as n-type organic electronic materials. The low conductivities may be due, in part, to the amorphous nature of these polymers in the solid state.

Table 3: Conductance, Conductivity, and Film Thickness of PDNDIV and PFNDIV in Presence of TBACN.

Polymer	Equivalents of TBACN	Conductance (S)	Conductivity (S cm^{-1})	Thickness (μm)
PDNDIV	0.0	1.64×10^{-9}	3.49×10^{-8}	15.5
PDNDIV	4.0	9.01×10^{-9}	6.98×10^{-7}	4.26
PFNDIV	0.0	2.76×10^{-10}	2.61×10^{-8}	3.48
PFNDIV	1.0	1.22×10^{-8}	3.28×10^{-7}	12.2

In summary, two new NDI-vinylene based electron acceptor polymers have been successfully synthesized. Due to the low-lying LUMOs (−4.09 and −4.27 eV) both the polymers behave as strong π-acids. The electron-withdrawing effect of the fluorinated side chain reduces the LUMO level of PFNDIV significantly. Multistep reduction potentials indicate the presence of several electron accepting sites in the polymer backbone. Chemical reduction from electron donors to the polymer generates persistent radical anion polymers with ambient stability. Time-dependent EPR spectroscopy showed the stability of the radical anions exists beyond several days. Finally, conductivity measurements showed the positive impact of chemical doping on the polymer's electrical conductivity, making these materials promising for organic electronic applications.

2.3 Persistent Radical Anion Polymers Based on Perylenediimide and a Vinylene Spacer

Perylenediimide-based semiconductors have low-lying LUMO levels, comparable[32] to those of naphthalenediimide-based semiconductors with similar alkyl chains and bay-substituents, and have been chemically doped to achieve persistent

dianions or radical anions in small molecules[26, 28, 33-34] and polymers[35]. We chose to prepare a perylenediimide polymer with a vinylene spacer using the same strategy as our previous work in order to study its electron accepting capability and conductivity under ambient conditions. Due to the notoriously poor solubility of perylenediimide compounds and our desire to characterize and dope the polymer in solution state, we elected to synthesize a polymer with branched side chains, regiorandom regiochemistry of the repeating units, and a relatively low number of repeating units to maximize solubility. The synthesis of the polymer, poly[*N*,*N*′-bis(1-hexylheptyl)-3,4,9,10-perylenediimide-1,7/1,6-diylvinylene] (PDIV), is outlined in Figure 17 and the Experimental Procedures are described in Appendix A, in the Experimental Section. An isomeric mixture of approximately 1:4 of 1,6- to 1,7- dibromo- monomers was used for the polymerization, resulting in a regiorandom polymer. The M_n and $Đ$ of the polymer, determined by high temperature GPC using 135 °C 1,2,4-trichlorobenzene as the mobile phase, was 3,887 g/mol and 1.67, respectively. The same polymer was recently synthesized elsewhere[36] (at a higher M_n and $Đ$ due to increased monomer concentration, alternative Stille coupling catalyst, and increased reaction time) and used as an acceptor in efficient, all polymer solar cells.

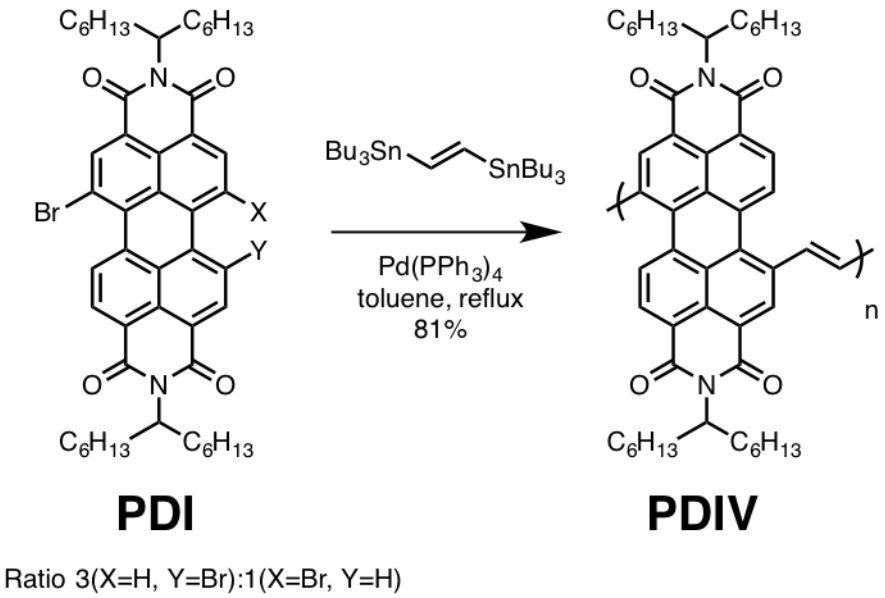

Figure 17: Scheme of the Stille coupling polymerization of PDIV. For the sake of simplicity, the structure of the of the 1,6- repeating units is omitted and only the 1,7- is shown in PDIV.

2.3.1 Optoelectronic Properties of Perylenediimide Vinylene Copolymers

The UV-Vis-NIR spectrum of a dilute THF solution of PDIV is shown in Figure 18a. PDIV has multiple, broad absorbance bands with λ_{max} appearing at 525 nm and 465 nm (a third peak which was used as the basis for normalization also appears at 240 nm, and is omitted from the range of Figure 18a for clarity). The E_g of the lowest energy transition obtained from the Tauc plot is 1.89 eV (see Figure 18a inset).

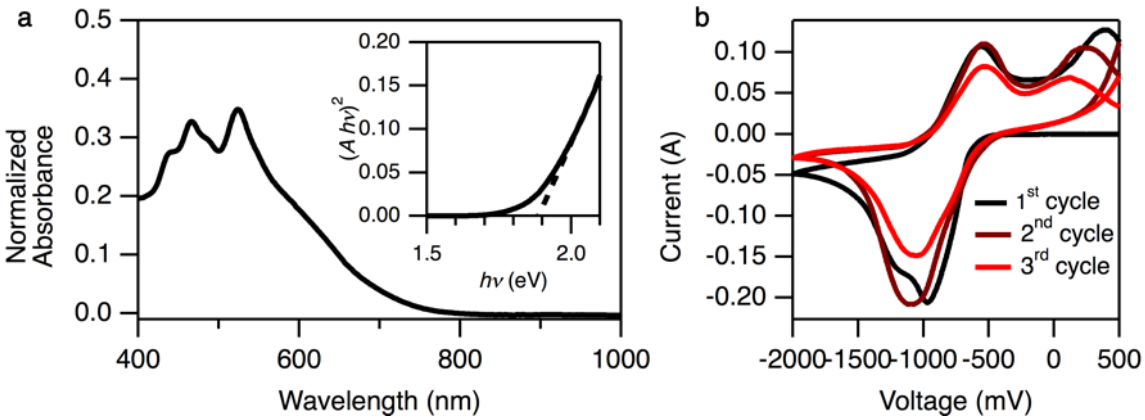

Figure 18: (a) UV-Vis-NIR spectrum of PDIV in THF solution. The Tauc plot, assuming r = ½ for a direct allowed transaction, including the dashed trace used to determine the bandgap, inset. (b) Cyclic voltammogram of a PDIV film dropcast onto a Pt disk (1.6 mm diameter) electrode as the working electrode, using Pt wire as the counter electrode, Ag/AgCl as the reference electrode, and 0.1 M tetrabutylammonium perchlorate as the supporting electrolyte at a scan rate of 50 mV s^{-1}.

The cyclic voltammogram of a PDIV film reveals a reversible reduction at an $E_{1/2}$ of -763 mV vs. Ag/AgCl (first scan). The LUMO of PDIV calculated from this reduction potential from Equation 1 is -3.72 eV, and the HOMO calculated from Equation 2 is -5.60 eV. The appearance of many overlapping absorbance bands in the UV-Vis-NIR spectrum, the marginally increased E_g compared to PDIV in the literature (1.74 eV), and the marginally increased LUMO compared to PDIV in the literature (-4.03 eV) altogether indicate that the PDIV we synthesized has a distribution of repeating unit lengths that is predominantly below the effective conjugation length.[37-38] This is consistent with the estimated number average repeating unit length of ~5 repeating units, obtained by dividing the GPC M_n (3,887 g/mol) by the repeating unit molecular weight (779.06 g/mol).

2.3.2 Characterization and Stability Study of Radical Anion Perylenediimide Vinylene Copolymers

When PDIV is mixed with TBACN in THF under ambient conditions, it responds with bleaching of its 525 nm and 465 nm UV-Vis absorbance bands and displays a new NIR absorbance band with λ_{max} at 780 nm, which we attribute to the formation of the radical anion $[PDIV]^{\bullet-}$ (see Figure 19). We verified the formation of the radical anion by EPR spectroscopy (see Figure 20). The solution of PDIV in THF with no TBACN has no EPR signal, confirming that the EPR signals from solutions of PDIV and TBACN in THF are from the radical anion resulting from electron transfer from TBACN to PDIV. Although the overall trend in EPR spectroscopic intensity versus concentration TBACN mixed with PDIV is increasing, the 4 mM TBACN does not follow this trend. The EPR signal persists for at least 6 days after doping, as shown in Figure 21, confirming the radical anion on the polymer persists in THF solution under ambient conditions.

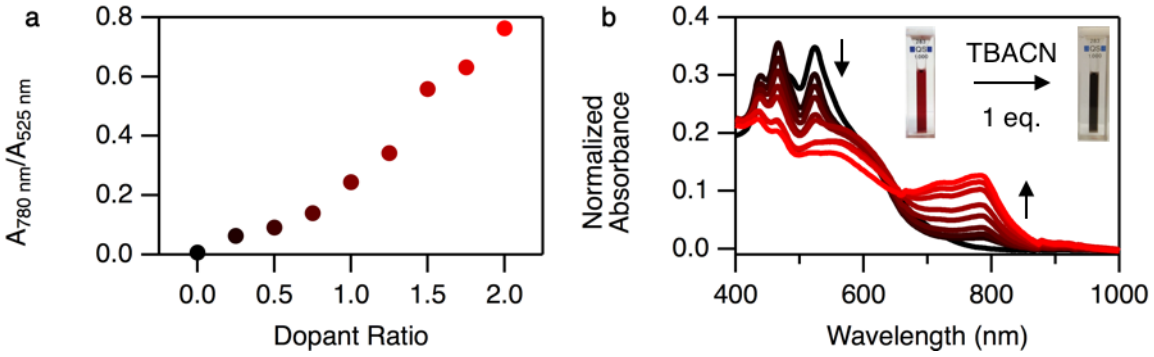

Figure 19: UV-Vis-NIR spectroscopic response of PDIV in THF solution to increasing stoichiometric equivalents of TBACN dopant. (a) Ratio of $A_{780\ nm}/A_{525\ nm}$ intensities and (b) UV-Vis-NIR spectra of PDIV mixed with dopant from 0 to 2 molar equivalents (with respect to PDIV repeating units), with a colorimetric comparison of 0 and 1 equivalent inset.

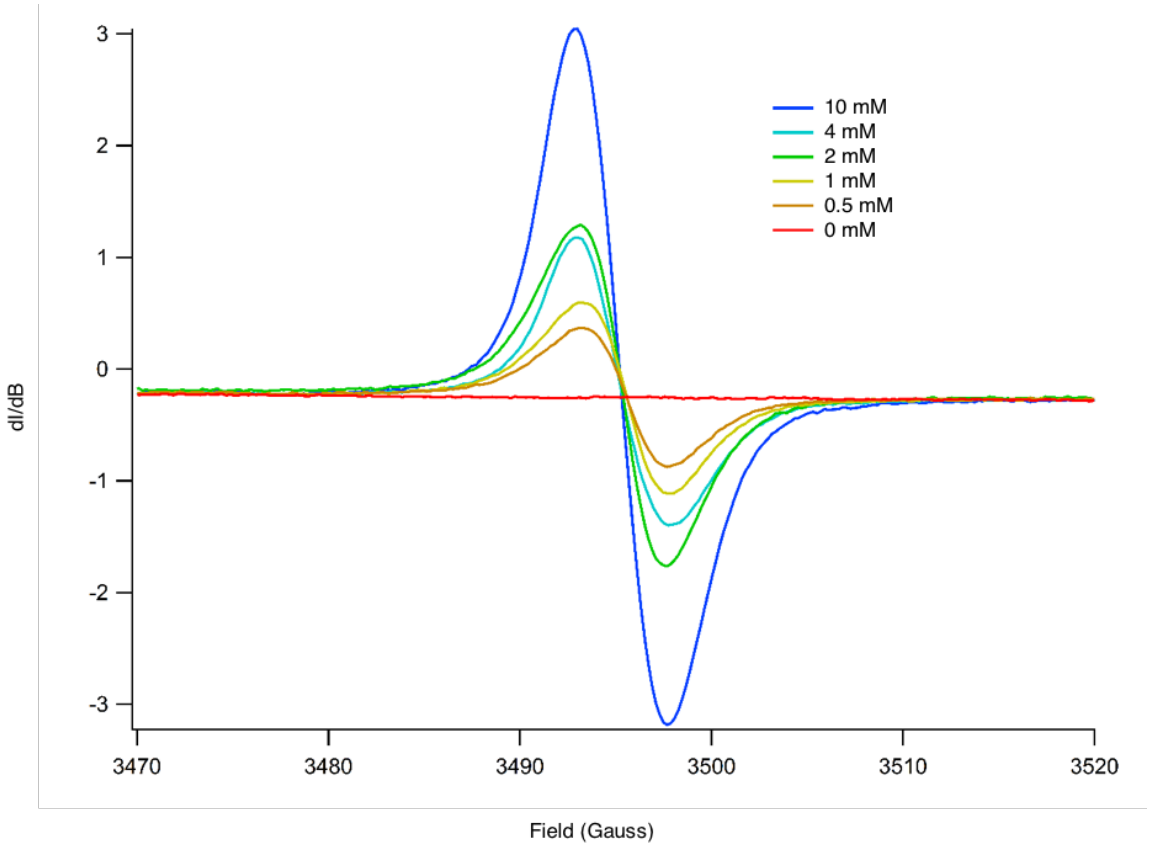

Figure 20: Room temperature X-band EPR spectra of 1 mM PDIV after mixing with increasing concentration of TBACN in THF.

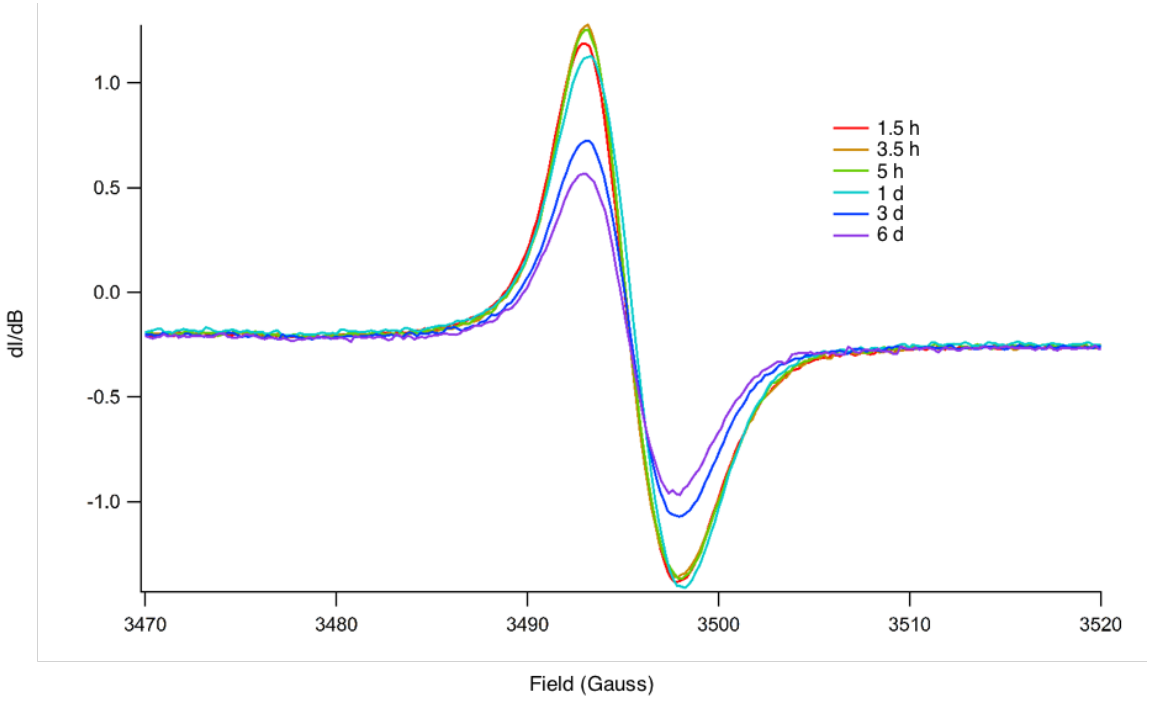

Figure 21: Room temperature X-band EPR spectra of 1 mM PDIV after mixing with 4 mM TBACN in THF under ambient conditions, over time.

2.3.3 Conductivity of Radical Anion Perylenediimide Vinylene Copolymers

A film of doped PDIV was prepared on a two-terminal Au electrode device. PDIV was doped in THF solution using 4 molar equivalents of TBACN and then dropcast onto the device. *I-V* characterization was carried out by poling the device at a constant voltage for an extended time to ensure the decay of the ionic component of the conductivity (see Figure 22). The rapid and decay of the current to less than half its initial magnitude, at each of the applied voltages, suggests the ionic conductivity of PDIV doped with TBACN is significant relative to its electrical conductivity. The electrical conductivity determined from the *I-V* curve, using only the final 30 sampled currents at each voltage (see Figure 23a), and the device dimensions (length = 165 µm, width = 5 mm, thickness

= 8.93 µm) was 8.50×10^{-5} S cm^{-1}. A film of undoped PDIV was also prepared and characterized the same way, and had a conductivity of ~0 S/cm (see Figure 23b).

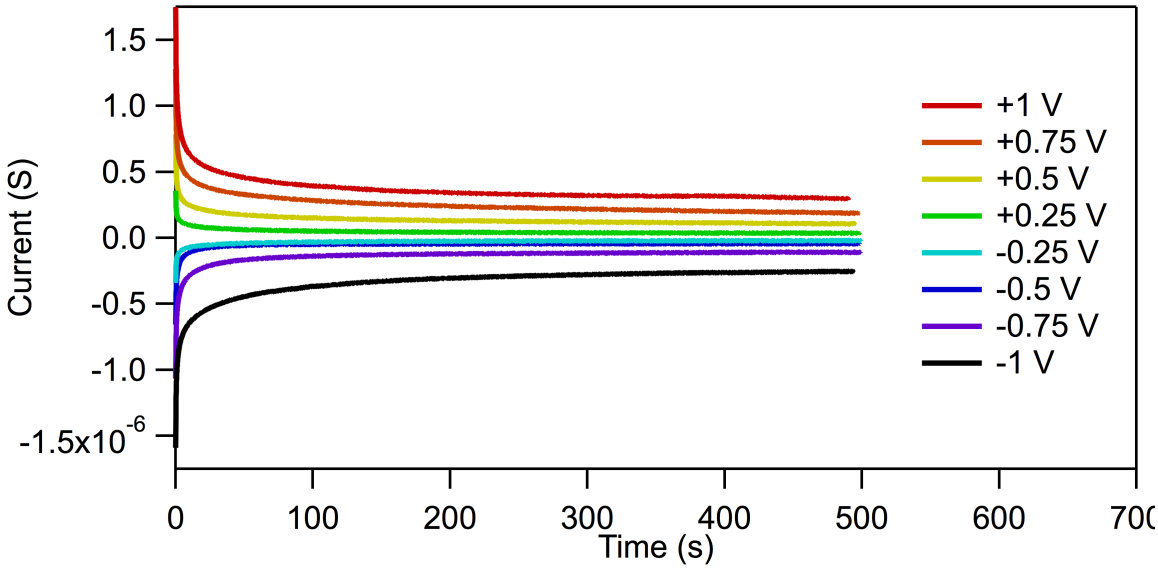

Figure 22: Current response of $[PDIV]^{\bullet-}$ to a constant applied voltage over time.

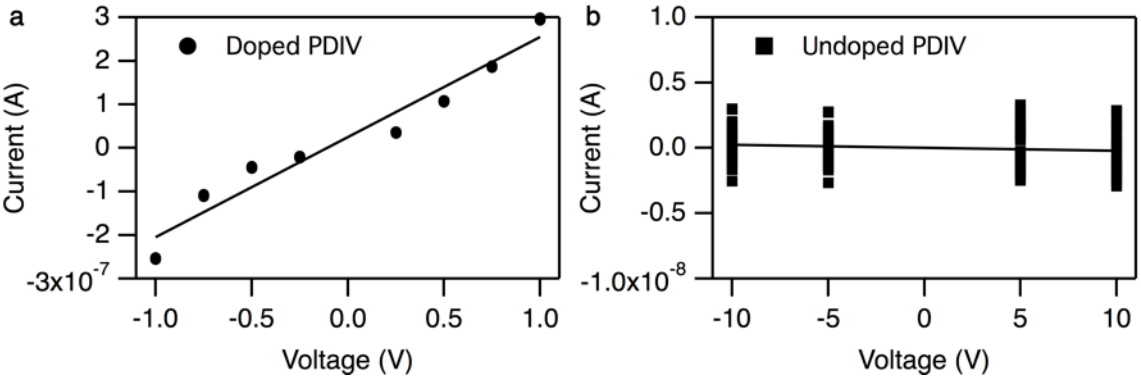

Figure 23: *I-V* curves of (a) doped PDIV and (b) undoped PDIV.

In summary, the polymer PDIV can be doped under ambient conditions to form an electrically conductive persistent radical anion polymer. The polymers prepared in this work and other rylenediimide-vinylene alternating copolymers that could be prepared using our strategy are promising for applications that require materials that are n-doped to

achieve a high carrier concentration under ambient conditions, such as n-type thermoelectric materials.[8, 13, 16, 39] The mixed ionic and electronic conductivity of these polymers are also beneficial for materials that require simultaneous electronic and ionic transport, such as n-type organic field effect transistors for complementary logic circuits[40-41] and mersisters.[42-43]

CHAPTER 3

THERMOELECTRIC PROPERTIES OF PBTDV2/CARBON NANOTUBE BLENDS

3.1 Introduction and Overview

In this chapter, I summarize the thermoelectric properties of blends of the polymer PBTDV2 (see Figure 24 for the structure of PBTDV2) with single-walled carbon nanotubes (SWNTs). The motivation for this work was to determine the effect of SWNT content on the σ and α of conjugated polymers prepared by the DV group and to determine whether the transport was n-type or p-type based on the sign of the α. Blending carbon nanotubes with conjugated polymers is an established strategy for improving the thermoelectric properties conjugated polymer and small molecule semiconductors by increasing their σ.[44-53] Conjugated polymer blends with SWNT with a narrow diameter (~0.7-1.4 nm) typically have superior thermoelectric properties than blends with SWNT with a relatively wider diameter and multi-walled carbon nanotubes due their greater conductivity and Seebeck coefficient.[44, 52] Although SWNTs are intrinsically n-type semiconductors,[54] the position of their E_F relative to the DOS and thus their type of transport (n-type or p-type) is extremely sensitive to factors such as the presence of oxygen gas,[55] ionic additives,[49, 56] conjugated molecular dopants,[46, 57] or amine functional groups in their environment.[58] Blends of conjugated polymer or small molecule semiconductors with SWNTs can therefore be used to prepare n-type or p-type thermoelectric materials.

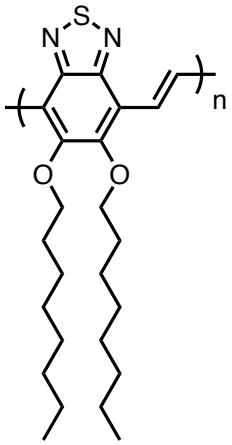

Figure 24: The chemical structure of PBTDV2.

The DV group has previously reported that PBTDV2 is capable of electron transport, having a low-lying LUMO level of -3.45 eV and an electron mobility on the order of 1.3×10^{-3} cm^2 V^{-1} s^{-1}. PBTDV2 is also easily electrochemically oxidized, having a HOMO level of -5.24 eV, suggesting it may be capable of ambipolar transport. Using the sign of the α, we determined that blends containing 10-50% SWNT in PBTDV2, measured in atmosphere, are p-type rather than n-type semiconductors. We also pursued the same strategy for the polymer PDIV to experimentally determine whether its blends with SWNT would exhibit p-type or n-type transport, but found that PDIV was unable to stabilize dispersions of SWNTs and films prepared from blends of PDIV with SWNT were cracked and not electrically conductive across the centimeter length scale. I acknowledge Dr. Timothy Gehan, who synthesized PBTDV2. I also acknowledge Dr. Murat Tonga and Prof. Paul Lahti, who provided and explained the use of the thermoelectric measurement apparatus, which I used consistently in the research projects described in the remaining chapters of this dissertation.

3.2 Preparation and Thermoelectric Properties of PBTDV2/SWNT Blends

SWNTs form bundles through strong inter-tube interactions and are intractable in common solvents. To achieve solution-processable blends of SWNTs, SWNTs can be sonicated in an organic solvent containing a polymer additive. Certain polymers can adhere to the SWNTs and stabilize dispersions of SWNTs in common solvents. Conjugated polymers are thought to interact with SWNT through π- π interactions and stabilized SWNT dispersions by wrapping around the SWNT tubes is organic solvents.[44] To attain dispersions of SWNT stabilized by PBTDV2 with a weight percent of SWNT ranging 10-50%, 5 mg/mL SWNT was mixed with *o*-DCB under pulsed probe sonication for 72 minutes, the amount of 5 mg/mL PBTDV2 in chloroform necessary to obtain the desired weight percentage was immediately added to this, and then the mixture was sonicated for an additional 12 minutes of pulsed probe sonication. Pulses were set to 5 seconds of sonication time followed by 1 second pauses. Flexible films were prepared from these dispersions by dropcasting 0.3 mL of the dispersion onto PTFE tape substrates placed within custom made PTFE wells, and a film of pure PBTDV2 (0% SWNT) was prepared by dropcasting 0.3 mL of 5 mg/mL PBTDV2 in chloroform (see Figure 25). The films were allowed to dry under ambient conditions for 48 h and then under vacuum for 24 h. Since the flexibility and uneven nature of each film precluded the use of profilimetry to measure the film thickness, the thickness was instead calculated (6.9 μm for each film) using the estimated volume of material dropcast (assuming a density of 1 g/cm^3), the measured length (2.7 cm), and the measured width (0.8 cm).

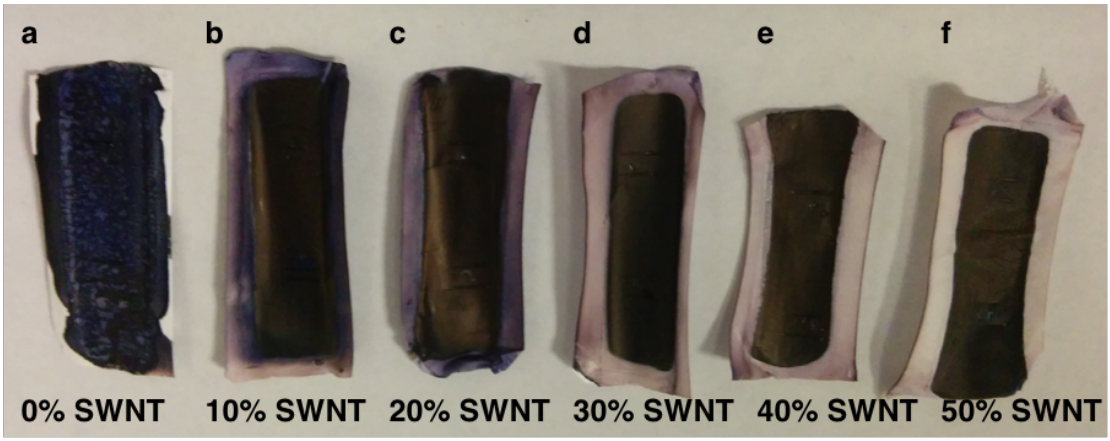

Figure 25: Flexible films of PBTDV2 blended with (a) 0%, (b) 10%, (c) 20%, (d) 30%, (e) 40%, and (f) 50% SWNT.

3.2.1 Thermoelectric Properties of Undoped PBTDV2/SWNT Blends

σ was determined using a 4-probe technique. α was determined by measuring the thermovoltage at a series of applied temperature gradients and determining slope. The details of the apparatus used to measure σ and α are provided in Appendix A. The sample of PBTDV2 with 0% SWNT had visible cracks and did not form a continuous film across the length of the substrate, thus its in-plane conductivity and Seebeck coefficient could not be determined.

The percolation of SWNT through conjugated polymer blends determines the bulk conductivity of the blend, σ, based on the relation: $\sigma = \sigma_{SWNT}|\rho - \rho^*|^t$.[44, 59-60] The fitting coefficient σ_{SWNT} represents the theoretical conductivity of pure SWNT, ρ is the weight fraction of SWNT in the blend, ρ^* is the percolation threshold of SWNT, and t is a critical exponent that describes the dimensionality of the network of SWNT. 2D networks are defined by have a $t = 4/3$, while 3D networks have a $t = 2$. For samples containing 10-50% SWNT in PBTDV2, the best fit of the σ vs ρ trend (see Figure 26a) for t was 1.16,

suggesting the possibility of a 2D network of SWNT driven by a preference for in-plane alignment of SWNT. It is important to note, however, that the empirically fitted t from experimental samples can deviate from its expected value for 2D or 3D networks,[44, 60] and thus the empirical fit of $t = 1.16$ does not rule out the possibility of a 3D network in these samples. The ρ^* and σ_{SWNT} of this fit were 1.61% and 384 S/cm, respectively, which is comparable to the ρ^* and σ_{SWNT} for SWNT blends with P3HT.[44] σ follows the relation $\ln \sigma \propto \rho^{-1/3}$ (see Figure 26b), which is consistent with charge transport limited by tunnel junctions of PBTDV2 matrix between SWNT intertube gaps.[44, 59-60]

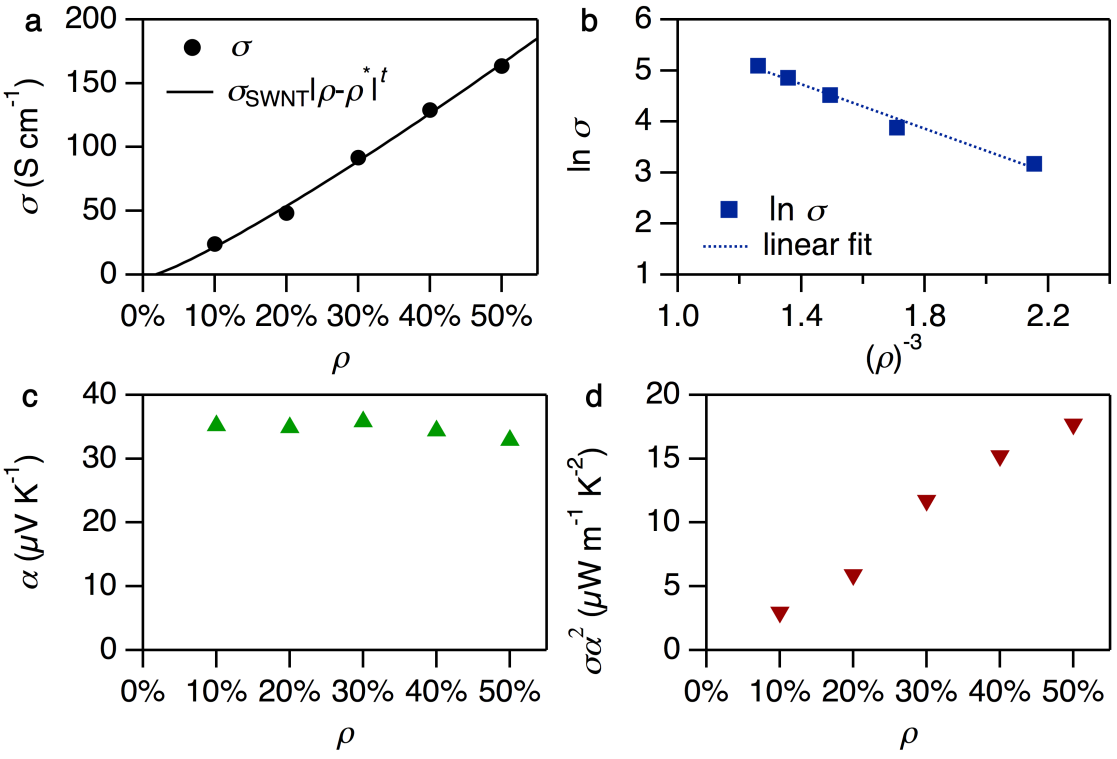

Figure 26: (a) Conductivity of SWNT:PBTDV2 blends as a function of ρ (black circles) and the fit to the model of percolation of SWNT filler in a matrix of PBTDV2 (solid black line), (b) the natural logarithm of conductivity dependence on $\rho^{-1/3}$ (blue squares) and the linear fit of this relation (dashed blue line), (c) the Seebeck coefficient.

The α of the blends of 10-50% SWNT in PBTDV2 was 32.9-35.8 μV K^{-1} (see Figure 26c), with no clear dependence on ρ, which is consistent with the α of SWNT and the α of conjugated polymer SWNT blends where $\rho \gg \rho^*$.[44] The positive sign of α indicates that holes are the charge carrier. Given the consistency of the α and steady increase in σ upon increasing ρ, the thermoelectric power factor increases with increasing ρ (see Figure 26d).

3.2.2 Thermoelectric Properties of Doped 50% SWNT in PBTDV2

Since the charge carrier in each blend in the 10-50% SWNT range was determined to be holes based on the positive α, chemical oxidation was expected to decrease α, increase σ, and potentially improve the thermoelectric power factor. Of all the undoped samples, 50% SWNT had the greatest thermoelectric power factor of 17.7 μW m^{-1} K^{-2}. This sample was doped by chemical oxidation with iodine vapor to determine the effect of doping on its thermoelectric performance (see Figure 27). After measuring the α and σ of the undoped sample, the same sample was doped with iodine vapor by sealing it in a vial containing ~50 mg of iodine crystals for 24 h before measuring α and σ again. α decreased from 32.9 to 24.7 μV K-1, σ increased from 163.4 to 486.6 S cm-1, and the overall power factor increased from 17.7 to 29.6 μW m^{-1} K^{-2}. Although the thermoelectric power factor improved, it is still significantly lower than the highest thermoelectric power factors reported for SWNT blends with conjugated polymers, such as the recently reported p-type and n-type power factors of ~700 μW m^{-1} K^{-2} for blends of SWNT with the conjugated polymer poly[(9,9-di-n-dodecyl-2,7-fluorendiyl-dimethine)-(1,4-phenylene-dinitrilomethine)].[61]

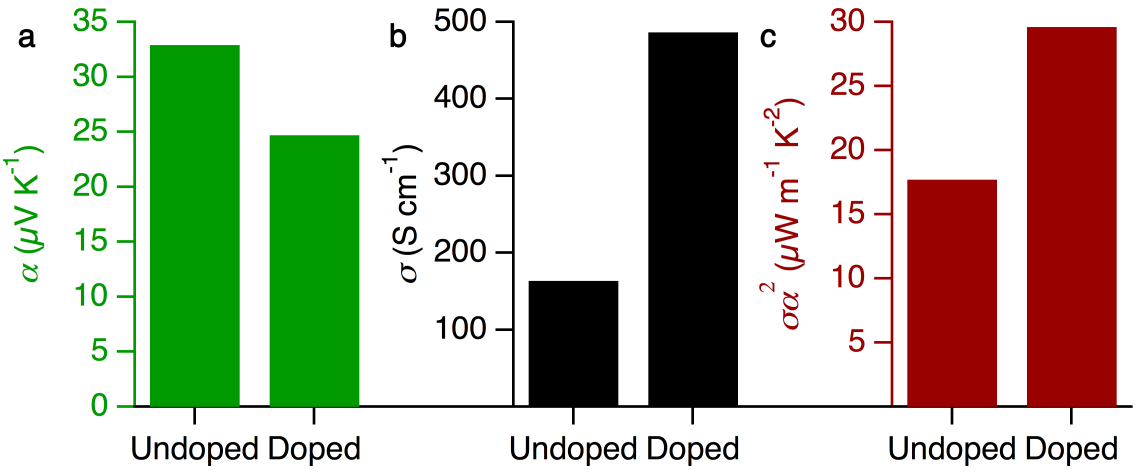

Figure 27: The (a) α, (b) σ, and (c) power factor of 50% SWNT in PBTDV2 before and after doping with iodine vapor.

3.2.3 Conclusion of Thermoelectric Properties PBTDV2:SWNT Blends

Undoped blends of SWNT with PBTDV2 were found to be p-type thermoelectric materials with α and σ magnitudes and SWNT concentration dependencies that are remarkably similar to those of SWNT blends with P3HT from the literature. The power factor of 50% SWNT in PBTDV2 improved upon doping with iodine vapor, but is still lower than the highest power factors obtained for blends of SWNT with conjugated polymers. Since none of the blends of SWNT with PBTDV2 prepared in this work were inherently n-type thermoelectric materials and since PDIV was unable to disperse SWNT to form solution-processable, homogeneous blends that could be studied, I decided to shift the focus my research to understanding the impact of doping on the thermoelectric properties, as described in the remaining chapters of this dissertation.

CHAPTER 4

SPATIAL HETEROGENEITY OF DOPANTS IMPACTS THE THERMOELECTRIC CHARGE TRANSPORT PROPERTIES

4.1 Overview

In this chapter,† I describe our measurements and modeling of the thermoelectric properties of P3HT and PDPP4T doped with iodine vapor as they spontaneously dedope.[62] This work was motivated by the recent charge transport model reported by Kang and Snyder, which requires σ and α across many orders of magnitude of σ for fitting. The idea of spontaneously doping polymer films was inspired by the findings reported in Murat Tonga's Ph.D. dissertation, that films of blends of conjugated polymers with carbon nanotubes doped with iodine vapor spontaneously dedope, resulting in a decrease in their *n*. I decided that this phenomenon could be exploited to achieve the desired range of σ and α by taking automated measurements as the sample spontaneously de-dopes.

I acknowledge Dr. Feng Liu and Prof. Thomas P. Russell for synthesizing PDPP4T, Dr. Ljiljana Korugic-Karasz for discussions on charge transport in semicrystalline polymers, Stephen Dongming Kang and Dr. G. Jeffrey Snyder for providing their transport model fitting MatLAB code, Dr. Lawrence Renna for his insights and modifications to the code, and Dr. Peijian Wang and Prof. Mike Barnes for characterizing the KPFM and PL microscopy. I gratefully acknowledge Meenakshi

† This chapter is reproduced with slight modifications from Ref. 62, our manuscript in preparation, Boyle, C. J.; Upadhyaya, M.; Wang, P.; Renna, L. A.; Korugic-Karasz, L.; Barnes, M. D.; Aksamija, Z.; Venkataraman, D., Spatial Heterogeneity of Dopants Impacts the Thermoelectric Charge Transport Properties.

Upadhyaya and Zlatan Aksamija, who conceived and implemented the charge transport simulations and DOS calculations which were fundamental to our understanding that the spatial distribution of dopants is responsible for modifying the DOS and thermoelectric properties.

4.2 Introduction

Semiconducting properties of conjugated polymers enable the development of electronic applications such as organic light-emitting diodes,[63-65] organic photovoltaics,[66-68] and organic thermoelectrics.[69-71] These applications are now poised to restructure our sustainable energy technologies portfolio as they offer distinct advantages over existing technologies. Organic electronic devices are lightweight, flexible, and are fabricated using solution-based processing methods. Charge transport in conjugated polymers is central to their performance. Therefore, understanding factors that affect the charge transport in these materials is necessary to improve their performance. A significant challenge to improving our understanding of this charge transport is that, unlike inorganic semiconductors, conjugated polymers do not adopt long-range ordered crystalline structures.

In charge transport, conductivity, σ, is dictated by the expression: $\sigma = nq\mu$, where n is nunumber of charge carriers, q is the carrier charge, and μ is the charge carrier mobility. Determining the charge carrier mobility and its dependence on temperature, field, or carrier concentration in conjugated polymers has led to considerable progress in understanding their charge transport.[72-78] However, this methodology becomes complicated by the difficulty in determining the carrier concentration with certainty and discrepancies in the reported mobilities for a given material.[79-81] The discrepencies in the

reported mobilities arise from differences in device architecture and the measurement technique. Furthermore, measured mobilities are the direct result of a carriers' drift velocity, v_d, at an applied field, $\mathbf{E}$, given by the realtion: $v_d = \mu\mathbf{E}$. Thus, mobility measurements cannot be used to determine the energy carried per unit carrier or information about the density of states (DOS) that are model and calculation independent.

An effective method to overcome these challenges is to measure both the conductivity and the Seebeck coefficient, α, across a broad range of carrier concentrations. The Seebeck coefficient is the voltage response to an applied temperature gradient, given by the equation: $\alpha = \frac{\Delta V}{\Delta T}$. This methodology takes advantage of the fact that α can be expressed, according to Fritzsche's general equation,[2] as $\alpha = \left(\frac{k_B}{q}\right) \int \left(\frac{E-E_F}{kT}\right) \frac{\sigma(E)}{\sigma} dE$ and σ as $\sigma = \int \sigma(E)\, dE = q \int g(E)\mu(E)f(E)[1 - f(E)]\, dE$. In these equations, E_F is the chemical potential and a relative indicator of the level of doping, $g(E)$ is the DOS, $\mu(E)$ is the charge carrier mobility, and $f(E)$ is the Fermi distribution. This approach is more widely applicable than the simpler Mott formula[82] $\alpha = -\left(\frac{\pi^2}{3}\right)\left(\frac{k^2 T}{q}\right)\frac{\partial}{\partial E}\ln[\sigma(E)]|_{E=E_F}$. Since these expressions are valid (neglecting correlation effects) across all doping levels regardless of the conduction mechanism or the semiconductor's crystalline, semi-crystalline, or amorphous nature, they support numerous mechanisms of conduction in disordered semiconductors,[83-85] including hopping models based the Miller-Abrahams[86] and Marcus[87] jump rates, that add to our physical explanation of charge transport in conjugated polymers and provide structural design criteria for improving their performance.

Generally, both α and σ depend on the carrier concentration $n = \int g(E)f(E)dE$ via the Fermi level but they have opposite trends—increasing n fills more states and boosts σ but decreases α. Thus, there is a narrow range of doping that optimizes the thermoelectric power factor, $\alpha^2\sigma$, which typically occurs when 10-20% of the states are occupied by a charge carrier. Thus, the shape of the DOS has an enormous impact on the scale and the trend of α which is not yet fully understood. Snyder and Kang's recent charge transport model also employs these expressions, substituting for the term $g(E)\mu(E)$ the empirical fitting transport function $\sigma_E(E,T) = \sigma_{E_0}(T)\left(\frac{E-E_t}{kT}\right)^s$ which successfully fits a diverse array of conjugated polymers and small molecules using a transport coefficient σ_{E_0}, comparable to the mobility of the semiconductor, and a transport parameter s.[88] Snyder and Kang state that the s parameter "could be understood as a different 'type' of charge transport" and they speculated that a "search for cases with s = 1 could lead to discovery of high-σ_{E_0} polymers". Characterizing both α and σ across a broad range of doping levels enables a more complete explanation of charge transport that is not possible from measurements of σ or mobility alone. Thus far, the factors that determine the transport parameter, s, in the Synder-Kang model are unclear.

We obtained α and σ across a broad range of doping levels by making in situ measurements of iodine doped conjugated polymers as they spontaneously de-dope, capturing the trend of α and σ using a single sample and without modulation doping. We simulated carrier transport using a modified Gaussian disorder model and the Pauli Master equation to explain how the shape of the DOS impacts the α and σ trend. SPC

mapping by KPFM verifies that differences in energetic disorder are related to differences in dopant counterion distribution throughout the sample.

It is well-established that the carrier concentration – *how much* a semiconductor is doped – is a key parameter in determining a semiconductor's thermoelectric performance, and even slight deviations from the optimal carrier concentration can cause a catastrophic loss in thermoelectric performance. Herein, we demonstrate that *the way* the semiconductor has been doped is fundamentally important to its thermoelectric performance across all carrier concentrations. We show that the distribution of the dopants in the conjugated polymer has a profound impact on the shape of the α vs. σ curve. We observe that a clustering of dopants in the polymer modifes the shape of the DOS and alters the trend of α vs. σ.

4.3 Results and Discussion

Measuring the σ and α over a wide range of values requires a large range of doping densities for a particular semiconductor. Chemical[3, 15-16, 89-95] or electrochemical[5] oxidation have been used to prepare organic semiconductors at many different doping densities for such characterization, but this requires the preparation of many different samples and the assumption that each sample has a nearly identical morphology. Modulation doping using field-effect transistors[96-97] has been used to measure the σ and α at many different, finely controlled doping densities, but the dipole distribution within the dielectric layer can influence the DOS by shifting shallow energy states to a deeper level,[84, 98] and thus impacts the α vs. σ trend in a way that traditional, chemically doped thermoelectric devices would not be affected. Recently, modulation doping using

electrochemical field-effect transistors has also been used to control the doping density of thermoelectric materials.[99-100] The manner in which ion infiltration into the conjugated polymer during and after gating the electrochemical field-effect transistor impacts the shape of the DOS currently remains unclear. The methodology we report herein uses spontaneous dedoping of chemically doped conjugated polymers as a rapid and convenient way to capture α vs. σ across four orders of magnitude of σ, using an individual sample, and without gating across a dielectric or electrolytic layer.

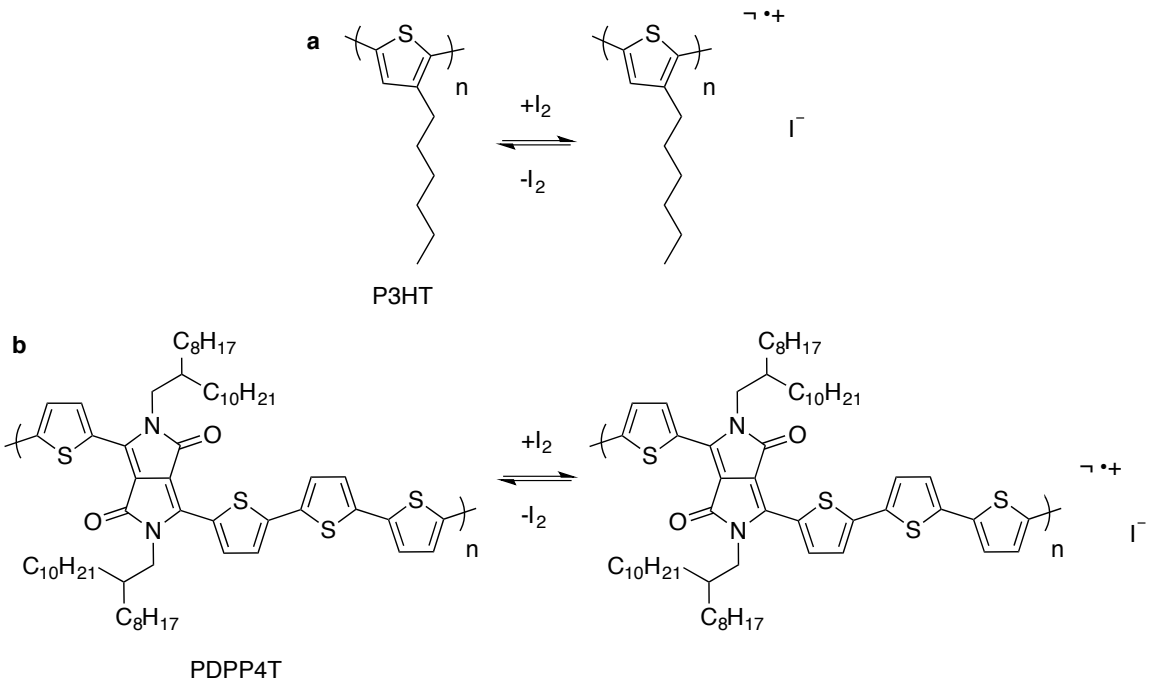

Figure 28: (a) P3HT and (b) PDPP4T are chemically doped in the presence of iodine vapor, but are unstable and gradually dedope in the absence of iodine vapor.

Doping organic semiconductors with iodine vapor[48, 101-106] is a well-established strategy to increase the p-type carrier (hole) concentration, resulting in an increased σ and decreased α. Samples doped in this manner can spontaneously de-dope over time, resulting in a gradual decrease in σ and increase in α from their values in the initial

doped state. We exploit this de-doping process to measure α as a function of σ over a four orders of magnitude σ window. We doped films of poly(3-hexylthiophene) (P3HT) and poly[2,5-bis(2-octyldodecyl)pyrrolo[3,4-c]pyrrole-1,4(2H,5H)-dione-3,6-diyl)-alt-(2,2';5',2'';5'',2''-quaterthiophen-5,5'''-diyl)] (PDPP4T) with iodine vapor (see Figure 28) to obtain highly doped p-type polymer films. Doping by iodine vapor was performed by exposing the polymer films to iodine vapor (see the Experimental Section in Appendix A for details) for 2 h at either 25 °C or 75 °C. We then measured, *in situ*, α and σ as the films spontaneously de-doped. In each sample, α increased and σ decreased over time as the film de-doped (see Figure 29), as is expected for organic semiconductors with decreasing carrier concentration. Notably, α increased at a decreasing rate for each P3HT sample while α increased at an increasing rate for each PDPP4T sample. α and σ both depend on the free carrier concentration, but this concentration is difficult to determine with certainty because a percentage of carriers are bipolarons, which have no electron paramagnetic resonance spectroscopy signal.[107] Thus, plotting the α vs. σ on the log-log scale is preferable (see Figure 30). The shape of the α vs. σ curve on the log-log plot indicates the nature of charge transport of the material. For instance, in Kang and Snyder's model, a flatter and more gradual curve is indicative of a transport parameter of $s = 3$, while a curve maintaining a greater α until a sudden, sharp drop-off at high σ is consistent with $s = 1$. Our simulations, vide infra, show that a flatter (i.e. $s = 3$) α vs. σ curve indicates a great energetic disorder and an exponential DOS, while a sharper α vs. σ curve indicates a narrow DOS.

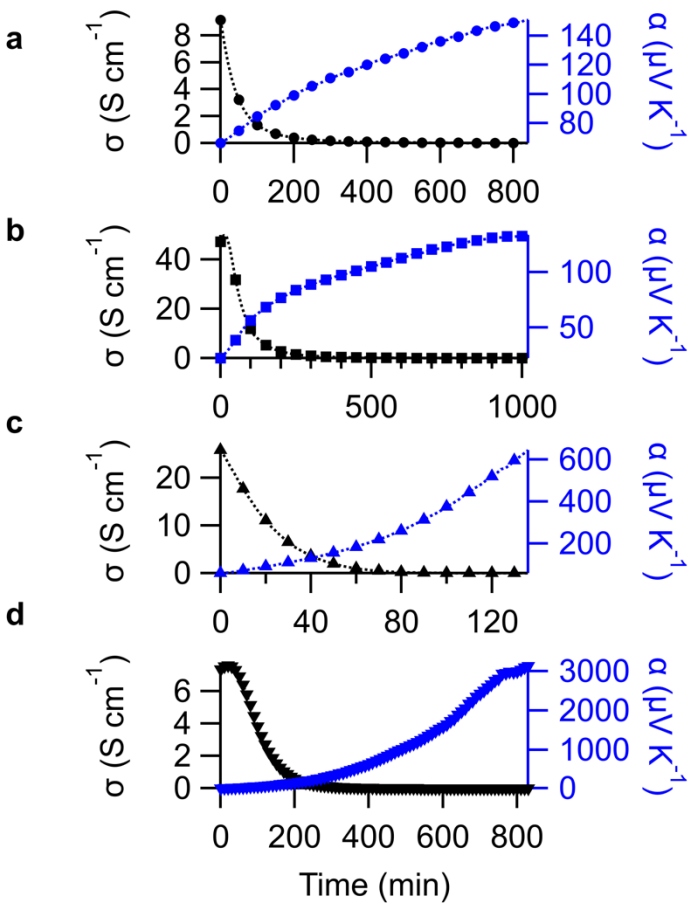

Figure 29: Conductivity (black, left axis) and Seebeck coefficient (blue, right axis) for (a) P3HT doped at 25 °C, (b) P3HT doped at 75 °C, (c) PDPP4T doped at 25 °C, and (d) PDPP4T doped at 75 °C. One of every five data points collected is plotted along a dashed line as a visual guide.

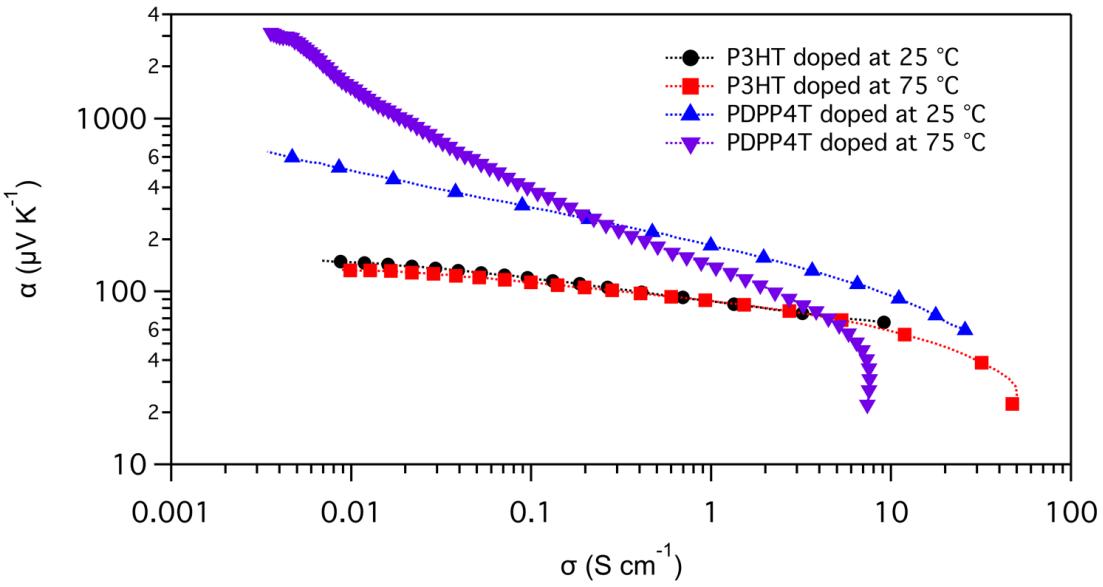

Figure 30: log-log plot of Seebeck coefficient vs. conductivity for P3HT doped at 25 °C (black circles), P3HT doped at 75 °C (red squares), PDPP4T doped at 25 °C (blue up triangles), and PDPP4T doped at 75 °C (purple down triangles). One of every five data points collected is plotted along with a dashed line as a visual guide. Vertical error bars representing the standard error for the thermovoltage sampling for α and horizontal error bars representing the root mean squared error for the *I-V* curve for σ for each marker would have the same size scale as the marker size, and are thus omitted for clarity.

4.3.1 Gaussian Disorder Model of σ and α

We calculated α and σ by numerically solving the Pauli master equation (PME) that describes phonon-assisted carrier hopping between localized sites (see the Experimental Section in Appendix A for modeling details) whose energies were sampled from the carrier DOS. We obtained α and σ at various carrier densities by varying the chemical potential E_F further and closer to the center of the energy distribution, analogous to doping. Previous studies have used a Gaussian distribution to describe the DOS, where the width of the DOS accounts for the degree of energetic disorder in the structure.[108-111] However, we find that in such a model, varying the energetic or positional

disorder simply shifts the α vs. σ on the log-log plot, with minimal difference in the slope and cannot fully account for the significant difference in the slope of the α vs. σ plots between the P3HT and PDPP4T plots. The Coulombic interaction between the ionized dopant molecules and the localized carriers resulting in the formation of deep trap states, and the physical distribution of dopant molecules within the sample or the size of the dopant clusters both cause further broadening of the DOS. We calculate the DOS resulting from doping concentration N_d in clusters having size C_s, according to Equation 3 in the Experimental Section of Appendix, and find that doping and clustering result in a heavy-tailed, exponential distribution (see Figure 31a).[112] We conclude that it is this 'change in shape' of the DOS that instigates the change in slope in the α vs. σ plot. This is clearly seen in Figure 31b, where we compare the α vs. σ plot for a purely Gaussian and an exponential DOS, showing that the exponential DOS results in a much flatter α vs. σ curve. This can be understood from the Mott formula, expanded[113] as $\alpha \propto \frac{d \ln[g(E)]}{dE} + g \frac{d[\mu(E)]}{dn}$: when the $\mu(E)$ is only weakly dependent on carrier concentration, an exponential DOS leads to a constant α independent of doping or σ, but inversely proportional to the energetic disorder that dictates the width of the DOS.

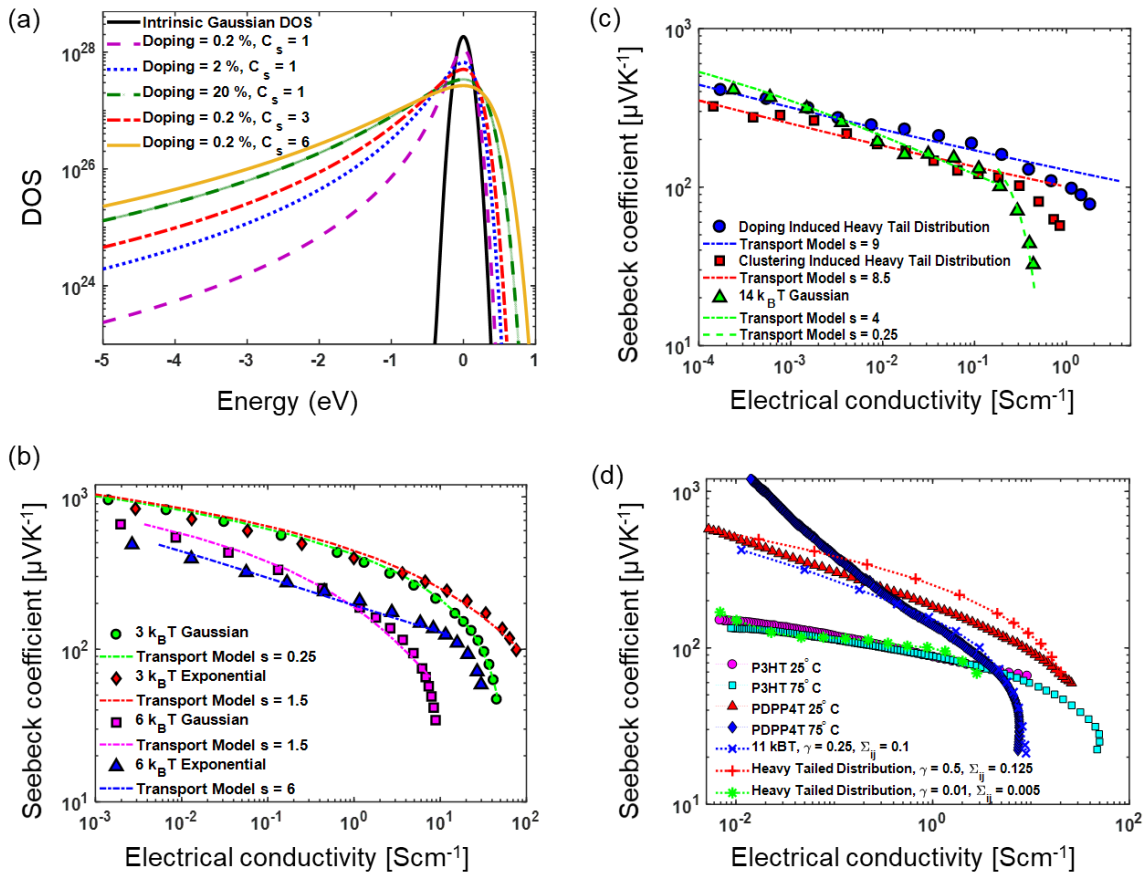

Figure 31: The effect of doping and clustering on the DOS distribution. (Intrinsic Gaussian width = 3 kT) The charge carriers interact Coulombically with the ionized dopants creating additional deep traps and effectively broadening the DOS. Log-log plot of Seebeck coefficient vs. conductivity showing the change in slope due to: (b) Gaussian and exponential DOS, (c) doping and clustering induced effective broadening and deep tail of the DOS. The doping induced distribution is computed with $N_d = 2\%$ and $C_s = 1$, and the clustering induced distribution with $N_d = 0.2\%$ and $C_s = 3$. (d) Comparison of our model to experimental data from Fig. 30. ($N_d = 0.1$ % and $C_s = 1$ for red dashed line with symbol, $N_d = 0.02$ % and $C_s = 9$ for green dashed line with symbol).

Further, Figure 31c compares the effect of a purely Gaussian DOS distribution vs. an exponential DOS distribution computed with several values of N_d and C_s. We compare our results to Snyder and Kang's charge transport model[88] and find that a Gaussian distribution results in significantly lower transport parameter $s \leq 1.5$ compared to the exponential case which has $s \geq 1.5$, and this difference increases further with increasing

width of the energetic disorder. However, at high energetic disorder in the presence of a heavy tail the curve cannot be fit by transport parameter values of $s = 1$ or $s = 3$ (see Figure 31c) indicating the limitations of a band model in predicting transport in highly disordered systems. Comparing our model to experimental data from Figure 30 we find that PDPP4T doped at 75 °C is most closely fit with α vs. σ computed from a purely Gaussian distribution with a width of 11 kT, whereas PDPP4T doped at 25 °C and P3HT is best fit with an exponential DOS that gives us the required change in slope. (see Figure 31d).

4.3.2 Kelvin Probe Force Microscopy and Photoluminescence of iodine doped clusters

To probe the dopant distribution in the conjugated polymer films, we use KPFM, which exploits the capacitive interactions between a metal-coated probe (typically platinum) and the sample. This interaction is associated with the work function difference between the probe and the sample, manifested as a SPC.[114] Since chemical doping of the conjugated polymer by iodine vapor alters the polymer's work function and thus the SPC, KPFM can track and map the changes that occur upon doping along the film's surface. We mapped the SPC of films of P3HT and PDPP4T doped at 25 °C and 75 °C see Figure 32, inset). In the SPC maps, we observed the presence of dense regions in the polymer films that had a different SPC than the surrounding sections. Photoluminescence microscopy imaging (see Figure 33) of a similar P3HT film doped at 25 °C displays dense regions of dark P3HT, consistent with chemically oxidized P3HT,[115] with similar cross-sectional areas surrounded by brighter-emitting P3HT. Therefore, we inferred that

the dense regions in the SPC map corresponds to densely doped states on the film's surface surrounded by less densely doped P3HT.

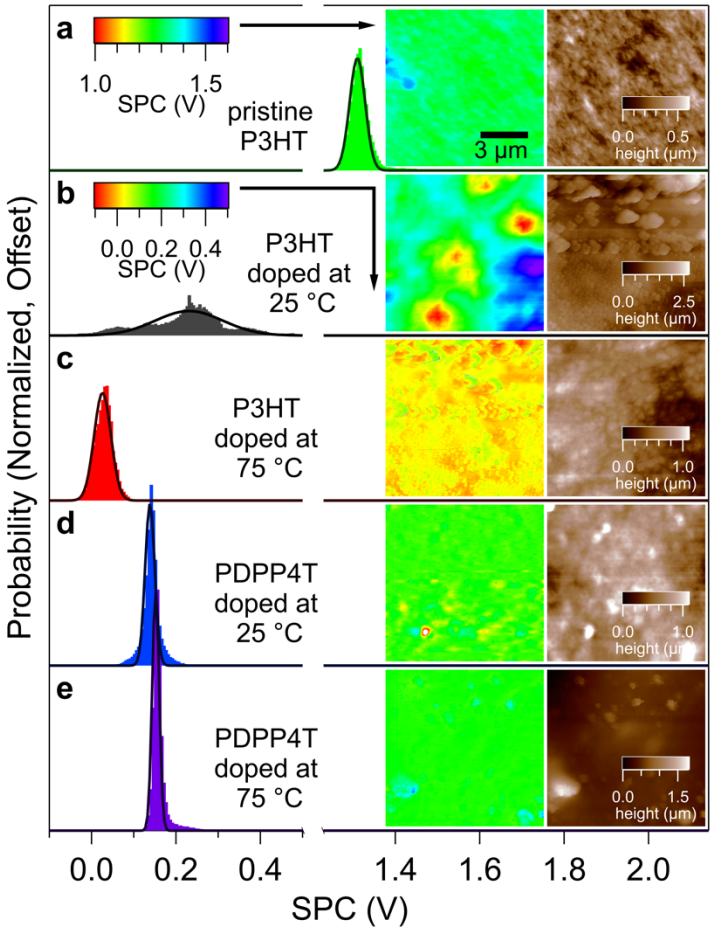

Figure 32: A histogram of measured SPC and its Gaussian fit, with the height map and SPC map inset, of (a) pristine P3HT, (b) P3HT doped at 25 °C, (c) P3HT doped at 75 °C, (d) PDPP4T doped at 25 °C, and (e) PDPP4T doped at 75 °C.

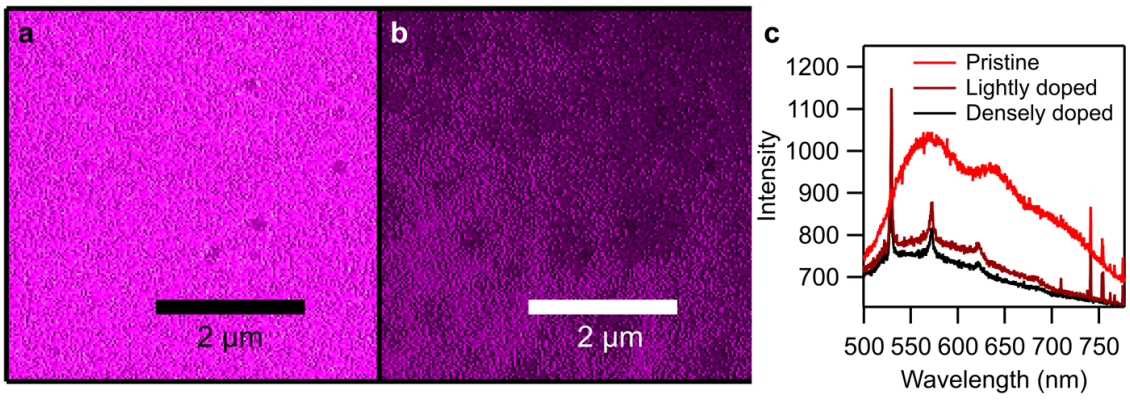

Figure 33: PL images of (a) a pristine P3HT film indicating intense, uniform photoluminescence, (b) an iodine doped P3HT film indicating quenched, non-uniform photoluminescence, and (c) the PL emission spectra of the prisinte P3HT (red), a lightly doped patch from the iodine doped P3HT (maroon), and a densely doped patch of the iodine doped P3HT (black). Exposure time: 0.2 s.

We then determined the homogeneity of the distribution of iodine-doped states within the film using the width of the distribution of SPCs. P3HT films doped at 25 °C displayed a remarkably wide distribution of SPCs and regions of densely doped states with cross-sectional areas on the order of 1 μm^2, indicating the distribution of iodine-doped states is heterogeneous, while pristine P3HT has a narrow distribution of SPCs (see Figure 32). The appearance of an exponential tail to this SPC distribution is consistent with the exponential DOS distribution we modeled to fit the α vs. σ curve for P3HT doped at 25 °C. P3HT films doped at 75 °C showed a marginally narrower distribution of SPCs, suggesting that P3HT films doped at 75 °C exhibit a slightly more homogeneous distribution of iodine-doped states compared to P3HT doped at 25 °C. PDPP4T doped at 25 °C displayed a significantly narrower distribution of SPCs than either P3HT sample, and PDPP4T doped at 75 °C had yet an even narrower distribution of SPCs. The trend of SPC distributions for each sample is consistent with the DOS distributions we modeled, confirming that the α vs. σ curve can be fit to an appropriate

DOS by solving the Pauli master equation. PDPP4T is doped with a more homogeneous distribution of iodine-doped states than P3HT and homogeneity of iodine-doped states increases with increasing doping temperature.

We tracked the SPC distribution of P3HT doped at 25 °C over time as the sample spontaneously dedoped to determine the effect of de-doping on the dopant distribution homogeneity (see Figure 34a). The SPC distributions recorded at each time were fit to a Gaussian distribution (Figure 34b) so that the dopant homogeneity can be described in terms of the mean (Figure 34c) and width of this distribution (Figure 34d). The width of the SPC distribution decreases over time, indicating the dopant distribution becomes more homogeneous as the sample de-dopes and the concentration of dopant counterions in the film decreases. The mean of the Gaussian fit of the SPC distribution becomes more positive over time, consistent with the increase in E_F of P3HT upon de-doping.

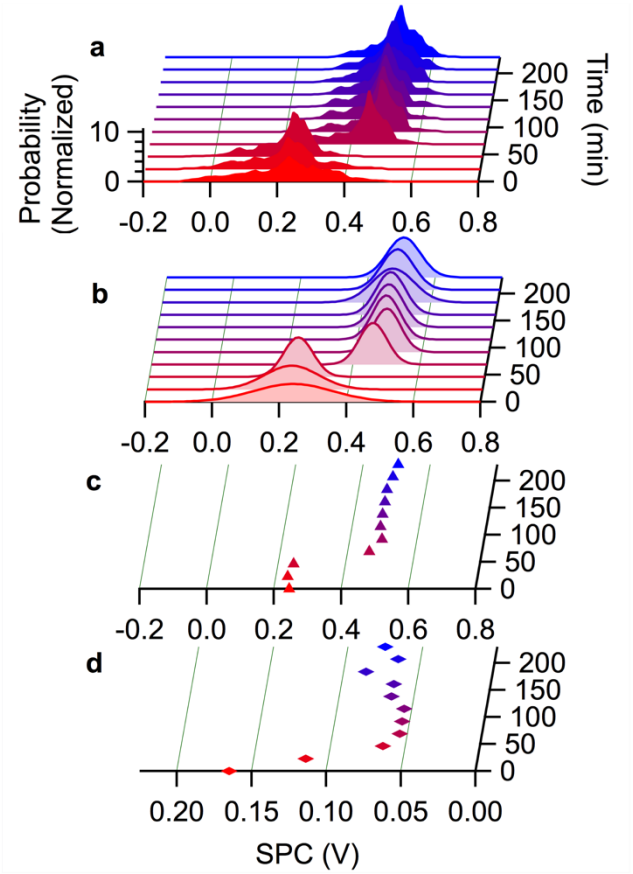

Figure 34: (a) Histograms of the SPC distribution, (b) Gaussian fit to each histogram, and the (c) mean and (d) width of the Gaussian fits of a film of P3HT initially doped at 25 °C as it spontaneously de-dopes.

4.4 Conclusion

Our studies establish that the shape of the α vs. σ curve depends on the distribution of the dopants in the conjugated polymer. The dopant distribution affects the energetic disorder, which in turn affects the charge transport properties. Our studies suggest that tuning the energetic disorder by controlling the dopant counterion distribution within the doped film and the dielectric constant of the organic semiconductor can lead to substantial improvements in the thermoelectric performance of organic semiconductors. We predict that polymers doped with a uniform dopant

distribution will lead to narrow energetic disorder and thus enhanced thermoelectric properties.

CHAPTER 5

ELECTROCHEMICAL CONTROL OF THE THERMOELECTRIC PROPERTIES OF PEDOT TOSYLATE

5.1 Introduction and Overview

Poly(3,4-ethylenedioxythiophene) tosylate (PEDOT:Tos) is a conducting polymer that can be prepared by chemical oxidation of 3,4-ethylenedioxythiophene (EDOT) using an oxidant, such as ferric tosylate, and a weak base (see Figure 35). PEDOT has thermoelectric charge transport characteristics that are unique to other conjugated polymers, having a transport parameter $s = 1$ according to Kang and Snyder's model,[88] and currently has the highest reported thermoelectric power factor (1,270 $\mu W\ m^{-1}\ K^{-2}$) and ZT (0.42) of any organic thermoelectric material.[3-5] The previous chapter of this dissertation describes in detail how the transport parameter of $s = 1$ can actually be explained by a homogeneous distribution of dopants throughout the conducting polymer film and a narrow DOS, and how these properties can be obtained in polymers other than PEDOT:Tos. The motivation for the research described in the current chapter was to determine how the unique charge transport properties of PEDOT:Tos depend on the spatial distribution of dopants throughout the film.

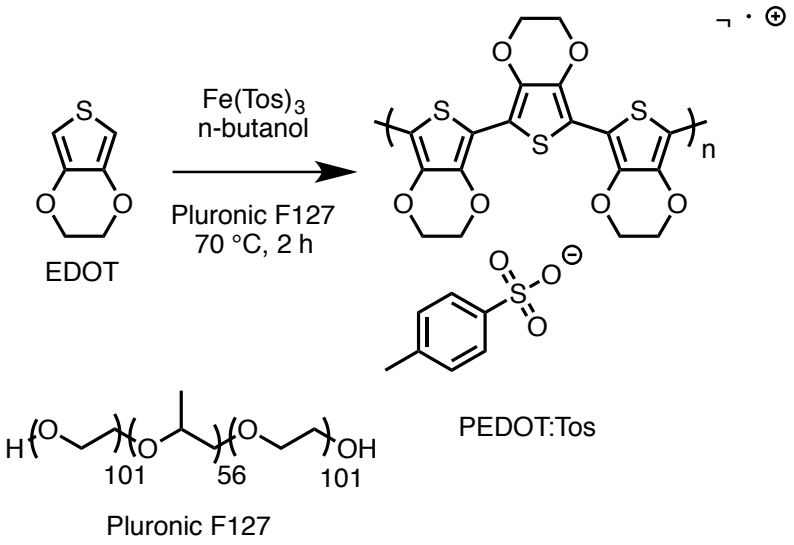

Figure 35: Oxididative polymerization conditions used for the SCP of PEDOT:Tos in this work. Pluronic F127 is added as a weak base that coordinates with Fe^{III} ions.

Conducting films of PEDOT:Tos were prepared, their σ and α were measured, and the extent of doping was controlled to a limited extent by electrochemical oxidation and reduction, but the range of σ and α obtained was not broad enough to enable confident fitting of the of the α vs. σ trend. This chapter provides a record of how PEDOT:Tos was prepared by solution casting polymerization (SCP), how its σ and α were controlled electrochemically, and offers suggestions for possible improvements to controlling the σ and α for future projects dealing with PEDOT:Tos for thermoelectric or other applications.

I gratefully acknowledge Julia Lenef and Haote Li for their assistance with this project. The preparation of PEDOT:Tos films, electrochemical oxidation and reduction of these films, and the measurement of σ and α was a collaborative effort shared by the three of us.

5.2 Preparation of PEDOT:Tos Films by SCP

PEDOT is insoluble in common solvents, and it is therefore necessary to prepare stable dispersions of PEDOT particles in a solvent or to prepare PEDOT by in situ polymerization directly into the desired film or device architecture. Heterophase polymerization leading to stable PEDOT dispersions have been studied extensively, most notably the oxidative dispersion polymerization of EDOT in the presence of poly(styrenesulfonate) (PSS) for the preparation of aqueous dispersions of PEDOT:PSS.[116] PEDOT:PSS in water is expansively used in organic electronics research and applications including electrochemical transistors,[117] the hole transporting layer in organic light emitting diodes and photovoltaics,[118-119] and as a thermoelectric material.[5, 45, 90] In situ methods for the direct preparation of PEDOT films or devices, including electrochemical polymerization,[120] vapor phase polymerization,[121] and SCP,[5, 122] are also useful. Oxidative SCP of PEDOT, a method by which a reactive solution of EDOT, oxidant, and a weak base (see Figure 35 for the oxidative SCP conditions used in this work) are directly cast onto the desired substrate and polymerized by increasing the temperature of the film, is the technique that has been used to prepare PEDOT:Tos with the greatest reported power factor for organic thermoelectric materials and to prepare PEDOT:Tos described by Kang and Snyder as having a transport parameter of $s = 1$.[3, 5, 88] Each technique results in PEDOT that is already chemically doped, since the PEDOT is formed in the presence of an oxidant and PEDOT itself has a lower redox potential than EDOT. PEDOT remains doped indefinitely under ambient conditions due its low redox potential.

We chose to use SCP to prepare PEDOT:Tos samples for this research in order to begin this project with samples resembling those reported to have $s = 1$. The experimental procedures we used for SCP are described in the Experimental Section in Appendix A. All polymerizations were carried using *n*-butanol as the solvent, ferric tosylate as the oxidant, and at a polymerization temperature of 70 °C. The oxidative solution was always prepared using an ethoxylated additive:oxidant:solvent weight ratio of 1:2:3 whenever an ethoxylated additive was used, and an oxidant:solvent weight ratio of 2:3 otherwise. The molar ratio of the oxidant, ferric tosylate, to monomer, EDOT, was 1.5:1 unless otherwise stated. We initially tested the impact of the impact of ethoxylated additive and the impact of oxidant (ferric toslyate) to monomer (EDOT) ratio on the σ and α of the PEDOT:Tos. The purpose of these tests was to find conditions for SCP that result in the consistent, repeatable formation of PEDOT:Tos films with similar σ and α, not to try to optimize σ, α, or the thermoelectric power factor. Next, we electrochemically controlled the extent of doping in the PEDOT:Tos in order to prepare PEDOT:Tos with a range of σ and α. Electrochemical control of the PEDOT:Tos carrier concentration resulted in a range of σ spanning ~1 order of magnitude, which is insufficient to model the charge transport properties.

5.2.2 Effect of Weak Base Additive Used in SCP on the Conductivity and Seebeck Coefficient of PEDOT:Tos

The conductivity of PEDOT:Tos prepared by SCP is sensitive to the polymerization temperature, solvent, oxidant concentration, monomer concentration, and the type and concentration of weak base additive or additives.[3, 122] Aromatic nitrogen-containing weak bases, such as pyridine and imidazole, are reported to aid in the

polymerization of high conductivity PEDOT:Tos by inhibiting the oxidant and slowing the rate of polymerization, allowing more time for crystallization of ordered domains of PEDOT. Ethoxylated additives have a similar effect and are also effective for preparing films of PEDOT:Tos with a high conductivity, whether they are used alone or in combination with pyridine or imidazole.

In our initial screening of additives, we prepared PEDOT:Tos using a combination of imidazole (0.5 molar equivalents with respect to oxidant) and Pluronic F127 (see Figure 35 for the chemical structure of Pluronic F127) as the weak base yielding a film that was inconveniently thin (40 nm) for use in our centimeter length-scale in-plane apparatus, and had a σ of 10 S cm^{-1} and an α of 12.0 μV K^{-1}. A film prepared using only imidazole (0.5 molar equivalents with respect to oxidant) and no ethoxylated additive was also thinner than desired (200 nm), and had a σ of 469 S cm^{-1} and an α of 19.7 μV K^{-1}. Although the conductivity of this film was promising, thicker films (approaching the μm scale) are necessary to enable reliable in-plane measurements of α across our centimeter scale apparatus. Since a reasonably high G ($G \geq \sim 10^{-6}$ S, as a general rule)[52] is needed for our nanovoltmeter to draw sufficient current to measure the thermovoltage, and decreasing the extent of doping and thus σ is ultimately necessary to characterize the charge transport at low doping levels, increasing the film thickness t is beneficial obtaining data at lower σ ($G \propto \sigma t$). The film prepared using only the ethoxylated additive Pluronic F127, with no imidazole, was 470 nm thick, with a σ of 316 S cm^{-1} and an α of 15.8 μV K^{-1}. After this initial screening, we shifted our focus to SCP conditions using only ethoxylated additives and avoided using imidazole.

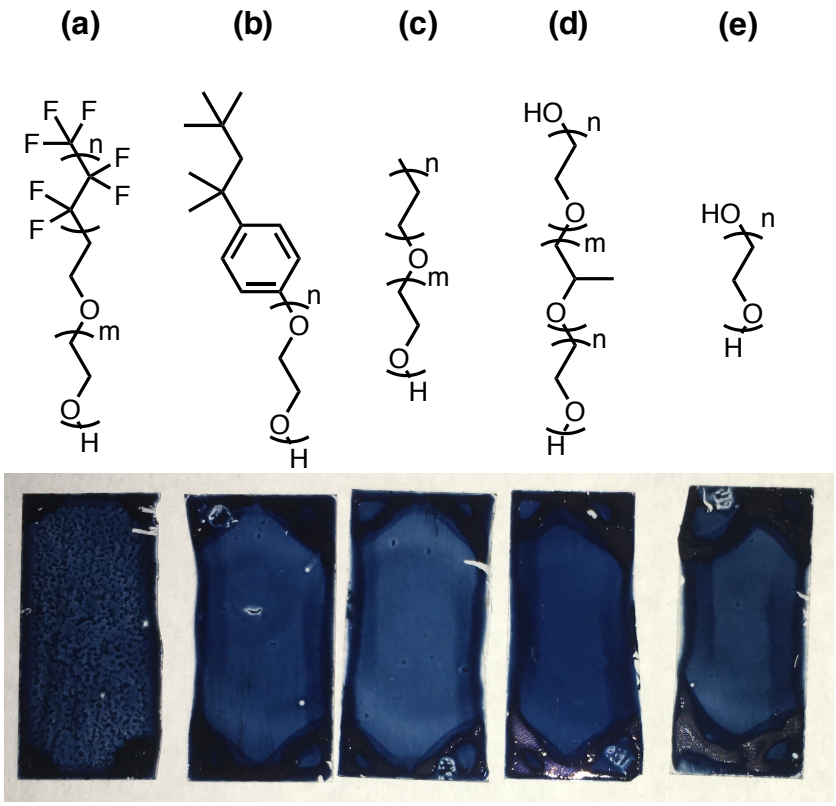

Figure 36: Chemical structure of (top) and image of film prepared using (bottom) the ethoxylated additives (a) Capstone FS-30 (n or m are not provided by the chemical vendor), (b) Triton X-45 (n ≈ 5), (c) Tomadol 91-8 (n ≈ 6, m ≈ 8), (d) Pluronic P85 (n = 26, m = 40), and (e) PEG 600 (n = 14).

Before continuing with Pluronic F127 as the ethoxylated additive, we also prepared PEDOT:Tos used other ethoxylated additives – Capstone FS-30, Triton X-45, Tomadol 91-8, Pluronic P85, and PEG 600 (see Figure 36) – under otherwise identical conditions to measure G and α (see Figure 37). Each film had a very similar α, 15.1-17.3 $\mu V\ K^{-1}$, regardless of the ethoxylated additive used. Decreases in G appeared to be consistent with decreases in film quality/smoothness, as is visually apparent from the nonuniform surface of the films prepared using either Capstone FS-30 (see Figure 36a) or PEG 600 (see Figure 36e).

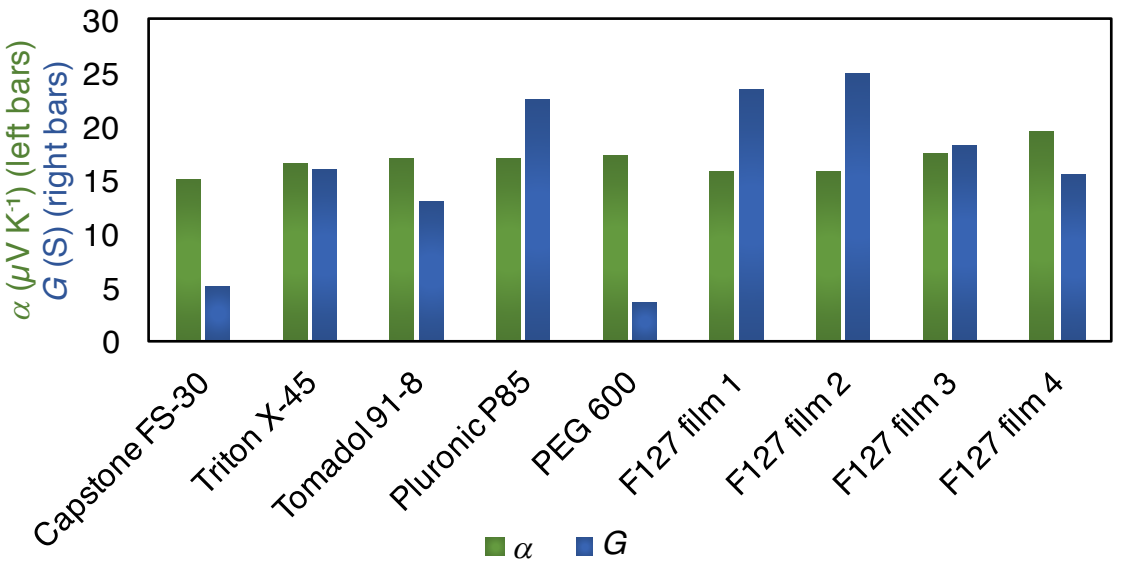

Figure 37: Seebeck coefficient (green, left bars) and conductance (blue, right bars) for PEDOT:Tos films prepared using a variety of ethoxylated additives.

Three additional films were prepared using Pluronic F127 and identical conditions. All four films prepared this way were acceptably reproducible considering the average and standard error of their α (17.1±0.9 μV K^{-1}), film thickness (639±68 nm), and G (20.5±2.2 S). Pluronic F127 was therefore used as the ethoxylated additive for the remainder of this project.

5.2.1 Effect of Oxidant to Monomer Ratio on the Conductivity and Seebeck Coefficient of PEDOT:Tos

Since the oxidant to monomer ratio can have an impact on how densely doped the product PEDOT:Tos is,[3, 122] and the extent of doping is fundamentally important to the σ and α of the material, we focused our final SCP tests on the oxidant to monomer ratio. Varying the oxidant to monomer ratio from 1:1 to 2.5:1 in 0.5 molar equivalent increments by varying the amount of the monomer added to the oxidative solution prior to SCP had a minimal impact on the film thickness, σ, and α (see Figure 38). Due to the

marginally improved σ and the reproducible film thickness obtained by using an oxidant to monomer ratio of 1.5:1, we continued to use this ratio for the preparation of PEDOT:Tos.

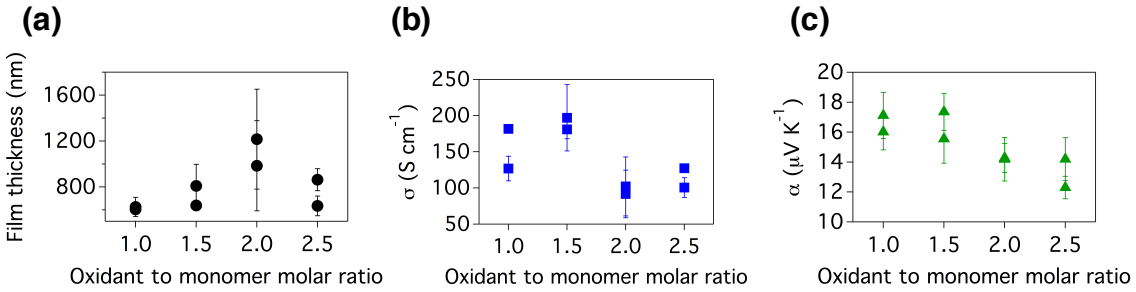

Figure 38: Effect of oxidant to monomer molar ratio on the (a) film thickness, (b) conductivity, and (c) Seebeck coefficient. Error bars represent the standard error of four measurements of the film thickness at for different locations on the films surface for (a), the combined standard error of the film thickness with the root mean square error (RMSE) of the *I-V* linear curve fit for (b), and the RMSE for the ΔV-ΔT linear curve fit for (c).

5.3 Effect of Electrochemical Oxidation and Reduction on the Conductivity and Seebeck Coefficient of PEDOT:Tos

Since PEDOT:Tos films are already doped and electrically conductive once they are prepared and remain so indefinitely, electrochemical reduction is necessary to decrease the carrier concentration to modify σ and α. Electrochemical oxidation can also be used to increase the carrier concentration, broadening the range of σ and α data further.[5] We prepared each film of PEDOT:Tos for electrochemical reduction under the same conditions, using an oxidative solution of a 1:2:3 weight ratio of Pluronic F127:ferric tosylate:*n*-butanol and an oxidant to monomer molar ratio of 1.5:1. After making 13 measurements of the film thickness of four films, it was assumed that every

film had approximately the same thickness as the average of these 13 measurements, 677±61 nm.

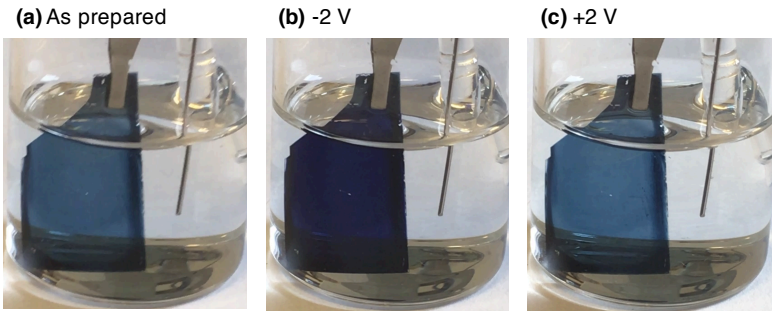

Figure 39: Electrochemical cell used to reduce or oxidize PEDOT:Tos. The PEDOT:Tos film before applying any potential is shown in (a), the PEDOT:Tos film reduced at -2 V is shown in (b), and the PEDOT:Tos film oxidized at +2 V is shown in (c). Each image was captured sequentially using the same sample of PEDOT:Tos.

Each film was electrochemically modified using an electrochemical cell by applying a constant potential for 10 minutes. The film of PEDOT:Tos being electrochemically modified was used as the working electrode, platinum wire as the counter electrode, Ag/AgCl as the reference, and 100 mM tetrabutyl ammonium perchlorate in propylene carbonate as the supporting electrolyte (see Figure 39). The color changes observed were consistent with neutral PEDOT absorbing in the visible region upon electrochemical reduction (see Figure 39b) and with p-doped polaron or bipolaron PEDOT absorbing in the infrared and near infrared upon electrochemical oxidation (see Figure 39c). Constant potentials ranging from -2 V to +1.2 V in 0.8 V increments were used to modify the extent of doping of PEDOT:Tos. The sample was washed soaking in ethanol in a petri dish and air-dried after electrochemical modification before measuring the α and σ. Electrochemical modification and α and σ measurements were all performed under atmosphere. The α and σ of PEDOT:Tos films electrochemically reduced/oxidized at each potential are shown in Figure 40.

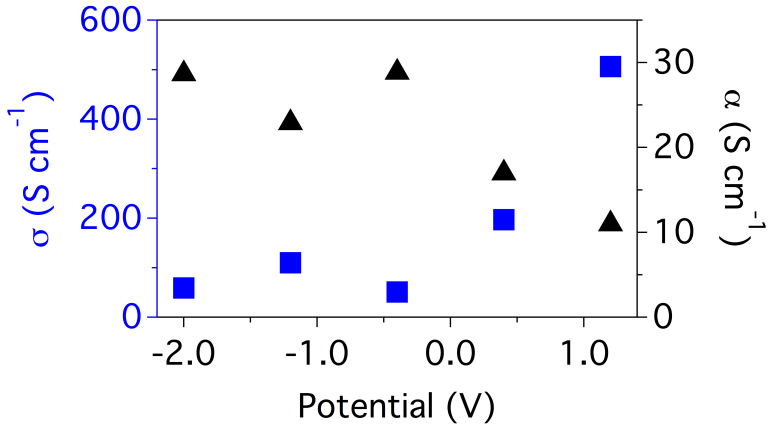

Figure 40: Dependence of conductivity (blue squares) and Seebeck coefficient (black triangles) on the potential applied to electrochemically modified PEDOT:Tos.

Decreasing the electrochemical potential resulted in increasing α and decreasing σ, which is consistent with decreasing the extent of doping of PEDOT:Tos. The complete dataset of α and σ obtained from electrochemically modified PEDOT:Tos and as prepared PEDOT:Tos (only including samples initially prepared by SCP under the same conditions) is plotted on a log-log scale in Figure 41. The dataset can be fit to Snyder and Kang's charge transport model using an s =1 or an s = 3. The trends of α vs. σ predicted by s = 1 and s = 3 are very similar to one another in the high σ, low α range where experimental data is abundant, but differ significantly at the low σ, high α range where no experimental data could be obtained. It is therefore unclear which fit, if any, best describes PEDOT:Tos prepared by SCP under the conditions described herein.

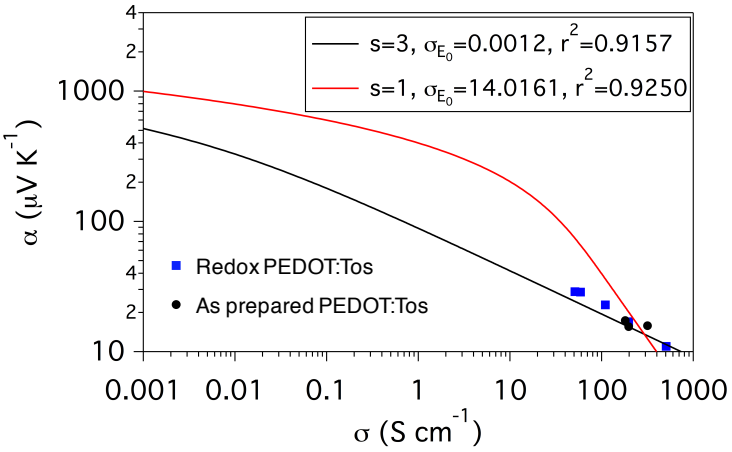

Figure 41: Compilation of PEDOT:Tos Seebeck coeffients vs. conductivities from electrochemically modified (blue squares) and as prepared (black circles) PEDOT:Tos fit with an *s* = 1 (black curve) and an *s* = 3 (red curve).

5.4 Summary and Future Outlook of Electrochemical Oxidation of PEDOT:Tos for Thermoelectric Studies

Electrochemical reduction of PEDOT:Tos using a potential of -2 V decreased σ by ~1 order of magnitude (see Figure 41). The impact of electrochemical reduction on σ we observed is less significant than what has previously been reported in the literature for PEDOT:Tos.[5] One possible reason for this discrepancy may be the exposure of our electrochemically modified PEDOT:Tos samples to atmosphere containing oxygen. It has recently been reported that oxygen can re-dope PEDOT chloride (PEDOT:Cl) that has been electrochemically de-doped,[123] enabling PEDOT to function as a conductive electrode for the oxygen reduction reaction in spite of applied electrochemical potentials that reduce PEDOT to a less conductive state. In that report, electrochemically reduced PEDOT:Cl retained a steady, low conductivity in the absence of oxygen in a nitrogen glovebox, but immediately became more electrically conductive upon exposure to oxygen, which was demonstrated by in situ resistometry in the presence and absence of

oxygen and by measure the resistance of PEDOT:Cl over time exposed to an oxygen atmosphere.

In the future continuation of this project, the impact of oxygen on the σ of electrochemically reduced PEDOT:Tos can be verified using in situ resistometry in the electrochemical cell, by first preparing PEDOT:Tos on a 4-terminal device and then measuring the σ at negative electrochemical potentials with and without sparging N_2 into the supporting electrolyte of the cell. If oxygen is found to re-dope the de-doped PEDOT:Tos, than this project must be continued by moving the electrochemical cell and thermoelectric apparatus into a glovebox. I did not attempt to rearrange this equipment in our lab, in part due to the conflicting research demands on our thermoelectric apparatus. The in situ measurement of the thermoelectric properties of iodine doped conjugated polymers as the spontaneously dedope, as described in the previous chapter, releases iodine vapor to the surroundings as the film dedopes. These experiments are not practical to perform in a glovebox, since the release of iodine vapor within the glovebox would jeopardize all chemicals stored in the same box and the catalyst of the glovebox.

Addressing the issue of the persistently high conductivity of PEDOT:Tos in the future would enable the characterization of a broader range of σ and α and a better understanding of its charge transport. Furthermore, the spatial distribution of dopants within PEDOT:Tos could possibly be tuned by controlling the conditions of re-doping the electrochemically de-doped PEDOT. For instance, electrochemically reduced PEDOT could be electrochemically oxidized back to a conductive state using a less permeable dopant than tosylate, such as PSS. This would be expected to create disparate regions, including regions of PEDOT where PSS is unable to permeate and regions on the surface

of PEDOT with a relatively denser distribution of PSS dopants. Controlling the temperature during electrochemical oxidation may be an additional way to influence the dopant permeability and resulting spatial distribution of dopants, as we observed during the chemical oxidation of PDPP4T described in the previous chapter (see Figures 31 and 32). Ultimately, the preparation of PEDOT films with a broad range of conductivities and varying spatial homogeneity of dopant counterions and characterization of the thermoelectric properties would lead to an improved explanation of the unique thermoelectric properties reported for PEDOT:Tos.

APPENDIX

EXPERIMENTAL SECTION

A.1 Synthesis and Characterization of Rylenediimide Monomers and Polymers

A.1.1 Materials

Acetic acid, acetone, acetonitrile, bromine, chlorobenzene, chloroform, 1,3-dibromo-5,5-dimethylhydantoin (DBH), dichloromethane, *n*-dodecylamine, 1,4,5,8-naphthalenetetracarboxylic dianhydride (NDA), ferrocene, *n*-octadecylamine, 2,2,3,3,4,4,4-heptafluorobutylamine, hexane, methanol, tetrahydrofuran (THF), $Pd(PPh_3)_4$, tetrabutylammonium cyanide (TBACN), tetrabutylammonium perchlorate (TBAP), tetrakis(dimethylamino)ethylene (TDAE), trans-1,2-bis(tri-n-butylstannyl)ethylene, 1,2,4-trichlorobenzene (TCB), toluene, dihexyl ketone, NH_4OAc, $NaBH_3CN$, imidazole, perylene-3,4,9,10-tetracarboxylic dianhydride, 7-tridecanamine, ethanol, and were purchased from commercial vendors and used as received unless otherwise stated. Toluene was dried by storage over 4 Å molecular drying sieves and degassed by sparging with N_2 for no less than one hour.

A.1.2 Instrumentation and Characterization

^1H NMR and ^{13}C NMR spectra were recorded on a 400 MHz Bruker Avance NMR spectrometer, ^{19}F NMR spectra were recorded on a 500 MHz Bruker Ascend NMR spectrometer. All the NMR spectra and chemical shifts were mentioned with respect to tetramethylsilane (TMS) internal standard in parts per million (δ scale). Gel permeation chromatography (GPC) analyses were performed on a HT-GPC, PL-GPC220, solvent: TCB, normal operating temperature: 135 °C. Absorption spectra were taken using a

Shimadzu UV 3600 UV-Vis-NIR spectrometer. Polymer thin films for UV-Vis-NIR spectroscopy were prepared by spincasting onto ITO-coated glass slides from chlorobenzene solution. The electrochemical properties were performed by using a three electrode system on a CV-50W electrochemical analyzer using a Pt disk (dia. 1.6 mm) and a platinum (Pt) wire as working electrode and as counter electrode respectively, with a reference electrode of Ag/AgCl. TBAP (0.1 M in N_2-purged dry acetonitrile) was utilized as the supporting electrolyte and ferrocene was used as an internal standard (the calculated half-wave potential for ferrocene/ferrocenium couple was found to be 0.32 V). Thermogravimetric study (TGA) was performed on a TGA Q50 instrument and differential scanning calorimetry (DSC) was performed on a DSC Q200 instrument. EPR spectra were collected at room temperature on a Bruker Elexsys E-500 at X-band. The two-terminal electronic devices were fabricated by vacuum depositing Au electrodes (100 nm) onto a clean glass substrate with a channel width and length at 5 mm and 165 μm, respectively, using a shadow mask. Solutions of a predetermined amount of polymer or polymer and TBACN in THF were dropcast onto these electrodes. Poling at a constant voltage was performed for a duration of time to ensure that the current measured was electronic and not ionic, and the final 30 measurements of current (the final 2.5 seconds of poling) were assumed to be the steady-state, electronic current for *I-V* characterization. All *I-V* characterization was carried out under ambient conditions at room temperature using Keithley 2440-5A SourceMeter. The film thicknesses were determined by profilimetry using a KLA Tencor Alpha-Step IQ Surface Profiler. DFT calculations were performed within the ωB97XD/6-31g(d,p) basis, with the geometry of each NDIV oligomer optimized

with vinylene end groups on each end and all hydrocarbon side chains replaced with ethyl groups.

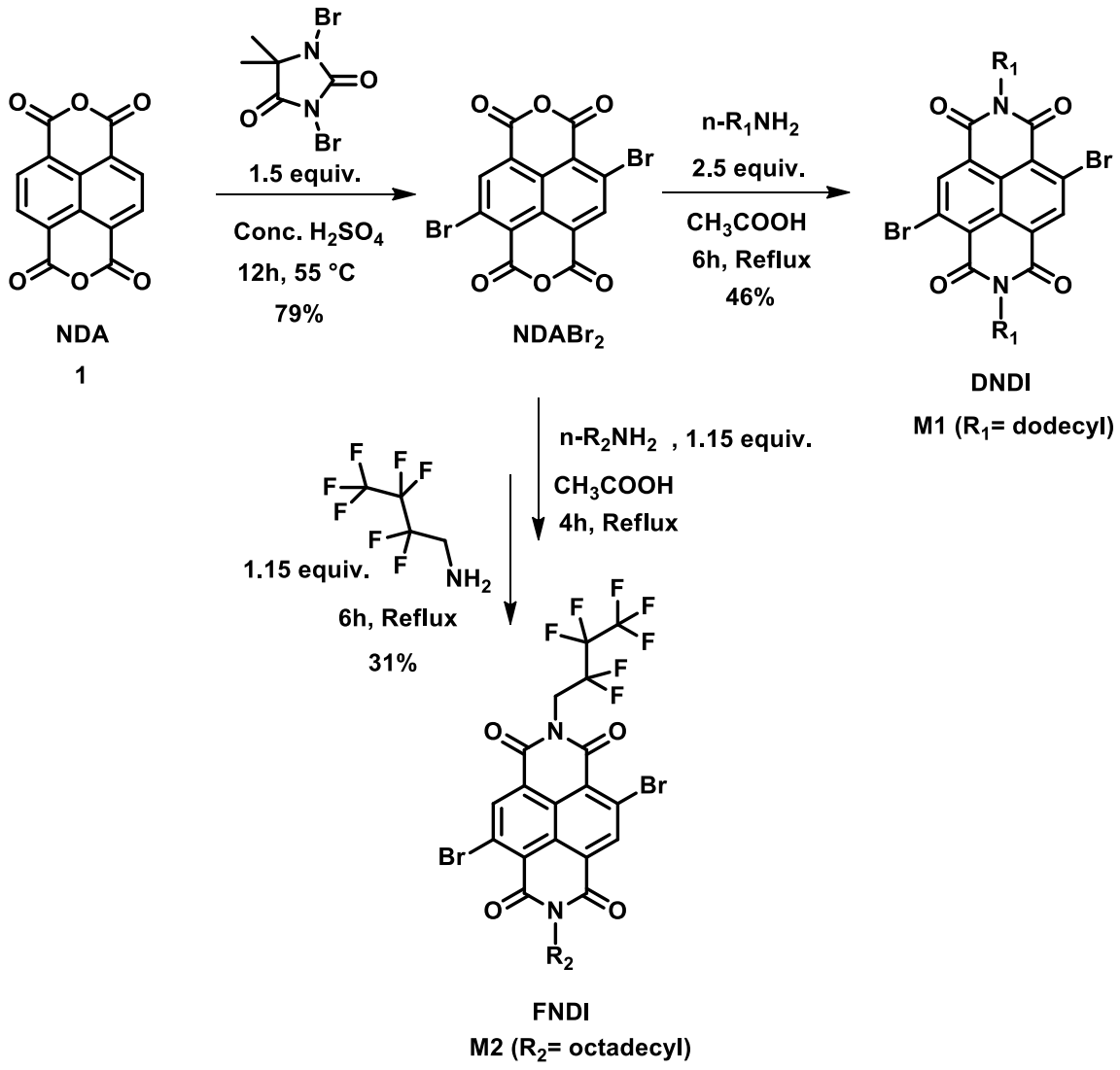

Figure 42: Synthetic scheme for the monomers DNDI and FNDI.

A.1.3 Experimental Procedures

The synthetic scheme of the monomers DNDI and FNDI is shown in Figure 42, and the synthetic scheme of the regioisomeric monomers for PDIV is shown in Figure 43.

A.1.3.1 Synthesis of 2,6-Dibromo-1,4,5,8-naphthalenetetracarboxylic Dianhydride ($NDABr_2$).

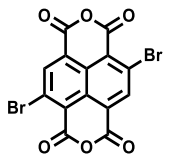

$NDABr_2$ was prepared in a modified version of the previously reported procedure.[1] In a single-necked RB flask, NDA (1.34 g, 5 mmol) was stirred at room temperature in concentrated sulfuric acid (15 mL) for 5 min. DBH (2.14 g, 7.5 mmol) was added in portion wise over a period of 40 min at room temperature. The resulting brown solution was stirred at 55 °C for 12 h. In order to precipitate the solid, the mixture was poured over crushed ice. Filtration of the precipitated solid was done, further washed with water (100 ml) followed by methanol (100 ml) then dried in vacuum to obtain $NDABr_2$ which was used for next steep without farther purification (1.68 g, 79 %). ^{1}H NMR (400 MHz, [D_6]DMSO): δ 8.78 (s, 2H).

A.1.3.2 Synthesis of *N, N′*-bis(*n*-dodecyl)-2,6-dibromo-1,4,5,8-naphthalenedicarboxiimide (DNDI).

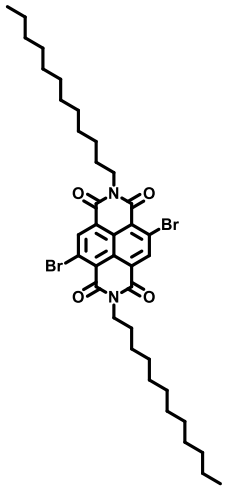

A mixture of $NDABr_2$ (423 mg, 1 mmol), *n*-dodecylamine (462 mg, 2.5 mmol), and acetic acid (20 mL) was stirred at 90 °C under N_2 atmosphere for 8 hours. The mixture was cooled to room temperature followed by addition of 80 ml of cold water. A yellow precipitate formed upon cooling and was separated by gravity filtration, washed with 100 ml of methanol and dried under vacuum. Final purification was done by column chromatography eluting with hexane/chloroform (60 : 40) to obtain DNDI as a yellow solid (350 mg, 46%). ^{1}H NMR (400 MHz, $CDCl_3$): δ 8.99 (s, 2H), 4.18 (t, J = 7.6 Hz, 4H), 1.78–1.68 (m, 4H), 1.44–1.34 (m, 8H), 1.30–1.22 (m, 28H), 0.89–0.85 (m, 6H). ^{13}C NMR (100 MHz, $CDCl_3$): δ 160.76, 160.73, 139.07, 128.32, 127.73, 125.36, 124.10, 41.62, 31.91, 29.62, 29.61, 29.56, 29.51, 29.34, 29.29, 27.90, 27.08, 22.69, 14.11.

A.1.3.3 Synthesis of *N*-(2,2,3,3,4,4,4-heptafluorobutyl)-*N*'-octadecyl-2,6-dibromo-1,4,5,8-naphthenedicarboximide (FNDI).

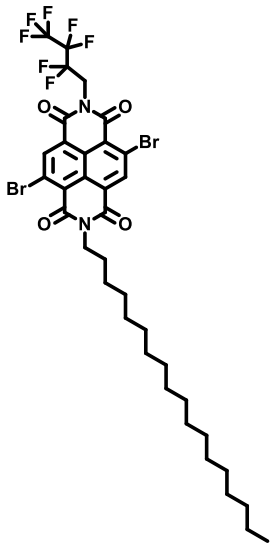

A mixture of $NDABr_2$ (423 mg, 1 mmol), *n*-octadecylamine (309 mg, 1.15 mmol), and acetic acid (20 mL) was stirred at 90 °C under N_2 atmosphere for 4 hours before 2,2,3,3,4,4,4-heptafluorobutylamine (228 mg, 1.15 mmol) was added to the same reaction

mixture at the same temperature and stirred for another 6 hours. The mixture was cooled to room temperature followed by addition of 80 ml of cold water. A precipitate that formed upon cooling was separated by gravity filtration, washed with 50 ml of methanol and dried under vacuum. Final purification was done by column chromatography eluting with hexane/chloroform (40 : 60) to obtain FNDI as a greenish yellow solid (266 mg, 31%). ^{1}H NMR (400 MHz, $CDCl_3$): δ 9.04 (s, 1H), 9.02 (s, 1H), 5,03 (t, J = 15.2 Hz, 2H), 4.19 (t, J = 7.6 Hz, 2H), 1.77–1.71 (m, 2H), 1.45–1.34 (m, 4H), 1.34–1.26 (m, 26H), 0.90–0.85 (m, 3H). ^{19}F NMR (500 MHz, $CDCl_3$): δ −80.41 (t, 3F), −115.85 (m, 2F), −127.60 (br, 2F). ^{13}C NMR (100 MHz, $CDCl_3$): δ 160.63, 160.51, 160.29, 139.79, 139.15, 129.45, 128.36, 127.90, 127.80, 125.89, 124.79, 124.35, 123.36, 41.71, 38.80, 31.91, 29.69, 29.65, 29.63, 29.57, 29.51, 29.35, 29.27, 27.88, 27.06, 22.68, 14.11.

A.1.3.4 Synthesis of PDNDIV

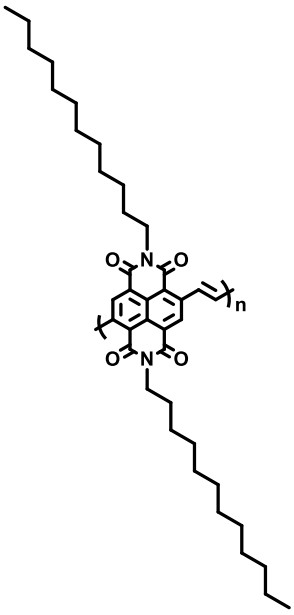

DNDI (76 mg, 0.10 mmol), and trans-1,2-bis(tri-n-butylstannyl)ethylene (61 mg, 0.1 mmol) were added to 3 mL of dry toluene in a two-necked 25 ml round-bottom flask

under nitrogen. The solution was purged with nitrogen for 10 min. Then, $Pd(PPh_3)_4$ (5.8 mg, 5 mol %) was added to the solution and the mixture was refluxed for 12 h. The crude reaction mixture was then precipitated in 30 ml methanol and collected by gravity filtration, after which the resulting solution was subjected to Soxhlet extraction with methanol, acetone, and hexane as washing solvents. A final chloroform extraction resulted in a deep red colored solution, which was then reprecipitated from 10 ml methanol and dried under a vacuum to yield reddish black polymer PDNDIV (40 mg, yield 61%). ^{1}H NMR (400 MHz, $CDCl_3$): δ 9.19 (br, 2H) 8.93 (br, 2H), 4.20 (br, 4H), 1.83−1.69 (br, 4H), 1.40−1.15 (br, 36H), 0.94−0.76 (br, 6H).

A.1.3.5 Synthesis of PFNDIV

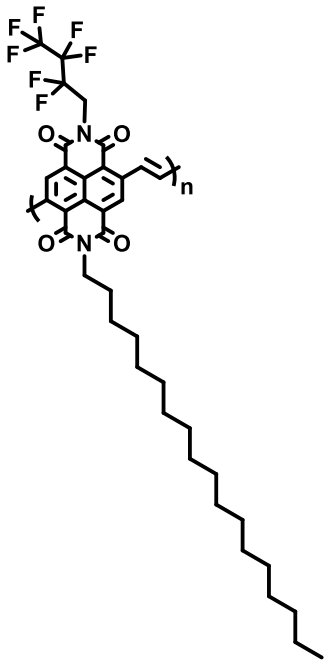

FNDI (86 mg, 0.10 mmol), and trans-1,2-bis(tri-n-butylstannyl)ethylene (61 mg 0.1 mmol) were added to 4 mL of dry toluene in a two-necked 25 ml round-bottom flask under nitrogen. The solution was purged with nitrogen for 15 min. Then, $Pd(PPh_3)_4$ (5.8 mg, 5

mol %) were added to the solution and the mixture was refluxed for 12 h. The crude reaction mixture was then precipitated in 40 ml methanol and collected by gravity filtration. The resulting solution was subjected to Soxhlet extraction with methanol, acetone, and hexane as washing solvents. A final chloroform extraction resulted in a deep red colored solution, which was then reprecipitated from 10 ml methanol and dried under a vacuum to yield reddish black polymer PFNDIV (54 mg, yield 73%). ^{1}H NMR (400 MHz, $CDCl_3$): δ 9.21 (br, 2H), 8.91 (br, 2H), 5.07 (br, 2H), 4.21 (br, 2H), 1.74 (br, 2H), 1.48−1.10 (br, 30H), 0.99−0.76 (br, 3H).

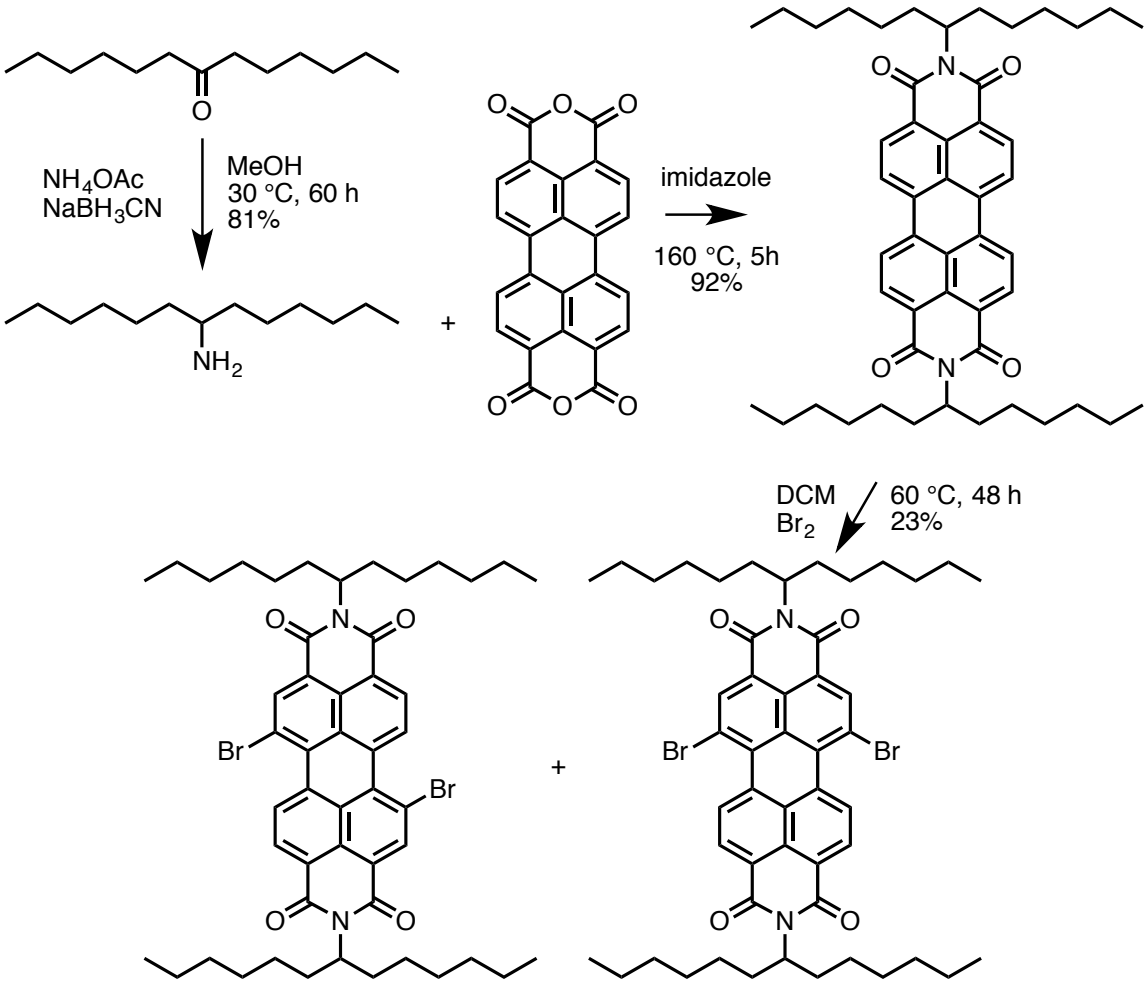

Figure 43: Synthetic scheme for the regioisomeric mixture of monomers for PDIV.

A.1.3.6 Synthesis of 7-tridecanamine

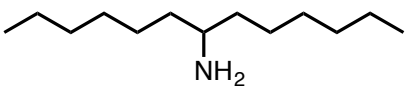

Methanol (152 mL), dihexyl ketone (10 g, 50 mmol), , NH_4OAc (40 g, 520 mmol), and then $NaBH_3CN$ (2.24, 36 mmol) were sequentially added to a 1 L RB flask with continuous magnetic stirring. The flask was lowered into a 30 °C water bath and magnetically stirred at 30 °C for 60 h. The mixture was quenched by the addition of 8 mL concentrated hydrochloric acid and concentrated by rotary evaporation. The crude product was suspended in 1 L of water and brought to basic pH by addition of NaOH pellets with stirring. The product was extracted using 3 × 250 mL of dichloromethane and concentrated to obtain a clear, colorless oil that crystallizes after storing at ambient temperature for several days (8.14 g, 81%). ^{1}H NMR (400 MHz, $CDCl_3$): δ 2.68 (q, 1H), 1.30 (m, 20H), 0.87 (t, 6H).

A.1.3.7 Synthesis of *N,N*'-bis(1-hexylheptyl)-3,4,9,10-perylenediimide

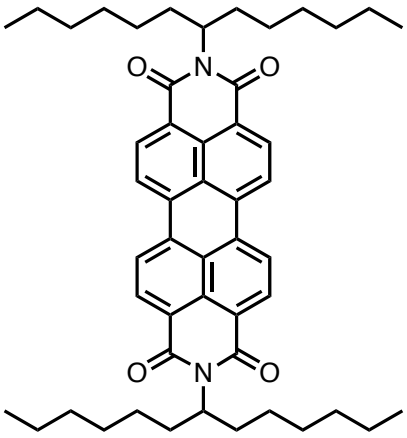

A 300 mL flat-bottomed flask was charged with imidazole (3.70 g, 54 mmol), perylene-3,4,9,10-tetracarboxylic dianhydride (0.82 g, 2 mmol), and 7-tridecanamine (1.00 g, 5 mmol), loosely covered with a watch glass, and placed in a 160 °C oven. The crude

product was allowed to cool to ambient temperature and then stirred in 30 mL ethanol and 84 mL 2 N HCl for 12 h. The product was isolated by vacuum filtration, washed with 300 mL water three times and then 300 mL ethanol once, and then dried in vacuo to obtain a red powder (1.46 g, 92%). ^{1}H NMR (400 MHz, $CDCl_3$): δ 8.66 (m, 8H), 5.19 (m, 2H), 2.52 (m, 4H), 1.86 (m, 4H), 1.24 (m, 32H), 0.82 (t, 12H).

Synthesis of *N*,*N*'-bis(1-hexylheptyl)-1,7/1,6-dibromo-3,4,9,10-perylenediimide ($PDIBr_2$)

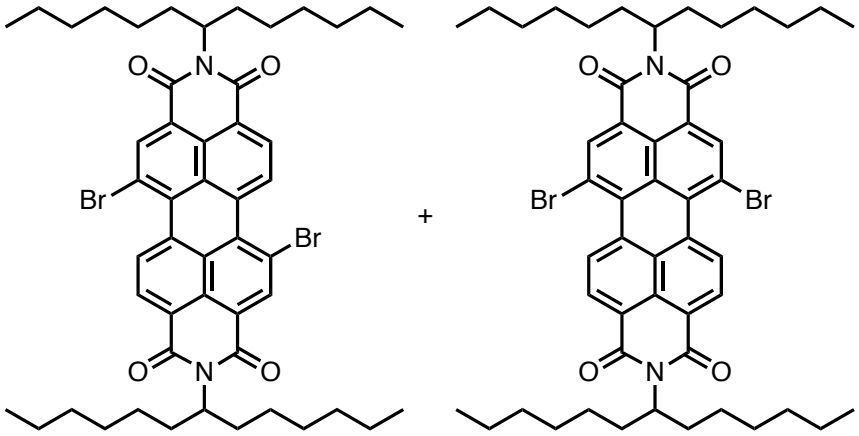

A 100 mL glass reaction tube containing a magnetic stir bar was charged with a solution of *N*,*N*'-bis(1-hexylheptyl)-3,4,9,10-perylenediimide (1.46 g, 1.93 mmol) in 36 mL dichloromethane and its neck was sealed by closing the stopcock. The solution was brought to reflux by stirring in a 60 °C oil bath. The stopcock was opened and bromine (23.00 g, 144 mmol) was added. The reaction tube was resealed by closing the stopcock and the reaction was stirred at 60 °C for 48 h. The solvent and excess bromine were removed by a stream of air followed by rotary evaporation. Column chromatography using a gradient elution of dichloromethane:hexanes from 1:3 to 1:1 yielded a regio-isomeric mixture of the product as a dark red powder (402 mg, 23%). ^{1}H NMR (400 MHz, $CDCl_3$):

δ 9.50 (m, 2H), 8.92 (m, 2H), 8.69 (m, 2H), 5.16 (m, 2H), 2.24 (m, 4H), 1.84 (m, 4H), 1.31 (m, 32H), 0.83 (t, 12H).

Synthesis of PDIV

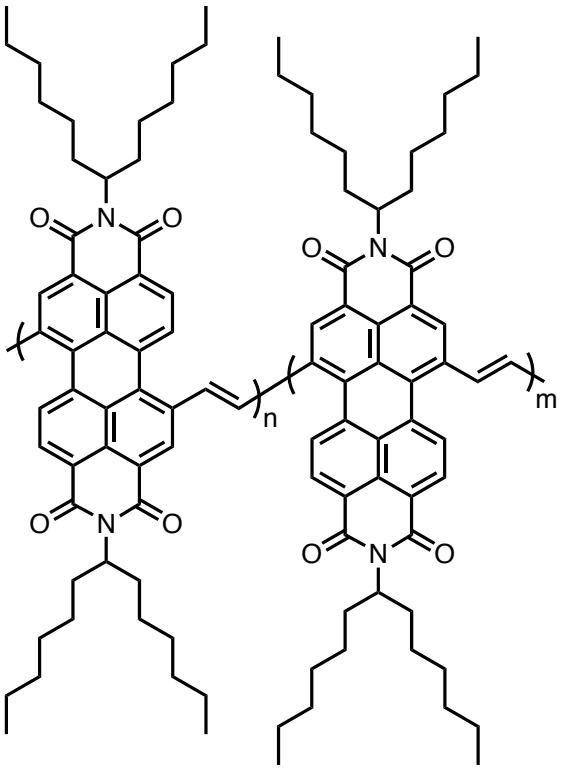

A 200 mL RB flask was charged with the regioisomeric mixture of $PDIBr_2$ (400 mg, 0.0219 mmol) and $Pd(PPh_3)_4$ (25 mg, 5 mol %), brought into a N_2 glovebox, fitted with a reflux condenser sealed with a septum, and brough out of the glovebox. 20 mL toluene was added to the reaction flask by cannular transfer under N_2. A solution of trans-1,2-bis(tri-n-butylstannyl)ethylene (266 mg, 0.438 mmol) in 20 mL toluene was degassed by sparging with N_2 for 20 minutes and added to the reaction flask by cannular transfer under N_2. The reaction flask was lowered into a 90 °C oil bath and stirred under N_2 for 24 h. An additional aliquot of $Pd(PPh_3)_4$ (25 mg, 5 mol %) was added under N_2, and the mixture was heated to reflux and stirred under N_2 for 24 h. The polymer was obtained by

sequential precipitation into methanol, vacuum filtration, and column chromatography using chloroform as the eluent to obtain a dark purple powder (277 mg, 81%).

A.2 Materials used to prepare blends of SWNT with PBTDV2

PBTDV2 was prepared by Dr. Timothy Gehan for a previous research project according to the reported procedure.[10] SWNT (diameter 0.7-1.4 nm) from a commercial vendor was donated by Prof. Paul Lahti. *o*-DCB and iodine were purchased from commercial vendors and used as received.

A.3 Preparation, Doping, Characterization, KPFM, and Modeling of P3HT and PDPP4T

A.3.1 Materials

P3HT (M_w = 90 kDa, 96% HT regioregularity), PDPP4T (M_w = 171,138 Da, $Đ$ = 2.45), chloroform, and iodine were purchased from commercial vendors and used as received.

A.3.2 Film Preparation

Solutions of 5 mg/mL P3HT or 8 mg/mL PDPP4T in chloroform were stirred for no less than 4 h before drop-casting. 0.23 mL of the polymer solution was drop cast onto a handcut, 1.1 cm × 2.2 cm glass coverslip that was preheated to 45 °C on a hot plate, and this was immediately covered with a watch glass to impede the escape of chloroform vapors and slow the rate of evaporation during drop-casting. After 10 min, the sample heating element was turned off, and the sample was let stand under ambient conditions for no less than 24 h to evaporate the chloroform further.

A.3.3 Doping with Iodine Vapor

50±5 mg iodine crystals were loaded into a 1 mL glass vial, and this vial was loaded into a 20 glass mL vial. For samples doped at 25 °C, the 20 mL vial was first capped and let stand for no less than 12 h to allow solid-vapor equilibration of the iodine within the vials. For samples doped at 75 °C, the 20 mL vial was first capped and let stand in a 75 °C oven for 10 min to allow solid-vapor equilibration of the iodine within the vials while the polymer film was simultaneously heated to 75 °C for 10 min. In each case, the iodine doping was carried out by placing the polymer film into the 20 mL vial (which contained iodine vapor and the 1 mL vial of 50±5 mg iodine), capping the vial, and heating to the specified temperature for 2 h.

A.3.5 Simulation Details

Our charge transport model is based on electron hopping between localized sites and the hopping rate between sites (i-j) is calculated from the Miller-Abrahams rate equation[86] $W_{ij} = \nu_0 exp\left(-2\gamma_{ij}R_{ij}\right)\left[N\left(\Delta E_{ij}\right) + \frac{1}{2} \pm \frac{1}{2}\right]$, where ν_0=5×10^{12} s^{-1} is the attempt to escape frequency, γ=1 is the overlap factor ($\gamma_{ij}=\gamma_i+\gamma_j$, γ_i and γ_j are the site-specific contributions obtained from a Gaussian distribution of width $\sum_{ij}=0.25$) and R_{ij} is the distance between the sites. $\Delta E_{ij} = E_j - E_i - eF\Delta R_{ij,x}$ where, E_i and E_j are the energies of the sites and F=10^6 Vm^{-1} is the externally applied electric field. These are the values used throughout the simulation unless stated otherwise. $N(E)$ is the Bose-Einstein distribution with $+\frac{1}{2}$ for hops upwards in energy ($E_i > E_j$) by absorption of a phonon and $-\frac{1}{2}$ for downward hops with the emission of a phonon.

We numerically solve the Pauli master equation to compute the time-averaged occupational probabilities of the sites using a non-linear iterative solver, and the initial site occupation probability is given by the Fermi-Dirac distribution.[124] In steady-state, $\frac{dp_i}{dt} = 0 = \Sigma_j[W_{ij}p_i(1-p_j) - W_{ji}p_j(1-p_i)]$ where, p_i is the occupation probability of a site i and W_{ij} is the hopping transition rate, and the whole term is summed over the neighbor sites j. The current density J is found by a summation over all the carriers in the direction of the applied field, $J = \frac{e}{a^3 N}\sum_{i,j} W_{ij}p_i(1-p_j)R_{ij,x}$ and the Seebeck coefficient is calculated as $S = \frac{E_F - E_T}{eT}$ where, E_T is the average transport energy, calculated from $E_T = \langle E_i \rangle = \frac{\sum_{i,j} E_i W_{ij} p_i(1-p_j)R_{i,j,x}}{\sum_{i,j} W_{ij} p_i(1-p_j)R_{i,j,x}}$.[47,50,52]

We simulate a 35×25×25 lattice of sites with an average distance between adjacent sites a=0.38 nm, and consider up to the third-nearest neighbor, which implies a maximum hopping distance of $\sqrt{3a}$. Each site is randomly assigned an energy from a dopant-induced DOS distribution calculated from[72]

$$g(E) = \frac{4\pi q^6 N_d C_s^3}{(4\pi\varepsilon_0\varepsilon)^3}\int_{-\infty}^{0}\frac{dE_c}{E_c^4}\exp\left[\frac{4\pi N_d C_s^3}{3}\frac{q^6}{(4\pi\varepsilon_0\varepsilon E_c)^3}\right] g_i(E-E_c) \quad (3)$$

where, N_i and N_d are the intrinsic and dopant concentration respectively, C_s is the number of dopants in each cluster, E_c is the potential energy of the Coulomb interaction and g_i is the intrinsic Gaussian DOS. Further details of our model have been described in the Supplementary Information and an upcoming report.[125]

A.3.6 KPFM and PL instrumentation and characterization

KPFM experiments were conducted on a Digital Instruments Bioscope Atomic Force Microscopy (AFM), with AppNano ANSCM-PA Platinum-coated Si cantilever probe. The probe possesses a resonance frequency of around 254 kHz. A mixed AC and DC voltage electrical excitation signal was applied between the probe, lifted by 40 nm, and the grounded sample, to acquire the surface potential contrast. The scan rate was set to be 0.4 Hz, and the sampling density was 512 lines and 512 samples per line.

The PL imaging was conducted with a Princeton Instrument Acton Photomax 512 EMCCD camera, which was cooled down thermoelectrically to -70 °C. The images were captured at an exposure time of 0.2 s.

A.4 Preparation of PEDOT:Tos

A.4.1 Materials

EDOT, anhydrous $FeCl_3$, *p*-toluenesulfonic acid monohydrate, methanol, *n*-butanol, Pluronic F127, Capstone FS-30, Triton X-45, Tomadol 91-8, Pluronic P85, PEG 600, and ethanol were all purchased from commercial vendors and used as received.

A.4.2 Synthesis of Ferric Tosylate

A solution of NaOH (4.44 g, 111 mmol) in 30 mL water was poured into a magnetically stirred solution of $FeCl_3$ (6.00 g, 37.0 mmol) in 140 mL water in a 300 mL RB flask. A brown precipitate immediately formed and was isolated by vacuum filtration and washed with 200 mL water twice. The brown precipitate was transferred back into the 300 mL RB flask without completely drying it and suspended in 70 mL of methanol with stirring. The reaction was charged with a solution of *p*-toluenesulfonate (20.00 g,

105.1 mmol) in 30 mL methanol and stirred at 45 °C for 3 h. The solution was subjected to hot filtration and concentrated by rotary evaporation to the crude product as an organge solid. Purification by sonication in hot diethyl ether, vacuum filtration, washing with diethyl ether, and drying in vacuo yielded ferric tosylate as an organge solid (16.24 g, 81%).

A.4.3 Solution Casting Polymerization of PEDOT:Tos

Oxidative solutions were prepared by stirring the desired amount of ferric tosylate at 50 °C in *n*-butanol for 2 h before adding the desired amount of weak base additive(s) and stirring for no less than 12 h. For example, to prepare a stock solution of the oxidative solution used most frequently in this research, ferric tosylate (2.00 g, 3.51 mmol) and *n*-butanol (3.00 g, 40.5 mmol) were stirred at 50 °C for 2 h. Pluronic F127 (1.00 g) was added to this and the solution was stirred for an additional 10 h. This solution could stored at 50 °C and cooled to 30 °C immediately before use. Prolonged storage at temperatures ≥~30 °C resulted in precipitation of insoluble solids.

For each film of PEDOT:Tos, 600 mg of oxidative stock solution [i.e. Pluronic F127 (100 mg), ferric tosylate (200 mg, 0.35 mmol), and *n*-butanol (300 mg, 4.05 mmol)] were stirred in a 7 mL glass vial at 30 °C.

EDOT (25 μL, 0.23 mmol) was injected into the stirred 600 mg oxidative solution. ~0.2 mL of this solution was immediately spincast in a home-built, humidity controlled chamber with a relative humidity of 35% onto a hand-cut 1.1 cm 2.2 cm glass slide using 0 RPM for 60 s, to allow the liquid to wet the substrate, followed by 2000 RPM for 30 s. The film was transferred to a 70 °C hot block, at 35% relative humidity, for 2 h, where it immediately turned blue from its initial yellow-brown color. The film

was allowed to cool to ambient temperature for 20 minutes before washing by soaking in ethanol in a plastic petri dish for 1 minute 3 times, sequentially, using fresh ethanol for each wash. Ethanol had to be added dropwise, slowly, to the petri dish containing the film to avoid delaminating it. Films were dried under ambient conditions for at least 12 h before measuring the conductivity and Seebeck coefficient or electrochemical modification.

A.5 Measuring the Thermoelectric Properties

The custom-built thermoelectric characterization apparatus used in this work is reported elsewhere.[47-48, 52] In brief, a temperature gradient is established by heating one of two copper blocks and the film being tested is placed onto a glass slide that bridges the copper blocks. Four Pt wire contacts are made by firmly clamping a home-built PTFE block with the Pt wire contacts located on the bottom into the sample, with the innermost contacts used to measure the resistance and thermovoltage spaced 1.4 cm apart. Type K thermocouples were inserted into holes in the PTFE block, located just outside the 1.4 cm spaced Pt contacts were were assumed to by equidistant to the 1.4 cm Pt contacts.

The conductance, *G*, was taken to be the slope of the *I*-*V* curve and σ was calculated from the relation $\sigma = \frac{Gl}{A}$. *l* is the length between Pt electrodes, 1.4 cm, and *A* is the area of the device $w \times t$ where *w* is the width of the film and *t* is the thickness obtained from profilometry after thermoelectric measurements were finished.

A.5.1 Conductivity and Seebeck Coefficent of Iodine Doped P3HT and PDPP4T

Samples were transferred from their iodine doping chamber to the thermoelectric characterization apparatus in a timely fashion since they began dedoping immediately

and rapidly in the absence of iodine vapor. A temperature gradient of ~20 °C with an average temperature of ~50 °C was applied to P3HT, and a temperature gradient of ~10 °C with an average temperature of ~45 °C was applied to PDPP4T. A LabView program was used to interface with a digital dual input thermometer with k-type thermocouples, a Keithley 6182 nanovoltmeter, and a Keithley 2440 source meter to repeat measurements of the temperature gradient ΔT, voltage gradient ΔV, and *I-V* characteristics across the sample sequentially and repeatedly every 10 minutes for P3HT and every 2 minutes for PDPP4T. ΔV was taken to be the average of 1000 voltage measurements from the Keithley 6182 nanovoltmeter, and α was taken to be $\Delta V/\Delta T$. Only measurements for which the standard deviation of the 1000 voltage measurements is less than 1% of their mean are used to calculate α to ensure only reliable estimates of α are considered.

A.5.2 Conductivity and Seebeck Coefficent of SWNT:PBTDV2 blends and PEDOT:Tos

The *I-V* curve for determining the *G* and σ before applying any temperature gradient. Temperature gradients in the range of 0-10 °C were applied to the sample and the sample was allowed to equilibrate for 1.5-2.5 h before measuring 1000 Keithley 6182 nanovoltmeter voltage measurements at each temperature gradient. α was determined to be from the linear fit from the ΔV vs. ΔT curve, as depicted in Figure 44. The advantages of fitting an entire range of ΔV vs. ΔT instead of calculating a from a single $\Delta V/\Delta T$ point include the confirmation that α is relatively independent of the average temperature in the temperature range being studied and the cancellation of any non-thermoelectric potentials that may be present in the sample.

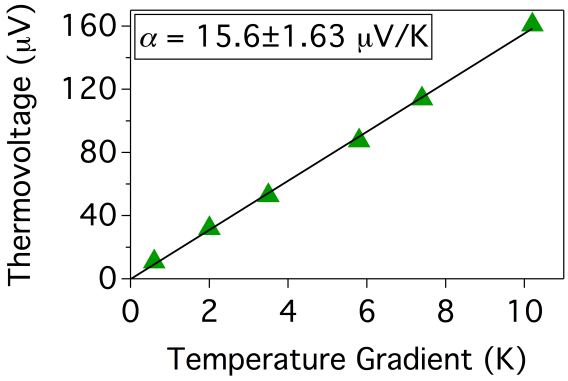

Figure 44: A thermovoltage (ΔV) vs. temperature gradient (ΔT) curve for PEDOT:Tos used to determine the Seebeck coefficient.

Since P3HT and PDPP4T constantly and rapidly changed their Seebeck coefficient due to their spontaneous dedoping, measuring the multipoint ΔV vs. ΔT curve was impractical since the sample would de-dope significantly during the necessary ~7.5 h of data acquisition. To verify that the single $\Delta V/\Delta T$ point methodology described for P3HT and PDPP4T in Section A.5.1 provides a reasonable estimate of α, the single $\Delta V/\Delta T$ point calculation was also performed for 8 PEDOT:Tos samples, for comparison with the multipoint ΔV vs. ΔT curve determined the α of the same samples. Only the $\Delta V/\Delta T$ point at the greatest ΔT value was used to determine α from a single point. The methods of calculating the Seebeck coefficient for PEDOT:Tos are comparable, with relative errors (assuming the multipoint ΔV vs. ΔT curve Seebeck coefficient is the correct value) of 1-2%, as shown if Figure 45. This confirms that estimating α from a single $\Delta V/\Delta T$ point was valid for P3HT and PDPP4T.

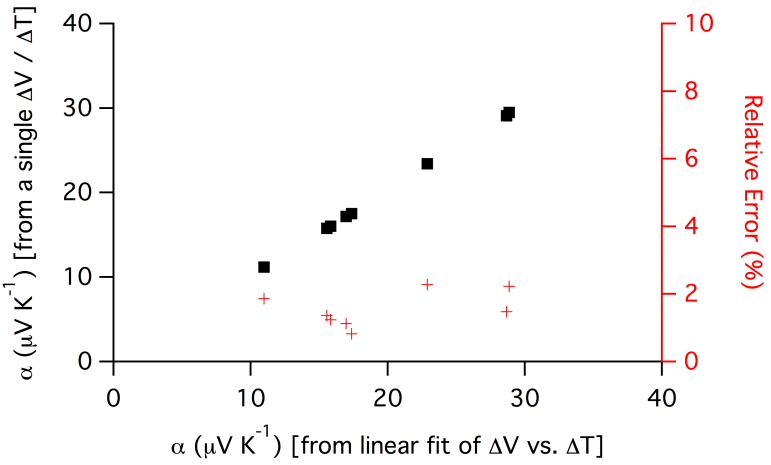

Figure 45: Single-point Seebeck coefficient calculations (black squares) and relative error (red crosses) for PEDOT:Tos compared to their multi-point Seebeck coefficient calculations.

BIBLIOGRAPHY

1. Rowe, D. M., *CRC Handook of Thermoelectrics*. CRC Press: 1995.

2. Fritzsche, H., A general expression for the thermoelectric power. *Solid State Commun.* **1971,** *9* (21), 1813–1815.

3. Bubnova, O.; Khan, Z. U.; Malti, A.; Braun, S.; Fahlman, M.; Berggren, M.; Crispin, X., Optimization of the thermoelectric figure of merit in the conducting polymer poly(3,4-ethylenedioxythiophene). *Nat. Mater.* **2011,** *10* (6), 429–433.

4. Kim, G.-H.; Shao, L.; Zhang, K.; Pipe, K. P., Engineered doping of organic semiconductors for enhanced thermoelectric efficiency. *Nat. Mater.* **2013,** *12* (8), 719–723.

5. Park, T.; Park, C.; Kim, B.; Shin, H.; Kim, E., Flexible PEDOT electrodes with large thermoelectric power factors to generate electricity by the touch of fingertips. *Energy Environ. Sci.* **2013,** *6* (3), 788–792.

6. Yuan, D.; Huang, D.; Zhang, C.; Zou, Y.; Di, C.-a.; Zhu, X.; Zhu, D., Efficient Solution-Processed n-Type Small-Molecule Thermoelectric Materials Achieved by Precisely Regulating Energy Level of Organic Dopants. *ACS Appl. Mater. Interfaces* **2017,** *9* (34), 28795–28801.

7. Huang, D.; Yao, H.; Cui, Y.; Zou, Y.; Zhang, F.; Wang, C.; Shen, H.; Jin, W.; Zhu, J.; Diao, Y.; Xu, W.; Di, C.-a.; Zhu, D., Conjugated-Backbone Effect of Organic Small Molecules for n-Type Thermoelectric Materials with ZT over 0.2. *J. Am. Chem. Soc.* **2017,** *139* (37), 13013–13023.

8. Shi, K.; Zhang, F.; Di, C.-A.; Yan, T.-W.; Zou, Y.; Zhou, X.; Zhu, D.; Wang, J.-Y.; Pei, J., Toward High Performance n-Type Thermoelectric Materials by Rational Modification of BDPPV Backbones. *J. Am. Chem. Soc.* **2015,** *137* (22), 6979–6982.

9. Wang, H.; Hsu, J.-H.; Yi, S.-I.; Kim, S. L.; Choi, K.; Yang, G.; Yu, C., Thermally Driven Large N-Type Voltage Responses from Hybrids of Carbon Nanotubes and Poly(3,4-ethylenedioxythiophene) with Tetrakis(dimethylamino)ethylene. *Adv. Mater.* **2015,** *27* (43), 6855–6861.

10. Nagarjuna, G.; Kokil, A.; Kumar, J.; Venkataraman, D., A straightforward route to electron transporting conjugated polymers. *J. Mater. Chem.* **2012,** *22* (31), 16091–16094

11. Nagarjuna, G. Breaking the Barriers of All-Polymer Solar Cells: Solving Electron Transporter And Morphology Problems. University of Massachusetts Amherst, 2012.

12. Debnath, S.; Boyle, C. J.; Zhou, D.; Wong, Bryan M.; Kittilstved, K. R.; Venkataraman, D., Persistent radical anion polymers based on naphthalenediimide and a vinylene spacer. *RSC Adv.* **2018,** *8* (27), 14760–14764.

13. Schlitz, R. A.; Brunetti, F. G.; Glaudell, A. M.; Miller, P. L.; Brady, M. A.; Takacs, C. J.; Hawker, C. J.; Chabinyc, M. L., Solubility-Limited Extrinsic n-Type Doping of a High Electron Mobility Polymer for Thermoelectric Applications. *Adv. Mater.* **2014,** *26* (18), 2825–2830.

14. Naab, B. D.; Zhang, S.; Vandewal, K.; Salleo, A.; Barlow, S.; Marder, S. R.; Bao, Z., Effective Solution- and Vacuum-Processed n-Doping by Dimers of Benzimidazoline Radicals. *Adv. Mater.* **2014,** *26* (25), 4268–4272.

15. Hwang, S.; Potscavage, Jr., W. J.; Yang, Y. S.; Park, I. S.; Matsushima, T.; Adachi, C., Solution-processed organic thermoelectric materials exhibiting doping-concentration-dependent polarity. *Phys. Chem. Chem. Phys.* **2016,** *18* (42), 29199–29207.

16. Wang, S.; Sun, H.; Ail, U.; Vagin, M.; Persson, P. O. Å.; Andreasen, J. W.; Thiel, W.; Berggren, M.; Crispin, X.; Fazzi, D.; Fabiano, S., Thermoelectric Properties of Solution-Processed n-Doped Ladder-Type Conducting Polymers. *Adv. Mater.* **2016,** *28* (48), 10764–10771.

17. Zhao, X.; Madan, D.; Cheng, Y.; Zhou, J.; Li, H.; Thon, S. M.; Bragg, A. E.; DeCoster, M. E.; Hopkins, P. E.; Katz, H. E., High Conductivity and Electron-Transfer Validation in an n-Type Fluoride-Anion-Doped Polymer for Thermoelectrics in Air. *Adv. Mater.* **2017,** *29* (34), 1606928.

18. Kumar, S.; Ajayakumar, M. R.; Hundal, G.; Mukhopadhyay, P., Extraordinary Stability of Naphthalenediimide Radical Ion and Its Ultra-Electron-Deficient Precursor: Strategic Role of the Phosphonium Group. *J. Am. Chem. Soc.* **2014,** *136* (34), 12004–12010.

19. Song, Q.; Li, F.; Wang, Z.; Zhang, X., A supramolecular strategy for tuning the energy level of naphthalenediimide: Promoted formation of radical anions with extraordinary stability. *Chem. Sci.* **2015,** *6* (6), 3342–3346.

20. Keshri, S. K.; Kumar, S.; Mandal, K.; Mukhopadhyay, P., Ambient Water-Stable Dianionic Electron Donors: Intramolecular Noncovalent Conduits Assist Charge Delocalization. *Chem. Eur. J.* **2017,** *23* (49), 11802–11809.

21. Katz, H. E.; Lovinger, A. J.; Johnson, J.; Kloc, C.; Siegrist, T.; Li, W.; Lin, Y.-Y.; Dodabalapur, A., A soluble and air-stable organic semiconductor with high electron mobility. *Nature* **2000,** *404* (6777), 478–481.

22. Chai, J.-D.; Head-Gordon, M., Long-range corrected hybrid density functionals with damped atom-atom dispersion corrections. *Phys. Chem. Chem. Phys.* **2008,** *10* (44), 6615–6620.

23. Golder, M. R.; Wong, B. M.; Jasti, R., Photophysical and theoretical investigations of the [8] cycloparaphenylene radical cation and its charge-resonance dimer. *Chem. Sci.* **2013,** *4* (11), 4285–4291.

24. Li, P.; Wong, B. M.; Zakharov, L. N.; Jasti, R., Investigating the Reactivity of 1,4-Anthracene-Incorporated Cycloparaphenylene. *Org. Lett.* **2016,** *18* (7), 1574–1577.

25. Liang, X.; Tan, L.; Liu, Z.; Ma, Y.; Zhang, G.; Wang, L.; Li, S.; Dong, L.; Li, J.; Chen, W., Poly(naphthalene diimide) vinylene: solid state red emission and semiconducting properties for transistors. *Chem. Commun.* **2017,** *53* (36), 4934–4937.

26. Kumar, Y.; Kumar, S.; Kumar Keshri, S.; Shukla, J.; Singh, S. S.; Thakur, T. S.; Denti, M.; Facchetti, A.; Mukhopadhyay, P., Synthesis of Octabromoperylene Dianhydride and Diimides: Evidence of Halogen Bonding and Semiconducting Properties. *Org. Lett.* **2016,** *18* (3), 472–475.

27. Ajayakumar, M. R.; Asthana, D.; Mukhopadhyay, P., Core-Modified Naphthalenediimides Generate Persistent Radical Anion and Cation: New Panchromatic NIR Probes. *Org. Lett.* **2012,** *14* (18), 4822–4825.

28. Ajayakumar, M. R.; Mukhopadhyay, P.; Yadav, S.; Ghosh, S., Single-Electron Transfer Driven Cyanide Sensing: A New Multimodal Approach. *Org. Lett.* **2010,** *12* (11), 2646–2649.

29. Fujitsuka, M.; Kim, S. S.; Lu, C.; Tojo, S.; Majima, T., Intermolecular and Intramolecular Electron Transfer Processes from Excited Naphthalene Diimide Radical Anions. *J. Phys. Chem. B* **2015,** *119* (24), 7275–7282.

30. Alvey, P. M.; Iverson, B. L., Reactions of Brominated Naphthalene Diimide with Bis(tributylstannyl)acetylene: A Simple Approach for Conjugated Polymers and Versatile Coupling Intermediates. *Org. Lett.* **2012,** *14* (11), 2706–2709.

31. Ye, L.; Jiao, X.; Zhang, H.; Li, S.; Yao, H.; Ade, H.; Hou, J., 2D-Conjugated Benzodithiophene-Based Polymer Acceptor: Design, Synthesis, Nanomorphology, and Photovoltaic Performance. *Macromolecules* **2015,** *48* (19), 7156–7163.

32. Zhan, X.; Facchetti, A.; Barlow, S.; Marks, T. J.; Ratner, M. A.; Wasielewski, M. R.; Marder, S. R., Rylene and Related Diimides for Organic Electronics. *Adv. Mater.* **2011,** *23* (2), 268–284.

33. Seifert, S.; Schmidt, D.; Würthner, F., An ambient stable core-substituted perylene bisimide dianion: isolation and single crystal structure analysis. *Chem. Sci.* **2015,** *6* (3), 1663–1667.

34. Shirman, E.; Ustinov, A.; Ben-Shitrit, N.; Weissman, H.; Iron, M. A.; Cohen, R.; Rybtchinski, B., Stable Aromatic Dianion in Water. *J. Phys. Chem. B.* **2008,** *112* (30), 8855–8858.

35. Naab, B. D.; Gu, X.; Kurosawa, T.; To, J. W. F.; Salleo, A.; Bao, Z., Role of Polymer Structure on the Conductivity of N-Doped Polymers. *Adv. Electron. Mater.* **2016,** *2* (5), 1600004.

36. Guo, Y.; Li, Y.; Awartani, O.; Zhao, J.; Han, H.; Ade, H.; Zhao, D.; Yan, H., A Vinylene-Bridged Perylenediimide-Based Polymeric Acceptor Enabling Efficient All-Polymer Solar Cells Processed under Ambient Conditions. *Adv. Mater.* **2016,** *28* (38), 8483–8489.

37. Meier, H.; Stalmach, U.; Kolshorn, H., Effective conjugation length and UV/vis spectra of oligomers. *Acta Polym.* **1997,** *48* (9), 379–384.

38. Rissler, J., Effective conjugation length of π-conjugated systems. *Chem. Phys. Lett.* **2004,** *395* (1-3), 92–96.

39. Wang, S.; Sun, H.; Erdmann, T.; Wang, G.; Fazzi, D.; Lappan, U.; Puttisong, Y.; Chen, Z.; Berggren, M.; Crispin, X.; Kiriy, A.; Voit, B.; Marks, T. J.; Fabiano, S.; Facchetti, A., A Chemically Doped Naphthalenediimide-Bithiazole Polymer for n-Type Organic Thermoelectrics. *Adv. Mater.* **2018**, 1801898.

40. Giovannitti, A.; Nielsen, C. B.; Sbircea, D.-T.; Inal, S.; Donahue, M.; Niazi, M. R.; Hanifi, D. A.; Amassian, A.; Malliaras, G. G.; Rivnay, J.; McCulloch, I., N-type organic electrochemical transistors with stability in water. *Nat. Commun.* **2016,** *7*, 13066.

41. Sun, H.; Vagin, M.; Wang, S.; Crispin, X.; Forchheimer, R.; Berggren, M.; Fabiano, S., Complementary Logic Circuits Based on High-Performance n-Type Organic Electrochemical Transistors. *Adv. Mater.* **2018,** *30* (9), 1704916.

42. Smits, J. H. A.; Meskers, S. C. J.; Janssen, R. A. J.; Marsman, A. W.; de Leeuw, D. M., Electrically Rewritable Memory Cells from Poly(3-hexylthiophene) Schottky Diodes. *Adv. Mater.* **2005,** *17* (9), 1169–1173.

43. Lai, Q.; Zhu, Z.; Chen, Y.; Patil, S.; Wudl, F., Organic nonvolatile memory by dopant-configurable polymer. *Appl. Phys. Lett.* **2006,** *88* (13), 133515.

44. Bounioux, C.; Díaz-Chao, P.; Campoy-Quiles, M.; Martín-González, M. S.; Goñi, A. R.; Yerushalmi-Rozen, R.; Müller, C., Thermoelectric composites of poly(3-hexylthiophene) and carbon nanotubes with a large power factor. *Energy Environ. Sci.* **2013,** *6* (3), 918–925.

45. Kim, D.; Kim, Y.; Choi, K.; Grunlan, J. C.; Yu, C., Improved Thermoelectric Behavior of Nanotube-Filled Polymer Composites with Poly(3,4-ethylenedioxythiophene) Poly(styrenesulfonate). *ACS Nano* **2010,** *4* (1), 513–523.

46. Wu, G.; Zhang, Z. G.; Li, Y.; Gao, C.; Wang, X.; Chen, G., Exploring High-Performance n-Type Thermoelectric Composites Using Amino-Substituted Rylene Dimides and Carbon Nanotubes. *ACS Nano* **2017,** *11* (6), 5746–5752.

47. Tonga, M.; Wei, L.; Wilusz, E.; Korugic-Karasz, L.; Karasz, F. E.; Lahti, P. M., Solution-fabrication dependent thermoelectric behavior of iodine-doped regioregular and regiorandom P3HT/carbon nanotube composites. *Synth. Met.* **2018,** *239*, 51–58.

48. Tonga, M.; Wei, L.; Taylor, P. S.; Wilusz, E.; Korugic-Karasz, L.; Karasz, F. E.; Lahti, P. M., Thermoelectric Enhancement by Compositing Carbon Nanotubes into Iodine-Doped Poly[2-methoxy-5-(2-ethylhexyloxy)-1,4-phenylenevinylene]. *ACS Appl. Mater. Interfaces* **2017,** *9* (10), 8975–8984.

49. Mai, C.-K.; Russ, B.; Fronk, S. L.; Hu, N.; Chan-Park, M. B.; Urban, J. J.; Segalman, R. A.; Chabinyc, M. L.; Bazan, G. C., Varying the ionic functionalities of conjugated polyelectrolytes leads to both p- and n-type carbon nanotube composites for flexible thermoelectrics. *Energy Environ. Sci.* **2015,** *8* (8), 2341–2346.

50. Hong, C. T.; Yoo, Y.; Kang, Y. H.; Ryu, J.; Cho, S. Y.; Jang, K.-S., Effect of film thickness and crystallinity on the thermoelectric properties of doped P3HT films. *RSC Adv.* **2015,** *5* (15), 11385–11391.

51. Lee, W.; Hong, C. T.; Kwon, O. H.; Yoo, Y.; Kang, Y. H.; Lee, J. Y.; Cho, S. Y.; Jang, K.-S., Enhanced Thermoelectric Performance of Bar-Coated SWCNT/P3HT Thin Films. *ACS Appl. Mater. Interfaces* **2015,** *7* (12), 6550–6556.

52. Tonga, M. Conjugated Polymers in Thermoelectric Composites and Small Molecules for High Light Absorptivity. University of Massachusetts Amherst, University of Massachusetts Amherst, 2015.

53. Hong, C. T.; Kang, Y. H.; Ryu, J.; Cho, S. Y.; Jang, K.-S., Spray-printed CNT/P3HT organic thermoelectric films and power generators. *J. Mater. Chem. C* **2015,** *3* (43), 21428–21433.

54. Bradley, K.; Jhi, S. H.; Collins, P. G.; Hone, J.; Cohen, M. L.; Louie, S. G.; Zettl, A., Is the intrinsic thermoelectric power of carbon nanotubes positive? *Phys. Rev. Lett.* **2000,** *85* (20), 4361–4364.

55. Collins, P. G.; Bradley, K.; Ishigami, M.; Zettl, A., Extreme Oxygen Sensitivity of Electronic Properties of Carbon Nanotubes. *Science* **2000,** *287* (5459), 1801–1804.

56. Nonoguchi, Y.; Nakano, M.; Murayama, T.; Hagino, H.; Hama, S.; Miyazaki, K.; Matsubara, R.; Nakamura, M.; Kawai, T., Simple Salt-Coordinated n-Type Nanocarbon Materials Stable in Air. *Adv. Funct. Mater.* **2016,** *26* (18), 3021–3028.

57. Nonoguchi, Y.; Ohashi, K.; Kanazawa, R.; Ashiba, K.; Hata, K.; Nakagawa, T.; Adachi, C.; Tanase, T.; Kawai, T., Systematic Conversion of Single Walled Carbon Nanotubes into n-type Thermoelectric Materials by Molecular Dopants. *Sci. Rep.* **2013,** *3*, 3344.

58. Freeman, D. D.; Choi, K.; Yu, C., N-type Thermoelectric Performance of Functionalized Carbon Nanotube-Filled Polymer Composites. *PLoS One* **2012,** *7* (11), e47822.

59. Kymakis, E.; Amaratunga, G. A. J., Electrical properties of single-wall carbon nanotube-polymer composite films. *J. Appl. Phys.* **2006,** *99* (8), 084302.

60. Connor, M. T.; Roy, S.; Ezquerra, T. A.; Baltá Calleja, F. J., Broadband ac conductivity of conductor-polymer composites. *Phys. Rev. B* **1998,** *57* (4), 2286–2294.

61. MacLeod, B. A.; Stanton, N. J.; Gould, I. E.; Wesenberg, D.; Ihly, R.; Owczarczyk, Z. R.; Hurst, K. E.; Fewox, C. S.; Folmar, C. N.; Holman Hughes, K.; Zink, B. L.; Blackburn, J. L.; Ferguson, A. J., Large n- and p-type thermoelectric power factors from doped semiconducting single-walled carbon nanotube thin films. *Energy Environ. Sci.* **2017,** *10* (10), 2168–2179.

62. Boyle, C. J.; Upadhyaya, M.; Wang, P.; Renna, L. A.; Korugic-Karasz, L.; Barnes, M. D.; Aksamija, Z.; Venkataraman, D., Spatial Heterogeneity of Dopants Impacts the Thermoelectric Charge Transport Properties. *In Preparation* **2018.**

63. Friend, R. H.; Gymer, R. W.; Holmes, A. B.; Burroughes, J. H.; Marks, R. N.; Taliani, C.; Bradley, D. D. C.; Dos Santos, D. A.; Brédas, J. L.; Lögdlund, M.; Salaneck, W. R., Electroluminescence in conjugated polymers. *Nature* **1999,** *397* (6715), 121–128.

64. Thejo Kalyani, N.; Dhoble, S. J., Organic light emitting diodes: Energy saving lighting technology—A review. *Renew. Sustainable Energy Rev.* **2012,** *16* (5), 2696–2723.

65. Xu, R.-P.; Li, Y.-Q.; Tang, J.-X., Recent advances in flexible organic light-emitting diodes. *J. Mater. Chem. C* **2016,** *4* (39), 9116–9142.

66. Günes, S.; Neugebauer, H.; Sariciftci, N. S., Conjugated Polymer-Based Organic Solar Cells. *Chem. Rev.* **2007,** *107* (4), 1324–1338.

67. Su, Y.-W.; Lan, S.-C.; Wei, K.-H., Organic photovoltaics. *Mater. Today* **2012,** *15* (12), 554–562.

68. Cheng, P.; Li, G.; Zhan, X.; Yang, Y., Next-generation organic photovoltaics based on non-fullerene acceptors. *Nat. Photonics* **2018,** *12* (3), 131–142.

69. Bubnova, O.; Crispin, X., Towards polymer-based organic thermoelectric generators. *Energy Environ. Sci.* **2012,** *5* (11), 9345–9362.

70. Zhang, Q.; Sun, Y.; Xu, W.; Zhu, D., Organic Thermoelectric Materials: Emerging Green Energy Materials Converting Heat to Electricity Directly and Efficiently. *Adv. Mater.* **2014,** *26* (40), 6829–6851.

71. Russ, B.; Glaudell, A.; Urban, J. J.; Chabinyc, M. L.; Segalman, R. A., Organic thermoelectric materials for energy harvesting and temperature control. *Nat. Rev. Mater.* **2016,** *1* (10), 16050.

72. Arkhipov, V. I.; Heremans, P.; Emelianova, E. V.; Adriaenssens, G. J.; Bässler, H., Charge carrier mobility in doped semiconducting polymers. *Appl. Phys. Lett.* **2003,** *82* (19), 3245–3247.

73. Li, L.; Meller, G.; Kosina, H., Carrier concentration dependence of the mobility in organic semiconductors. *Synth. Met.* **2007,** *157* (4-5), 243–246.

74. Bouhassoune, M.; van Mensfoort, S. L. M.; Bobbert, P. A.; Coehoorn, R., Carrier-density and field-dependent charge-carrier mobility in organic semiconductors with correlated Gaussian disorder. *Org. Electron.* **2009,** *10* (3), 437–445.

75. Fishchuk, I. I.; Kadashchuk, A. K.; Genoe, J.; Ullah, M.; Sitter, H.; Singh, T. B.; Sariciftci, N. S.; Bässler, H., Temperature dependence of the charge carrier mobility in disordered organic semiconductors at large carrier concentrations. *Phys. Rev. B* **2010,** *81* (4), 045202.

76. Fishchuk, I. I.; Kadashchuk, A.; Ullah, M.; Sitter, H.; Pivrikas, A.; Genoe, J.; Bässler, H., Electric field dependence of charge carrier hopping transport within the random energy landscape in an organic field effect transistor. *Phys. Rev. B* **2012,** *86* (4), 045207.

77. Heck, A.; Kranz, J. J.; Elstner, M., Simulation of Temperature-Dependent Charge Transport in Organic Semiconductors with Various Degrees of Disorder. *J. Chem. Theory Comput.* **2016,** *12* (7), 3087–3096.

78. Kaiser, W.; Albes, T.; Gagliardi, A., Charge carrier mobility of disordered organic semiconductors with correlated energetic and spatial disorder. *Phys. Chem. Chem. Phys.* **2018,** *20* (13), 8897–8908.

79. Tiwari, S.; Greenham, N. C., Charge mobility measurement techniques in organic semiconductors. *Opt. Quantum Electron.* **2009,** *41* (2), 69–89.

80. Kokil, A.; Yang, K.; Kumar, J., Techniques for characterization of charge carrier mobility in organic semiconductors. *J. Polym. Sci. B* **2012,** *50* (15), 1130–1144.

81. Blakesley, J. C.; Castro, F. A.; Kylberg, W.; Dibb, G. F. A.; Arantes, C.; Valaski, R.; Cremona, M.; Kim, J. S.; Kim, J.-S., Towards reliable charge-mobility benchmark measurements for organic semiconductors. *Org. Electron.* **2014,** *15* (6), 1263–1272.

82. Jonson, M.; Mahan, G. D., Mott's formula for the thermopower and the Wiedemann-Franz law. *Phys. Rev. B* **1980,** *21* (10), 4223–4229.

83. Niu, J.; Lu, N.; Li, L.; Liu, M., Polaron effect dependence of thermopower in organic semiconductors. *Phys. Lett. A* **2014,** *378* (48), 3579–3581.

84. Lu, N.; Li, L.; Liu, M., A review of carrier thermoelectric-transport theory in organic semiconductors. *Phys. Chem. Chem. Phys.* **2016,** *18* (29), 19503–19525.

85. Shi, X.; Sun, J., Dependence of Seebeck Coefficient on the Density of States in Organic Semiconductors. *IEEE Electron Device Lett.* **2017,** *38* (12), 1728–1731.

86. Miller, A.; Abrahams, E., Impurity Conduction at Low Concentrations. *Phys. Rev.* **1960,** *120* (3), 745–755.

87. Marcus, R. A., Chemical and Electrochemical Electron-Transfer Theory. *Annu. Rev. Phys. Chem.* **1964,** *15*, 155–196.

88. Kang, S. D.; Snyder, G. J., Charge-transport model for conducting polymers. *Nat. Mater.* **2017,** *16* (2), 252–257.

89. Xuan, Y.; Liu, X.; Desbief, S.; Leclère, P.; Fahlman, M.; Lazzaroni, R.; Berggren, M.; Cornil, J.; Emin, D.; Crispin, X., Thermoelectric properties of conducting polymers: The case of poly(3-hexylthiophene). *Phys. Rev. B* **2010,** *82* (11), 115454.

90. Culebras, M.; Gòmez, C. M.; Cantarero, A., Enhanced thermoelectric performance of PEDOT with different counter-ions optimized by chemical reduction. *J. Mater. Chem. A* **2014,** *2* (26), 10109–10115.

91. Zhang, Q.; Sun, Y.; Xu, W.; Zhu, D., What To Expect from Conducting Polymers on the Playground of Thermoelectricity: Lessons Learned from Four High-Mobility Polymeric Semiconductors. *Macromolecules* **2014,** *47* (2), 609–615.

92. Glaudell, A. M.; Cochran, J. E.; Patel, S. N.; Chabinyc, M. L., Impact of the Doping Method on Conductivity and Thermopower in Semiconducting Polythiophenes. *Adv. Energy Mater.* **2015,** *5* (4), 1401072.

93. Patel, S. N.; Glaudell, A. M.; Kiefer, D.; Chabinyc, M. L., Increasing the Thermoelectric Power Factor of a Semiconducting Polymer by Doping from the Vapor Phase. *ACS Macro Lett.* **2016,** *5* (3), 268–272.

94. Jung, I. H.; Hong, C. T.; Lee, U.-H.; Kang, Y. H.; Jang, K.-S.; Cho, S. Y., High Thermoelectric Power Factor of a Diketopyrrolopyrrole-Based Low Bandgap Polymer via Finely Tuned Doping Engineering. *Sci. Rep.* **2017,** *7*, 44704.

95. Qiu, L.; Liu, J.; Alessandri, R.; Qiu, X.; Koopmans, M.; Havenith, R. W. A.; Marrink, S. J.; Chiechi, R. C.; Koster, L. J. A.; Hummelen, J. C., Enhancing doping efficiency by improving host-dopant miscibility for fullerene-based n-type thermoelectrics. *J. Mater. Chem. A* **2017,** *5* (40), 21234–21241.

96. Pernstich, K. P.; Rössner, B.; Batlogg, B., Field-effect-modulated Seebeck coefficient in organic semiconductors. *Nat. Mater.* **2008,** *7* (4), 321–325.

97. Zhang, F.; Zang, Y.; Huang, D.; Di, C.-a.; Gao, X.; Sirringhaus, H.; Zhu, D., Modulated thermoelectric properties of organic semiconductors using field-effect transistors. *Adv. Funct. Mater.* **2015,** *25* (20), 3004–3012.

98. Li, L.; Lu, N.; Liu, M., Effect of dipole layer on the density-of-states and charge transport in organic thin film transistors. *Appl. Phys. Lett.* **2013,** *103* (25), 253303.

99. Bubnova, O.; Berggren, M.; Crispin, X., Tuning the Thermoelectric Properties of Conducting Polymers in an Electrochemical Transistor. *J. Am. Chem. Soc.* **2012,** *134* (40), 16456–16459.

100. Thomas, E. M.; Popere, B. C.; Fang, H.; Chabinyc, M. L.; Segalman, R. A., Role of Disorder Induced by Doping on the Thermoelectric Properties of Semiconducting Polymers. *Chem. Mater.* **2018,** *30* (9), 2965–2972.

101. Zuzok, R.; Kaiser, A. B.; Pukacki, W.; Roth, S., Thermoelectric power and conductivity of iodine-doped ‘‘new’’ polyacetylene. *J. Chem. Phys.* **1991,** *95* (2), 1270–1275.

102. Park, Y. W., Structure and morphology: relation to thermopower properties of conductive polymers. *Synth. Met.* **1991,** *45* (2), 173–182.

103. Hiroshige, Y.; Ookawa, M.; Toshima, N., Thermoelectric figure-of-merit of iodine-doped copolymer of phenylenevinylene with dialkoxyphenylenevinylene. *Synth. Met.* **2007,** *157* (10-12), 467–474.

104. Hayashi, K.; Shinano, T.; Miyazaki, Y.; Kajitani, T., Fabrication of iodine-doped pentacene thin films for organic thermoelectric devices. *J. Appl. Phys.* **2011,** *109* (2), 023712.

105. Kim, G. H.; Shtein, M.; Pipe, K. P., Thermoelectric and bulk mobility measurements in pentacene thin films. *Appl. Phys. Lett.* **2011,** *98* (9), 093303.

106. Taylor, P. S.; Korugic-Karasz, L.; Wilusz, E.; Lahti, P. M.; Karasz, F. E., Thermoelectric studies of oligophenylenevinylene segmented block copolymers and their blends with MEH-PPV. *Synth. Met.* **2013,** *185–186*, 109–114.

107. Bredas, J. L.; Street, G. B., Polarons, bipolarons, and solitons in conducting polymers. *Acc. Chem. Res.* **2002,** *18* (10), 309–315.

108. Borsenberger, P. M.; Pautmeier, L.; Bässler, H., Charge transport in disordered molecular solids. *J. Chem. Phys.* **1991,** *94* (8), 5447–5454.

109. Bässler, H., Charge Transport in Disordered Organic Photoconductors a Monte Carlo Simulation Study. *Phys. Status Solidi B* **1993,** *175* (1), 15–56.

110. Pasveer, W. F.; Cottaar, J.; Tanase, C.; Coehoorn, R.; Bobbert, P. A.; Blom, P. W. M.; de Leeuw, D. M.; Michels, M. A. J., Unified Description of Charge-Carrier Mobilities in Disordered Semiconducting Polymers. *Phys. Rev. Lett.* **2005,** *94* (20), 206601.

111. Mendels, D.; Tessler, N., Thermoelectricity in Disordered Organic Semiconductors under the Premise of the Gaussian Disorder Model and Its Variants. *J. Phys. Chem. Lett.* **2014,** *5* (18), 3247–3253.

112. Arkhipov, V. I.; Heremans, P.; Emelianova, E. V.; Bässler, H., Effect of doping on the density-of-states distribution and carrier hopping in disordered organic semiconductors. *Phys. Rev. B* **2005,** *71* (4), 045214.

113. Ihnatsenka, S.; Crispin, X.; Zozoulenko, I. V., Understanding hopping transport and thermoelectric properties of conducting polymers. *Phys. Rev. B* **2015,** *92* (3), 035201.

114. Melitz, W.; Shen, J.; Kummel, A. C.; Lee, S., Kelvin probe force microscopy and its application. *Surf. Sci. Rep.* **2011,** *66* (1), 1–27.

115. Jenkins, J. L.; Lee, P. A.; Nebesny, K. W.; Ratcliff, E. L., Systematic electrochemical oxidative doping of P3HT to probe interfacial charge transfer across polymer–fullerene interfaces. *J. Mater. Chem. A* **2014,** *2* (45), 19221–19231.

116. Pecher, J.; Mecking, S., Nanoparticles of Conjugated Polymers. *Chem. Rev.* **2010,** *110* (10), 6260–6279.

117. Berggren, M.; Forchheimer, R.; Bobacka, J.; Svensson, P.-O.; Nilsson, D.; Larsson, O.; Ivaska, A., PEDOT:PSS-Based Electrochemical Transistors for Ion-to-Electron Transduction and Sensor Signal Amplification. In *Organic Semiconductors in Sensor Applications*, Spring, Berlin, Heidelberg: 2008; Vol. 107, pp 263–280.

118. Brown, T. M.; Kim, J. S.; Friend, R. H.; Cacialli, F.; Daik, R.; Feast, W. J., Built-in field electroabsorption spectroscopy of polymer light-emitting diodes incorporating a doped poly(3,4-ethylene dioxythiophene) hole injection layer. *Appl. Phys. Lett.* **1999,** *75* (12), 1679–1681.

119. Steim, R.; Kogler, F. R.; Brabec, C. J., Interface materials for organic solar cells. *J. Mater. Chem.* **2010,** *20* (13), 2499–2512.

120. Kumar, S. S.; Mathiyarasu, J.; Phani, K. L. N.; Yegnaraman, V., Simultaneous determination of dopamine and ascorbic acid on poly (3,4-ethylenedioxythiophene) modified glassy carbon electrode. *J. Solid State Electrochem.* **2005,** *10* (11), 905–913.

121. Mueller, M.; Fabretto, M.; Evans, D.; Hojati-Talemi, P.; Gruber, C.; Murphy, P., Vacuum vapour phase polymerization of high conductivity PEDOT: Role of PEG-PPG-PEG, the origin of water, and choice of oxidant. *Polymer* **2012,** *53* (11), 2146–2151.

122. Ha, Y.-H.; Nikolov, N.; Pollack, S. K.; Mastrangelo, J.; Martin, B. D.; Shashidhar, R., Towards a Transparent, Highly Conductive Poly(3,4-ethylenedioxythiophene). *Adv. Funct. Mater.* **2004,** *14* (6), 615–622.

123. Mitraka, E.; Jafari, M. J.; Vagin, M.; Liu, X.; Fahlman, M.; Ederth, T.; Berggren, M.; Jonsson, M. P.; Crispin, X., Oxygen-induced doping on reduced PEDOT. *J. Mater. Chem. A* **2017,** *5* (9), 4404–4412.

124. van der Holst, J. J. M. Three-dimensional modeling of charge transport, injection and recombination in organic light-emitting diodes. Technische Universiteit Eindhoven, Eindhoven, 2010.

125. Upadhyaya, M.; Boyle, C. J.; Venkataraman, D.; Aksamija, Z., Effects of disorder on thermoelectric properties of semiconducting polymers. *Submitted* **2018.**